CARBON DIFFUSION ACROSS DISSIMILAR STEEL WELDS

By
Julia Margaret Race
St. John's College, Cambridge

Department of Materials Science and Metallurgy
Pembroke Street
Cambridge
CB2 3QZ

A dissertation submitted for the degree of Doctor of Philosophy

October 1992

For Grandpa

If you can dream – and not make dreams your master
If you can think – and not make thoughts your aim:

Rudyard Kipling

PREFACE

This dissertation is submitted for the Degree of Doctor of Philosophy in Natural Sciences at the University of Cambridge. The investigation described in this thesis was carried out under the supervision of Dr. H. K. D. H. Bhadeshia at the Department of Materials Science and Metallurgy, Cambridge, between October 1989 and October 1992. Except where acknowledgement and reference to previous work is made, this work is original and carried out without collaboration. Neither this, nor any substantially similar dissertation has been or is being submitted for any degree, diploma or other qualification at any other university.

This dissertation contains less than 60,000 words.

Julia Race

October 1992

ACKNOWLEDGEMENTS

Financial and technical support for this research was provided by NEI Parsons Ltd; in particular the involvement of Brian Greenwell and Roger Conroy is appreciated. Thanks are also due to Prof. Colin Humphreys for the provision of laboratory facilities at the University of Cambridge and to the technical staff of the Materials Science and Metallurgy department for their assistance. Invaluable help was received from David Nichol and Brian Barber.

The project was supervised enthusiastically by Dr. Harry Bhadeshia, to whom I am extremely grateful for his encouragement and advice. My thanks and best wishes go to the rest of the PT group with whom it has been a pleasure to work.

Finally, I would like to thank my parents and family for their constant love and support.

ABSTRACT

Dissimilar steel welds are used extensively in the power generation industry in boiler tubing to accommodate changing temperature, pressure and corrosive conditions in different locations. Joints like these are prone to failure and can cause steam leakage resulting in expensive shut downs. A principle cause of failure is the migration of carbon, in general, from the low alloy side to the high alloy side of the weld. This leaves an area on one side of the weld denuded of carbon and therefore weaker in terms of stress rupture. The other side is correspondingly enriched and there may be further detrimental effects on the mechanical properties as a consequence. The partitioning of carbon occurs even when both sides of the weld have identical carbon concentrations because the driving force for its migration is the difference in carbon chemical potential as caused by the variation in the substitutional solute content across the junction.

Mathematical models have been produced in this work to model the diffusion of carbon across dissimilar metal welds in both the austenite, and ferrite plus carbide phase fields. Carbon diffusion profiles across joints in the austenite phase field can be accurately predicted by the combination of the equations to describe diffusion. The only limitation to this is the accurate prediction of the partition coefficient in concentrated solutions. However, this method could not be extended to the ferrite phase field. Experimental results from dissimilar metal joints heat treated in the ferrite phase field indicated that the dissolution and precipitation of carbides is instrumental in providing a 'source' and 'sink' for the diffusion carbon, a fact which could not be accounted for in any previous model. The present model is based on a series of discrete carbide particles on either side of the weld interface which dissolve and grow, thereby simulating the dissolution and precipitation of carbides. The real situation is further complicated by the fact that the experimental measurements of the decarburised zone widths do not exhibit parabolic kinetics as is normally assumed but tend to level off on a plot against root time. Furthermore, the influx of carbon into the high alloy side of the weld changes the precipitation sequences that occur on that side of the weld. It has been shown that these changes in precipitation sequences are significant in causing a reduction in the rate of decarburisation. This has been successfully incorporated into the model allowing the prediction of decarburised zone widths and relative comparisons of the extent of decarburisation to be made between different alloy systems.

Nomenclature List.

a_c	Activity of carbon
$a_c^{\alpha\theta}$	Activity of carbon at α/θ interface
$a_c^{\theta\alpha}$	Activity of carbon at θ/α interface
A_1	A constant
A_2	A constant
A_3	A constant
A_4	A constant
B	A constant
B_1	A constant
B_2	A constant
C_1	A constant
C_{B_i}	Concentration of B atoms on plane i
d_{20}	Original particle size on the high carbon activity side of the interface
$\overline{D}$	Average integrated diffusivity
D_B	Diffusion coefficient of B atoms
D_{ik}	Diffusion coefficient of element i under the influence of a gradient in element k
D^{O-T-O}	Diffusion coefficient for carbon atoms jumping from an octahedral to an octahedral site via a tetrahedral site
D^{T-O-T}	Diffusion coefficient for carbon atoms jumping from a tetrahedral to a tetrahedral site via an octahedral site
D^{T-T}	Diffusion coefficient for carbon atoms jumping from a tetrahedral to a tetrahedral site
D_α	Diffusion coefficient of carbon in α
D_β	Diffusion coefficient of carbon in β
D_θ	Diffusion coefficient of carbon in θ
D1	Slab size on the high carbon activity side of the interface
D2	Particle size on the high carbon activity side
D3	Interparticle spacing on the high carbon activity side
D4	Particle size on the low carbon activity side of the interface
D5	Slab size on the low carbon activity side
D6	Interparticle spacing on the low carbon activity side
E_u^T	Change in Gibbs free energy of pure solvent when a solute atom is inserted in a tetrahedral site
E_u^O	Change in Gibbs free energy of pure solvent when a solute atom is inserted in an octahedral site
f	Fraction of remaining atoms which jump via the T–T route
G_1	Free energy of the B–rich alloy
G_2	Free energy of the A–rich alloy
G_3	Initial free energy of the alloy block
G_4	Free energy of the homogeneous A–B alloy
h	Planck's constant
J_B	Flux of B atoms
J_i	Flux of element i
$\overrightarrow{J}$	Flux of B atoms from left to right
$\overleftarrow{J}$	Flux of B atoms from right to left
k	Partition coefficient
k_B	Boltzmann's constant
n_i	Number of B atoms on plane i /m^2

R	Universal gas constant
S_u^T	Change in vibrational entropy of pure solvent when a solute atom is inserted in a tetrahedral site
S_u^O	Change in vibrational entropy of pure solvent when a solute atom is inserted in an octahedral site
T	Temperature
t	Time in seconds
V_i^A	Rate of change of z_i^A
v_α	Volume fraction of carbide A
v_β	Volume fraction of carbide B
x_k	Concentration of element k
$x^{A\alpha}$	Carbon concentration in the carbide A on the high carbon activity side in equilibrium with the ferrite
$x^{B\beta}$	Carbon concentration in the carbide B on the low carbon activity side
$x^{B_2\beta}$	Carbon concentration in the carbide B2 on the low carbon activity side in the second slice in equilibrium with the ferrite
x^α	Carbon concentration in α
x^θ	Carbon concentration in θ
$\overline{x}$	Average carbon concentration of the alloy
$\overline{x_\alpha}$	Average carbon concentration on the α side of the interface
$\overline{x_\beta}$	Average carbon concentration on the β side of the interface
$x^{\alpha A}$	Carbon concentration in the ferrite on the high carbon activity side in equilibrium with the carbide A
$x^{\alpha o}$	Initial carbon concentration in α
$x^{\beta o}$	Initial carbon concentration in β
$x^{\beta B}$	Carbon concentration in the ferrite on the low carbon activity side
$x^{\beta B_1}$	Carbon concentration in the ferrite on the low carbon activity side in the first slice in equilibrium with carbide B1
$x^{\beta B_2}$	Carbon concentration in the ferrite on the low carbon activity side in the second slice in equilibrium with the carbide B2
$x^{\theta o}$	Initial carbon concentration in θ
$x^{\alpha\beta}$	Carbon concentration in α when it is in equilibrium with β at the interface
$x^{\alpha\theta}$	Carbon concentration in α when it is in equilibrium with θ at the interface
$x^{\beta\alpha}$	Carbon concentration in β when it is in equilibrium with α at the interface
$x^{\theta\alpha}$	Carbon concentration in θ when it is in equilibrium with α at the interface
$x^{Fe_3C/\alpha}$	Carbon equilibrium between ferrite and cementite
$x_\gamma^{\gamma\alpha}$	Maximum permissible carbon content in the austenite at the transformation interface
X	Atom fraction of carbon atoms
z_a	Co-ordination number of an octahedral site in the austenite lattice
z	Coordinate normal to the diffusion boundary
z_o	Distance between particles on the low carbon activity side of the interface
z_i^A	Distance from weld interface to carbide particle after time t on the high carbon activity side
z_o^A	Initial distance from the weld interface to the carbide on the high carbon activity side
z_j^B	Distance from weld interface to carbide particle after time t on the low carbon activity side
z_o^B	Initial distance from the weld interface to the carbide on the low carbon activity side

x_1	Carbon concentration in solution on the high carbon activity side of the interface
α	High carbon activity side of the interface
β	Low carbon activity side of the interface for ferritic joints
γ_m	Activity coefficient of the activated complex
Δc	Amount of carbon transferred from slice 1 to slice 2 on the low carbon activity side of the weld
$\Delta^o G_c^{\gamma \rightarrow gr}$	Molar Gibbs free energy of pure carbon for the change in crystal structure $\gamma \rightarrow$ graphite
ΔF^*	Activation free energy
Δx_1	Difference in carbon concentration across the interface
Δx_2	Difference in alloy concentration across the interface
ϵ_{ij}	Wagner interaction coefficient between element i and j
λ	Distance between {002} austenite planes
υ	Separation of planes of atoms
μ	Chemical potential
μ_o	Chemical potential of the standard state
$\mu_{\alpha\theta}$	Chemical potential of carbon at α/θ interface
$\mu_{\theta\alpha}$	Chemical potential of carbon at θ/α interface
Γ_B	Jump rate of interstitial atoms
Γ_i	Activity coefficient of element i
Γ_α	Activity coefficient of carbon on the α side of the weld
Γ_θ	Activity coefficient of carbon on the θ side of the weld
θ	Low carbon activity side of the interface for austenitic joints
σ	Atom fraction of carbon atoms
η^α	Decarburised zone width
η^β	Carburised zone width
ξ	Dimensionless parameter
ω	Atom fraction of carbon atoms
ϕ	Fraction of the total interstitial atoms in the octahedral sites

CONTENTS

CHAPTER 1

Introduction

1.1 The Power Station

The operation of a turbine-generator plant is independent of the fuel source used to create the steam and works along the following basic principle. Water is converted to steam in the evaporator and is passed to the steam drum. The steam from the drum is collected in headers and passed through between one and three stages of superheat before being passed to the high pressure (HP) turbine. From the HP turbine, the steam returns to the reheater to be raised to the original steam temperature and pressure before entering the intermediate pressure (IP) turbine. The steam leaving the IP turbine is then passed through upto three LP turbines depending on the size of the plant. The steam exhausted from the last low pressure stage is condensed and circulated through a feed heater and economiser stage on its way back to the boiler. The basic layout of the steam generation plant is illustrated in Figure 1.1.

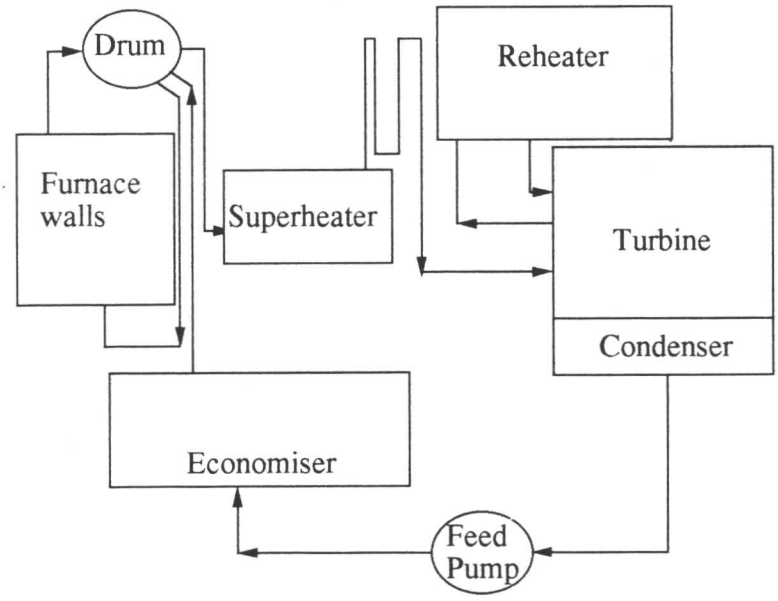

Figure 1.1: Schematic representation of the power plant layout.

1.2 Material considerations

1.2.1 Mechanical properties

The first requirement of any potential material is that it should exhibit adequate mechanical properties when exposed under design conditions for the specified life to the operating

environment. Any material must therefore have the mechanical properties adequate enough to sustain steady, instantaneous or cyclic stresses when operating at the design temperature and pressure. Fossil fuelled boilers and gas and liquid metal cooled reactors can generate steam at upto 600°C, but more recently temperatures have been standardised at 540°C to produce lower capital costs and greater reliability. In the majority of cases the final steam temperature of both superheat and reheat cycles is 535–570°C. Water tubes rarely exceed 350–400°C, but final stage superheater and reheater components may reach temperatures as high as 650°C.

Creep is therefore an important design consideration for steam tubes operating at temperatures in excess of 400°C. Steam pressures for conventional reheat plant have been standardised at 1.68×10^7 Pa because this is the highest pressure at which reasonable steam/water separation can be obtained. The large volume of working liquid (1.26×10^4kg/s for a 660 MW, 540°C unit) is conveyed between the boiler and the turbines by about 60m of pipework. These pipes must be large enough to pass this quantity of steam without excessive pressure loss and the wall thickness must be large enough to withstand the bursting forces generated by the pressure. The typical working conditions of a 550MW turbo–generator plant are given in Table 1.1, from which the variety of temperatures and pressures experienced by the plant can be gauged. Ductility is also a very important property which must be considered especially when new, as this affects the fabricability, but also when aged in service as loss of ductility can lead to crack inititation.

Evaporation	1.58×10 6kghr^{-1}
Drum conditions	18.3MPa, 680°C
Superheater outlet temperature	541°C
Superheater outlet pressure	16.6MPa
Reheater inlet temperature	348°C
Reheater inlet pressure	4.3MPa
Reheater outlet temperature	541°C
Reheater outlet pressure	4.1MPa
Initial feedwater inlet temperature	254°C

Table 1.1: Typical operating conditions for a 550MW power station.

1.2.2 Fabrication

The material must be able to be fabricated by the available equipment to the shape and

properties required. In the area of fabrication and especially in steam plant pipe lines, the weldability of a material is very important. Weldability is a widely used term, but is poorly defined and can probably be best described as:-

'the capacity of a metal or a combination of metals to be welded under the fabrication conditions imposed into a specific, suitably designed structure and to perform satisfactorily in the intended service. The better the weldability, the easier these requirements may be met.'

Gorton (1975)

Weldability is therefore a relative term which depends upon the application of the welded component and the severity of the conditions under which it operates.

1.2.3 Environmental resistance

The environment of a boiler is very harsh. The fireside conditions require material which is resistant to corrosion. In oil fired boilers, the gas is relatively clean but the particles entrained in it contain significant amounts of vanadium and sulphate which are corrosive at high temperatures. All the coal fired boilers use pulverised coal which is mainly low grade containing upto 20% ash. The ash fusion temperature is often relatively low and it contains appreciable amounts of SO_4^{2-}, Cl^- and Na^+. The small particles of ash are generally in the fused state in the combustion chamber and can cause corrosion.

In addition to these major requirements, any candidate materials must be readily available and economical.

1.3 Candidate materials

Ferritic steels provide the bulk of construction materials used in power plant because of their low cost, good availability, relatively easy fabrication and mechanical properties at both high and low temperatures. Bainitic steels are, in general, used in the more highly stressed or higher temperature components. Chromium is the main alloying element in these steels with strengthening being provided by the addition of Mo, V, Nb and W. These additions slow down the rate of transformation and combine with carbon to form fine dispersions of carbides which are more stable and therefore precipitate and coarsen more slowly than cementite in bainite. These dispersions increase the resistance of the matrix to deformation at high and low temperatures and can be used to develop steels with high yield and creep strengths.

Austenitic stainless steels are used in conditions of high temperature and severe corrosion. Corrosion resistance is achieved by the higher chromium contents which stabilise the austenite phase field and also combine with oxygen to form a protective oxide layer on the surface.

As has been mentioned previously, typical service conditions in a boiler might involve temperatures in the range 540–680°C, and no particular alloy is suitable to serve over this entire range. Consequently, the steel offering the most economic advantage in a narrower temperature range is used, necessitating a gradual change in alloy chemistry towards more concentrated alloys as the service temperature rises.

1.3.1 High strength low alloy steels

The most commonly used high strength low alloy steels used are the 1CrMo, $2\frac{1}{4}$CrMo and $\frac{1}{2}$Cr$\frac{1}{2}$Mo$\frac{1}{4}$V types. Typical compositions are given in Table 1.2. These are the preferred materials for heavy section tube plates, pressure vessels and structural components, because they enable an economic wall thickness to be used which can withstand the design pressure. 1CrMo is used where the creep strength of C–Mn steel is insufficient but it offers little improvement in oxidation resistance. $2\frac{1}{4}$CrMo is used extensively as a final superheat for power stations operating at 540°C main steam temperature, however, the creep strength is too low for applications operating at temperatures much above this and the stress–to–rupture values begin to fall off rapidly. It is ductile and readily fabricated and welded using electrodes of the same composition. The $\frac{1}{2}$Cr$\frac{1}{2}$Mo$\frac{1}{4}$V steel is one of the family of Cr–Mo–V steels whose applications range from small items such as bolting to larger components such as steam piping and turbine rotors. Vanadium carbide, VC, is the carbide which is precipitating to provide creep strength.

	Composition/wt%								
Steel	C	Si	Mn	P	S	Cr	Mo	Ni	V
$2\frac{1}{4}$CrMo	0.08–0.15	0.15–0.50	0.40–0.70	0.040	0.040	2.00–2.50	0.90–1.20	–	–
1CrMo	0.056	0.40	0.77	0.010	0.012	1.11	0.44	0.035	0.015
$\frac{1}{2}$Cr$\frac{1}{2}$Mo$\frac{1}{4}$V	0.13	0.23	0.50	0.033	0.055	0.41	0.58	0.25	0.25

Table 1.2: Typical compositions of the commonly used high strength low alloy steels.

1.3.2 High Cr ferritic steels

Increasing the chromium content improves the creep strength and oxidation resistance. The main steel compositions used are 9CrMo and 12CrMo, typical compositions of which are given in Table 1.3. Both of these steels have compositions compatible with a fully transformable microstructure. In order to obtain maximum high temperature properties they are transformed to a fully martensitic structure and then tempered to produce chromium rich carbides.

In Switzerland, high Cr ferritics have been used since 1957 as superheaters and as steam headers since 1975. Their favourable strength in the 500–600°C temperature range permits the use of considerably smaller wall thicknesses than in $2\frac{1}{4}$CrMo. 9CrMo is marginally superior to $2\frac{1}{4}$CrMo in resistance to oxidation by combustion products and can be easily welded using 9CrMo or $2\frac{1}{4}$CrMo electrodes. 12CrMo has the higher creep strength and oxidation resistance of the ferritic steels, however, it does have welding problems in that it requires a high pre–heat and immediate post weld heat treatment.

	Composition/wt%								
Steel	C	Si	Mn	P	S	Cr	Mo	Ni	V
12CrMo	0.20	0.37	0.58	0.035	0.003	11.5	0.92	0.74	0.31
9CrMo	0.14	0.44	0.45	0.012	0.016	8.25	0.84	–	0.019

Table 1.3: Nominal chemical compositions of 12CrMo and 9CrMo steels.

1.4 The use of dissimilar metal welds

If the varying conditions in a power station require the most suitable and economic choice of materials then at some stage joints have to be made between steels of different phase (austenitic–ferritic joints) and/or steels of differing substitutional alloy content (primarily ferritic–ferritic joints). These types of joint will be referred to hereafter as dissimilar metal joints or transition welds. The major problems associated with dissimilar metal welds are the diffusion of carbon across the weld interface and the thermal stresses induced in the joint, both during welding and service, due to the differences in thermal expansion coefficients. These two effects are common to all transition joints (*i.e.* ferritic–ferritic or ferritic–austenitic welds) and are contributing factors in the failure of these joints.

1.4.1 Carbon diffusion in dissimilar metal welds

Carbon diffusion across the weld interface is a significant factor in all dissimilar metal joint failures. The difference in substitutional alloy content on either side of the welded joint results in a gradient of chemical potential[†] of carbon being set up across the interface. Carbon will therefore diffuse down this chemical potential gradient resulting in one side of the interface being denuded of carbon whilst the other side is correspondingly enriched in carbon. The direction of carbon diffusion will, in general, be from the low chromium to the high chromium side of the

[†] The chemical potential of an atom is its mean free energy in a solution of specified composition.

interface even if the average carbon concentrations on both sides of the interface are equal. The result of this diffusion of carbon is that the low alloy side of the weld adjacent to the interface becomes denuded of carbon, whilst the other side becomes correspondingly enriched leading to the formation of a carburised and decarburised zone on either side of the weld interface.

In some cases, the decarburised zone is characterised by large grains of recrystallised ferrite. The major consequence of carbon diffusion is a loss of strength in the carbon depleted region and an increase in hardness in the carburised region. These zones are immediately adjacent to one another and provide a significant change in properties across a narrow region. Attempts have been made to minimise carbon migration by the use of nickel based filler metals such as Inconel, the composition of which is given in Table 1.4. These have the advantage that they have a thermal expansion coefficient intermediate between that of ferrite and austenite thereby reducing the thermal stresses across the interface, and they also reduce the carbon activity gradient between ferrite and austenite. The diffusivity of carbon in Ni–based fillers is lower than in austenitic stainless steel so the extent of carbon migration is reduced. Ryder *et al.* (1986) suggest that the use of Ni–based fillers can effect an improvement in the life of dissimilar metal joints of upto five times over that of austenitic fillers.

	Composition/wt%									
Steel	C	Si	Mn	P	S	Cr	Mo	Ni	V	Fe
Inconel 132	0.08	0.75	1.5	–	0.015	13–17	–	68.0	min	– 11.0

Table 1.4: Composition of Inconel 132

1.4.2 Stresses acting on the joints

By their very nature, dissimilar metal welds are under stress as soon as they are put into service. The welding together of two different metals with different coefficients of thermal expansion results in stresses being set up in the joint which cannot be adequately removed during post weld heat treatment. Further problems arise during service where cyclic conditions of temperature during start up and shut down procedures mean that tangential, longitudinal and radial components of stress are created in the joint due to this difference in thermal expansion coefficients. The pipework in general is also subject to external bending stresses, internal pressures and vibrational loadings which serve to enhance the stressed state of the weld.

1.5 Mechanism of dissimilar metal joint failure

Most of the failure analysis on dissimilar metal welds has been done between austenitic–

ferritic welds or between ferritic/Ni–based filler welds. Although there is some debate in the literature as to whether a universal mode of fracture can be determined for all dissimilar weld joints, three characteristics of failure emerge.

1.5.1 Formation of an oxide notch

In many joints between ferritic and austenitic welds an oxide notch is formed in the ferritic material close to the weld interface. Various authors postulate as to why these notches are formed. Viswanathan *et al.* (1985) have suggested that notch formation could be due to a stress concentration arising from the strength discontinuity at the interface under cyclic load conditions. Alternatively, they propose that general oxidation of the ferritic steel occurs because of the difference in bulk chromium concentration between the ferritic and austenitic steels. Close to the interface, local stresses cause the oxide to crack exposing fresh metal and allowing further oxidation to occur. Once the notch has formed, by either initiation method, it fills with oxide which has a greater volume than the metal consumed. This causes a stress concentration at the tip of the notch which leads to crack propagation. Klueh and King (1982), however, suggest that it is the loss of chromium from the ferritic matrix by the precipitation of chromium carbides, and not the difference in chromium content between the ferritic and austenitic sides of the weld that causes an oxide notch to form. They found that high chromium particles form in the grain boundaries parallel to the fusion line, thereby depleting the surrounding matrix of chromium, and rendering these areas more susceptible to oxidation. This leads to the formation of an oxide notch at the external surface which promotes crack nucleation and propagation. Crack propagation is therefore in the ferritic side of the weld interface and is associated with the carbon depleted zone.

1.5.2 Prior austenite grain boundary cracking

This mode of failure is common when the filler metal is stainless steel. Creep cavitation occurs adjacent to carbides at the prior austenite grain boundaries of the ferrite. This mode of cracking is associated with a carbon depleted zone, but does not occur in joints were gross decarburisation has occurred resulting in the formation of a soft ferrite zone. The creep cavities are orientated relative to the fusion line in a manner indicative of shear stresses resulting from differences in thermal expansion coefficients.

1.5.3 Weld interface cracking

This mode of failure is commonly observed with Ni–based fillers. During service a planar array of globular carbides develops along the fusion line and cracking occurs along this array. Again, this failure is associated with a decarburised zone in the ferrite.

1.6 Techniques to minimise failure

Although there is some contention in the literature as to the exact cause and mode of failure, the various authors all recognise the effects of carbon migration and stress in the failure of transition joints. Consequently, most of the effects in minimising failures have been concentrated around these two areas.

1.6.1 Reduction of carbon migration

The use of Ni fillers has already been discussed earlier in this chapter. Another technique is to use a buttering layer. This is where a layer of a stabilising alloy, such as a Ni based alloy is 'buttered' onto the weld preparation before the weld metal is laid down to provide a barrier to diffusion. Stabilisation techniques are also used on the ferritic side of a ferritic–austenitic weld by the addition of strong carbide formers such as Cr to minimise carbon migration. Another method which has become of technological interest is that of using graded transition joints by hot isostatic pressing of powders. This results in a smoother transition from the high alloy to the low alloy side of the weld and therefore a reduction in the severity of the carbon activity gradient.

1.6.2 Reduction of stress

The reduction of thermal induced stresses can be achieved by a closer match of expansion coefficients in the transition joint components. This can be accomplished by the use of Ni based filler metals, or again by graded transition joints which spread–out the coefficient of thermal expansion mismatch. External stresses due to bending and vibrational loadings can also be minimised.

1.7 Conclusions

Although dissimilar metal welds are necessary in components such as boiler tubing which experience a range of temperatures and pressures, there are inherent problems in their use. Failure of these joints is largely due to the stresses acting on the joint, both internal and external, and to the migration of carbon across the interface. The risk of failure of dissimilar metal joints is reduced by minimising either one of these causes.

CHAPTER 2

Physical Metallurgy of Chromium Steels

2.1 Introduction

During welding, post weld heat treatment and subsequent service, the dissimilar metal weld is subjected to a variety of temperatures and temperature cycles which have an effect on the resultant microstructure. In general, the weld microstructure will consist of allotriomorphic ferrite, bainite and martensite in varying quantities depending on alloy chemistry. The microstructure will then be tempered during post weld heat treatment and during service at the operating temperature. It is therefore important to understand the physical metallurgy and specifically, the tempering characteristics of the steels under investigation.

2.2 Tempering Characteristics

The tempering of martensite in plain carbon and low alloy steels, in general, can be divided into three well–defined but overlapping stages:-

1. Immediately after quenching, the microstructure of the steel will consist of untempered martensite and retained austenite. If the quenched steel is then heated at temperatures up to 200°C metastable ϵ is precipitated from the martensite. During the precipitation there is a corresponding reduction in the carbon concentration of the martensite whose lattice consequently contracts and becomes less tetragonal.
2. At temperatures between 200 and 315 °C, the retained austenite decomposes to ferrite and carbides. This transformation, which is only important in medium or high carbon steels where there is an appreciable amount of retained austenite present, tends to decrease the volume of the steel.
3. The third stage is marked by the precipitation of Fe_3C at the expense of the ϵ–carbide platelets.

In the presence of strong carbide formers, the early stages of tempering are identical to those of a plain carbon steel, but at temperatures above 500°C the cementite is replaced by more stable alloy carbides. It has been suggested that this could constitute a fourth tempering stage. The exact mechanism by which the alloy carbide precipitates is dependent on the particular solute element present. In low chromium steels (<3 wt%), the Fe_3C transforms to Cr_7C_3 by an '*in-situ*' mechanism *i.e.* the Cr_7C_3 is regarded as precipitating within the boundary of the initial Fe_3C. In higher chromium steels the Cr_7C_3 is nucleated separately. It is these

carbides which give rise to secondary hardening and account for the good creep resistance of the steels. In alloys containing a number of carbide forming elements *e.g.* chromium, molybdenum, vanadium, tungsten and niobium, a sequence of alloy carbides may be formed, giving rise to the more complex $M_{23}C_6$ and M_6C carbides at higher tempering temperatures. In this notation "M" indicates a mixture of metal atoms. Nutting (1969) summarises the sequence of carbides as follows:-

Chromium steels

$$Fe_3C \rightarrow Cr_7C_3 \rightarrow M_{23}C_6$$

Molybdenum steels

$$Fe_3C \rightarrow Mo_2C \rightarrow M_6C$$

Vanadium steels

$$Fe_3C \rightarrow V_4C_3 \rightarrow M_6C$$

In comparison with martensite, bainite grows at relatively higher temperatures so some recovery of the microstructure can occur during transformation. Most of the carbon in ordinary bainitic steels is tied up in the form of cementite precipitates which tend to be coarser than those carbides found in tempered martensite. Consequently, the kinetics of secondary hardening reactions for bainite are found to be slower than those for martensite because the cementite particles take longer to dissolve. However, the secondary hardening reaction in bainitic steels is no different from that produced in martensite in that the tempering resistance of the steels is increased in both cases.

2.3 Structure and morphology of carbides forming in Cr–Mo type steels

2.3.1 Cementite

Cementite is an iron–rich carbide having the orthorhombic structure. Cementite can take a large amount of other elements into solution. Manganese in cementite is limited only by the manganese content of the steel and the partitioning coefficient of the element between the carbide and ferrite. Chromium is highly soluble in cementite and in fact upto one fifth of the iron atoms may be replaced by chromium. Hippsley (1981) has also shown that the chromium content in cementite increases with increasing tempering temperature. Molybdenum will dissolve in Fe_3C but only up to a metal-atom ratio of about 0.04.

2.3.2 M_7C_3

This is a chromium rich carbide which has the trigonal structure of Cr_7C_3. M_7C_3 has a very high solubility for iron and manganese and can dissolve molybdenum and vanadium up to metal-

atom ratios of 0.055 and 0.16 respectively. The composition of M_7C_3 remains constant during tempering and, according to Pilling and Ridley (1982), is independent of carbon concentration.

2.3.3 $M_{23}C_6$

The composition of this carbide is dependent on the alloy content of the steel. In steels that are Mo and W free, it occurs as a Cr rich carbide having the face centred cubic structure $Cr_{23}C_6$ according to Woodhead and Quarrell (1965). In the total absence of Cr, in steels containing Mo the composition is $Fe_{21}Mo_2C_6$. Therefore, in steels containing chromium and molybdenum, the actual composition can vary between these two limits. Dyson and Andrews (1969) have shown the composition to be nearer $(FeCr)_{21}Mo_2C_6$ in chromium containing steels. Beech and Warrington (1966) have shown that the transformation to $M_{23}C_6$ occurs by separate nucleation and growth in the matrix.

2.3.4 M_6C

M_6C is a ternary carbide of Fe and Mo. It has a complex cubic structure and compositions in simple ternary systems ranging from Fe_4Mo_3C to Fe_3Mo_3C, but it shows appreciable solubility for other elements, taking into solution chromium and vanadium up to metal–atom ratios of 0.3 and 0.1 respectively. Pilling and Ridley (1982) found that M_6C was enriched in Si which Yu (1989) also found partitioned to M_6C thereby stabilising the carbide and increasing its nucleation rate.

2.3.5 Mo_2C

Mo_2C has the face centered cubic structure and shows considerable solubility for chromium and vanadium. This carbide forms by separate nucleation in the ferrite as fine needle shaped clusters. Initially it is coherent with the matrix which confers maximum hardness but as it grows into needles it loses some of its coherency with the matrix. Baker and Nutting (1959) have shown that acicular Mo_2C may also be formed at prior austenite grain boundaries and appears if austenite is retained on cooling. As with M_6C, Yu (1989) has shown that the precipitation of Mo_2C is accelerated by the presence of Si.

2.4 Carbide precipitation in 1CrMo steels

The initial microstructure of a 1CrMo steel will depend to some extent on the steel composition and method of production but chiefly on the final heat treatment. Microstructural and precipitation studies have been made on 1CrMo steel which had an initial ferrite/pearlite structure (Toft and Marsden, 1961) and on initial ferrite/bainite or fully bainitic structures (Afrouz *et al.* , 1983).

Toft and Marsden found that the microstructural changes that occur during prolonged ageing of a 1CrMo steel are carbide spherodisation and precipitation. These processes occur separately but proceed together. In the ferrite areas, precipitation and growth of M_7C_3 and Mo_2C is evident, whilst in the pearlite areas there is a spherodisation of Fe_3C and the precipitation of M_7C_3 and Mo_2C. From this work, Toft and Marsden propose the following precipitation sequence in 1CrMo steels containing ferrite and pearlite.

$$Fe_3C \rightarrow Fe_3C + Mo_2C \rightarrow M_7C_3 + Mo_2C \rightarrow M_6C$$

The M_6C in this case is Mo rich but contains Cr and Fe.

In the ferrite/bainite structures after long term tempering, Afrouz *et al.* found spherodised Fe_3C in the bainite regions and at the ferrite/bainite boundaries. Mo_2C precipitates in the form of fine needles were present in the ferrite grains. In the bainite regions Afrouz *et al.* suggest a precipitation sequence similar to that found by Baker and Nutting (1959) for $2\frac{1}{4}$CrMo steels. In the ferrite regions the sequence was:-

$$Mo_2C \rightarrow M_6C$$

The fully bainitic structure contained M_7C_3 and M_6C which was not encountered in the predominantly ferritic specimen. An interesting extension of this work was that Afrouz *et al.* (1983) have shown that the chemical composition changes that occur in Fe_3C carbides during ageing can be used to estimate the time/temperature exposure of a component.

2.5 Carbide precipitation in $2\frac{1}{4}$CrMo steels

The major metallurgical advantages of $2\frac{1}{4}$CrMo steel are that it has a high bainitic hardenability so it will transform to a fully bainitic microstructure over a wide range of temperatures, and that it forms stable alloy carbides conferring high temperature stability to the steel. During the tempering process the morphology, distribution and type of carbide will change depending on the time and temperature at which the steel is held.

The precipitation sequence in a quenched $2\frac{1}{4}$CrMo steel, put forward by Baker and Nutting (1959), can be summarised in the form of Figure 2.1 and the flow diagram:-

$$\epsilon\text{-carbide} \longrightarrow \text{cementite} \longrightarrow \begin{matrix} \uparrow \\ \text{cementite} \\ + \\ Mo_2C \end{matrix} \longrightarrow M_{23}C_6 \longrightarrow \begin{matrix} Cr_7C_3 \\ \downarrow \\ M_6C_3 \end{matrix}$$

Pilling and Ridley (1982) suggest a similar precipitation sequence although they found that the cementite dissolved and was replaced by Mo_2C, M_7C_3 and $M_{23}C_6$ which all nucleated

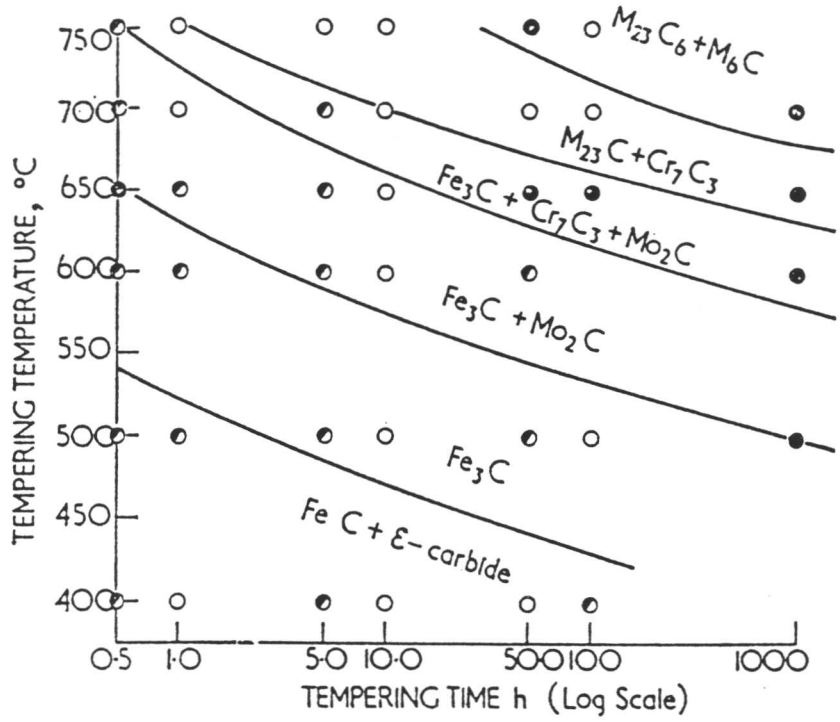

Figure 2.1: Summary of precipitation sequence observed by Baker and Nutting (1959).

simultaneously. Baker and Nutting (1959) found that the Cr_7C_3 precipitated at or within existing cementite particles probably at the interface between the carbide and the ferrite. The precipitate is usually found to have either a rod–like or small parallelogram morphology within the matrix. The precipitation of $M_{23}C_6$ occurs at the grain boundaries separately from M_7C_3 at temperatures above 650°C. The $M_{23}C_6$ grows at the expense of cementite and Mo_2C leading to a decrease in the number of particles present. Baker and Nutting (1959) found no evidence that the Cr_7C_3 dissolved after the formation of $M_{23}C_6$ and therefore concluded that the $M_{23}C_6$ carbide was based on Fe and Mo as if it was Cr rich, it would be expected to grow at the expense of Cr_7C_3. By contrast, Pilling and Ridley found the $M_{23}C_6$ carbide to be high in Cr and low in Mo as shown by its characteristic X-ray spectra in Figure 2.2. The M_6C was initially low in Mo because most it was present in the form of Mo_2C, but as tempering progressed the Mo_2C dissolved and the carbide composition changed to one containing a large concentration of molybdenum.

$M_{23}C_6$ and M_6C are believed to be the stable carbides at 975K and the equilibrium microstructure is expected to be one of M_6C in a ferrite matrix. Klueh and Leitnaker (1975) have disputed this saying that in a multi–component system such as $2\frac{1}{4}$CrMo steel it is possible that two carbides could coexist at equilibrium, and that only very long term heat treatments would resolve this. It is therefore suggested that the equilibrium structure could be one of $M_{23}C_6$ and M_6C. Yu (1989) has shown that the nucleation and growth of carbides is sensitive to the presence of minor alloying additions. Thus, in Si–containing steels, the precipitation sequence

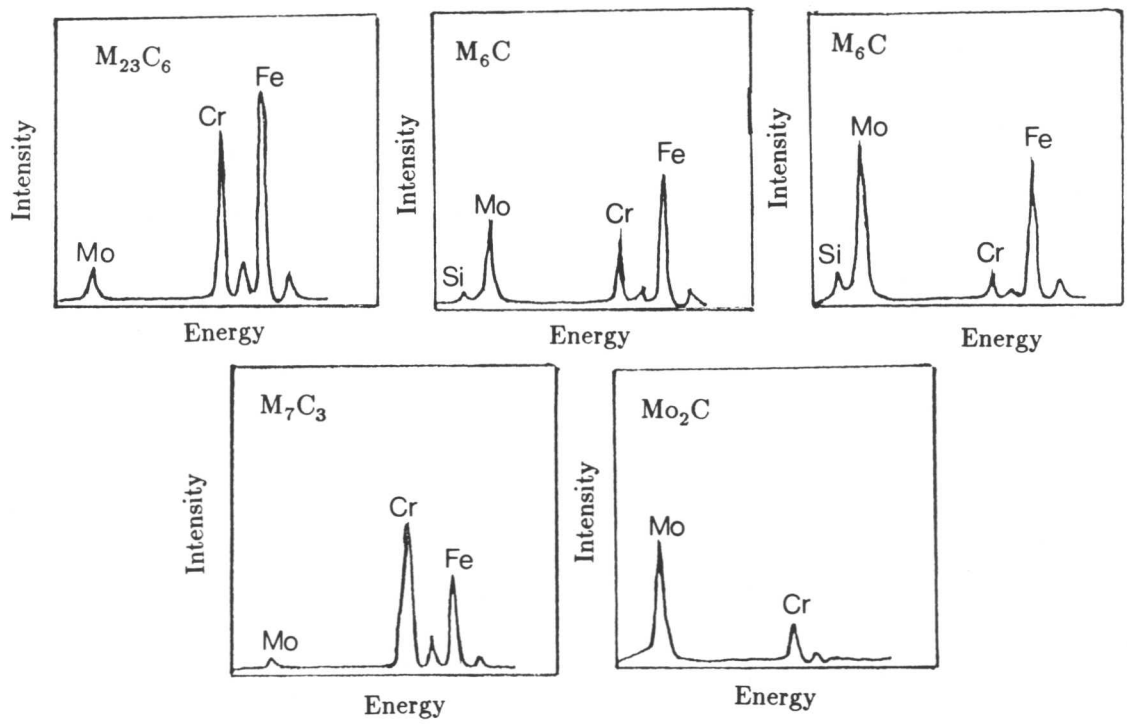

Figure 2.2: Characteristic X-ray spectra of carbides precipitating from $2\frac{1}{4}$CrMo steel.

is given as:-

$$\epsilon\text{–carbide} \rightarrow Fe_3C \rightarrow Mo_2C \rightarrow M_6C \rightarrow M_7C_3 \rightarrow M_{23}C_6$$

Baker and Nutting also studied the precipitation sequences in initially martensitic or ferritic microstructures. With martensite, the sequence was similar to that presented for bainite. The ferrite contained M_2C particles formed during its growth which transformed to M_6C during ageing. Bhadeshia (1992) suggests that the reason for these differences is due to the nature of the transformation in both cases. Ferrite forms by a reconstructive mechanism where the atomic mobility is such that the precipitation of alloy carbides can occur. The displacive nature of the martensitic and bainitic transformations precludes the formation of alloy carbides during transformation.

2.5.1 Morphology

Pilling and Ridley (1982) suggest that there are four distinct carbide morphologies in specimens tempered at 700°C:-

i) globular precipitates at the prior austenite and lath grain boundaries,

ii) rod like precipitates in the matrix,

iii) clusters of needle shaped precipitates in the matrix,

iv) parallelogram shaped particles in the matrix.

Mo_2C has the distinctive needle shaped morphology, and Pilling and Ridley suggest that the grain boundary carbides are M_6C or $M_{23}C_6$ and that the rod shaped precipitates are M_7C_3. However, Balluffi *et al.* (1951) have shown that $M_{23}C_6$ has a spherical shape and Beech and Warrington (1966) have shown that M_7C_3 and $M_{23}C_6$ have similar morphologies. Thus, it can be concluded that the shape of the particle is not a satisfactory guide to identification.

2.6 Tempering characteristics of 9CrMo steel

The composition of 9CrMo is such that it is close to the $\delta/\gamma + \delta$ phase boundary during high temperature heat treatment. Therefore, the structure may contain varying proportions of austenite/δ–ferrite and possibly some undissolved carbides depending on the exact alloy composition and austenitising temperature. The equilibrium phase diagram for the Fe–Cr–0.1wt%C system is given in Figure 2.3.

The presence of carbides and δ–ferrite can cause variations in the transformation characteristics of the austenite and the tempering characteristics of the martensite formed. The microstructures obtained as a function of austenitising temperature are summarised by Pickering and Vassiliou (1980) in Table 2.1. This is particularly important in weldments which are subjected to elevated temperatures and rapid cooling and can therefore contain small amounts of δ–ferrite.

Treatment temperature /°C	Initial structure
900	γ + undissolved α + undissolved $M_{23}C_6$
1000	coarser γ + fine undissolved $M_{23}C_6$
1100	coarse grained γ
1200	γ + 35% δ–ferrite

Table 2.1: Initial microstructures as a function of treatment temperature (Pickering and Vassiliou, 1980).

Sanderson (1977) has carried out studies into the tempering of 9CrMo steel, heat treated in the $\delta + \gamma$ phase field. The normalised microstructure contains lath martensite and auto-tempered M_3C precipitates. Auto-tempering is a process occurring during quenching when carbon atoms can redistribute to low energy sites associated with dislocations or vacancies and precipitate as fine carbides. This is a consequence of the relatively high martensite start (M_s)

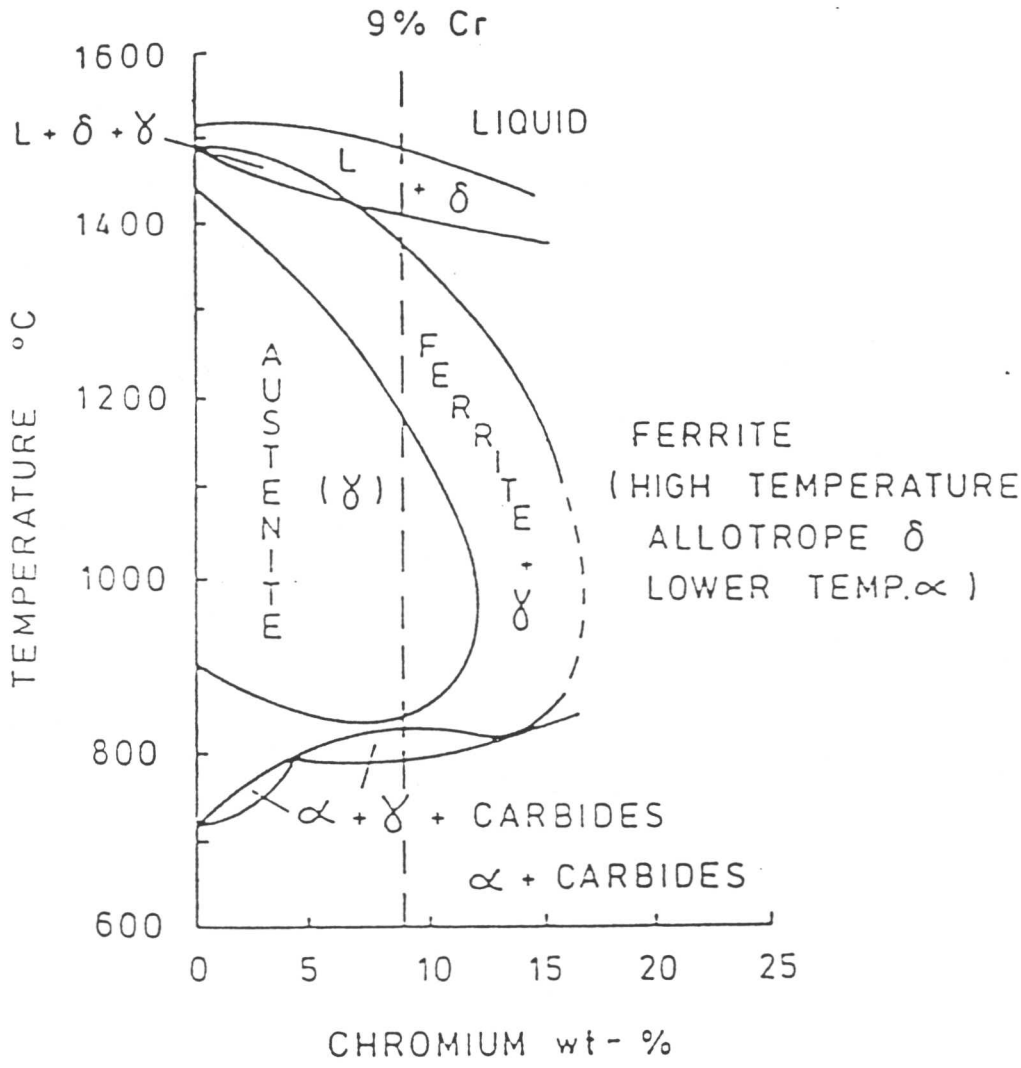

Figure 2.3: Equilibrium diagram for the Fe–Cr–0.1 wt%C. (Sanderson, 1977)

temperature, about 320°C. During the early stages of tempering at 600°C, M_2X needles precipitate at dislocations throughout the matrix, providing some dispersion strengthening and also maintaining a high dislocation density. Tempering proceeds by M_2X precipitate coarsening, decreasing dislocation density and the precipitation of $M_{23}C_6$ at grain and tempered lath martensite boundaries. M_3C is still present in the structure after 8 hours. Sanderson (1977) identified the precipitate M_2X as Cr_2N and $M_{23}C_6$ as $(Fe_5Cr_{18})C_6$. At 700°C no M_3C is observed and the structure is one of coarsened M_2X and $M_{23}C_6$. More severe heat treatments lead to $M_{23}C_6$ precipitate coarsening and the dissolution of M_2X.

The need for a ferritic steel of improved yield strength for use in power plant has led to the development of a modified 9CrMo steel, which differs from the standard 9CrMo by virtue of a tighter compositional specification, the addition of small amounts of niobium, vanadium and nitrogen and the use of a higher austenitising temperature. The compositional differences between the standard and modified 9CrMo steels are illustrated in Table 2.2.

	Composition /wt%	
Element	Standard 9CrMo	Modified 9CrMo
C	0.15 max	0.08–0.2
Mn	0.3–0.6	0.3–0.6
P	0.03 max	0.02 max
S	0.03 max	0.01 max
Si	1.00 max	0.2–0.5
Cr	8.0–10.0	8.0–9.5
Mo	0.9–1.1	0.85–1.05
Ni	–	0.4 max
V	–	0.18–0.25
Nb	–	0.06–0.10
Al	–	0.04 max
N	–	0.03–0.07

Table 2.2: Variation in composition between standard and modified 9CrMo (ASTM A387/A387MG9)

Sikka *et al.* (1983) claim that this modified alloy has a creep strength which exceeds that of standard steels with compositions in the range 2.2-12 wt%CrMo for the temperature range 427-704°C, and can therefore carry higher design stresses. This means that for high temperature components, such as steam headers and pipework, reductions can be made in section size resulting in benefits in terms of material and fabrication requirements and improvement in plant performance.

In the modified 9Cr alloy, the high temperature strength advantage is due to the precipitation of NbC. This fine dispersion of precipitate seems to form in the matrix without regard for dislocations, producing a secondary hardening effect. Panton-Kent (1989) suggests that the higher creep properties arise from the formation of $M_{23}C_6$ containing vanadium.

2.7 Tempering characteristics of 12CrMo steel

It was shown in the previous section that in order to achieve a significantly higher creep rupture strength 9CrMo must be modified by employing other alloying additions or the chromium level has to be raised to about 12wt%. If reference is made to Figure 2.3, it can be seen that for 0.1 wt% C, (which is desirable for ease of welding and good ductility), the austenite loop

is closed at 12.5 wt% Cr. It is important to obtain a fully austenitic structure at the solution treatment temperature to ensure a fully martensitic transformation on cooling. The austenitising temperature is therefore very important. A compromise is sought between a temperature adequate enough to ensure dissolution of the carbides but not so high that δ–ferrite forms, which detracts from the strength of the alloy, or austenite grain growth is excessive, which reduces impact properties. The recommended temperature is 1050°C. This alloy is highly hardenable and can transform to martensite on air cooling even in large section size.

In order to maximise the strength on tempering it is necessary to increase the temper resistance by alloying. The most effective alloying additions for temper resistance are the ferrite stabilisers Mo and V. However, these will tend to produce δ–ferrite at the solution temperature so it is necessary to balance the constitution by the addition of austenite stablilsers Ni, Co, Mn and Cu. An additional concern in making alloying additions is not to depress the martensite start temperature (M_s) below room temperature. Mo and V increase the tempering resistance by the formation of fine M_2X precipitates at the expense of M_7C_3 and the retardation of the transformation to $M_{23}C_6$. M_2X has a close packed hexagonal structure based on $(CrMoV)_2(CN)$ in 12CrMoV steels and in fact, Irvine *et al.* (1960) have shown it to be Cr_2C in 12Cr steels. The precipitation of M_2X causes a secondary hardening peak in the tempering curve and it is also stable over a large temperature range, thereby increasing the tempering resistance. In the overaged condition, $M_{23}C_6$ coarsens and M_2X is replaced by the more stable carbide.

In work on 12CrMoV steels Irvine *et al.* (1960) found that an initial tempered structure contained only Fe_3C at 300°C. At higher temperatures Fe_3C dissolved and M_7C_3 precipitated both '*in–situ*' and by a separate nucleation process as a fine precipitate in the matrix. M_2X precipitated as a fine precipitate within the martensite laths (Murphy and Branch, 1968 and Little *et al.* , 1978). At 500°C, $M_{23}C_6$ was observed at the martensite lath and prior austenite grain boundaries as a coarse precipitate (Murphy and Branch, 1968 and Irvine *et al.* , 1960) which grows at the expense of M_7C_3 on further tempering and accounts for the softening of the structure. Murphy and Branch (1968) propose that the equilibrium carbide will be $M_{23}C_6$, a view which is corroborated by Thomson and Bhadeshia (1992). Using thermodynamic calculations they showed that $M_{23}C_6$ is the equilibrium stable carbide between 400°C and 800°C. This carbide precipitates initially with a composition close to that predicted by thermodynamics and no significant change in composition was detected during tempering.

The precipitates found by Park *et al.* (1980) in a 12CrMoVNb steel can be summarised in Table 2.3. The effect of Nb is to extend the range over which M_2X is stable and thereby increase the temper resistance further.

	10 hours	100 hours	1000 hours
550°C	M_3C, M_7C_3, M_2X	M_7C_3, $M_{23}C_6$, M_2X	$M_{23}C_6$, M_2X
600 °C	M_3C, M_7C_3, M_2X	$M_{23}C_6$, M_2X	$M_{23}C_6$, M_2X
650 °C	M_3C, M_7C_3, M_2X	$M_{23}C_6$, M_2X	$M_{23}C_6$, M_2X

Table 2.3: Precipitates found in 12CrMoVNb steel after Park, *et al.* (1980)

2.8 Equilibrium thermodynamic calculations

The previous sections have outlined the precipitation studies made experimentally on the steels to be used in this investigation. The precipitation sequences have been calculated, using thermodynamic calculations for the exact compositions of the experimental steels, together with the equilibrium carbide compositions. These calculations were made using MTDATA. This is a computer package developed by the NPL which is capable of performing detailed equilibrium calculations for a wide range of alloys. The program utilizes an optimisation routine for minimising the Gibbs free energy of the system. The stable equilibrium phases can be predicted using data obtained from simple systems and experimental evidence. Thus for a given temperature and pressure or volume, plus initial concentrations of the elements in the system, the amounts of elements within each stable phase can be calculated. A precipitation sequence can be determined by calculating the most stable phase, suppressing its formation and performing the calculation again. In all of these calculations, the components allowed for were Fe, Cr, C, Mn, Mo, V, Si, Ni, S and P and the possible phases were ferrite, Fe_3C, Mo_2C, M_7C_3, $M_{23}C_6$ and M_6C. MTDATA has currently no data for the M_2X phase, so this is missing from the precipitation sequences. The precipitation sequences calculated plus the compositions of the phases are presented using the chemical compositions of Table 5.2.

2.8.1 1CrMo

The predicted precipitation sequence for this alloy at 700°C is shown below:-

$$Fe_3C \rightarrow Mo_2C \rightarrow Mo_2C + M_7C_3 \rightarrow M_{23}C_6 \rightarrow M_{23}C_6 + M_6C$$

In comparison with the precipitation sequence of Toft and Marsden (1961), it can be seen that the equilibrium carbides predicted for this alloy are $M_{23}C_6$ and M_6C. However, the composition of the M_6C is as found by Toft and Marsden in that it is Mo rich but contains Fe and Cr. The chemical compositions of the phases are given in Table 2.4.

Phase	Weight fraction of component within phase					
	Fe	Cr	Mn	Mo	C	V
M_6C	0.288	0.019	0.0	0.666	0.025	0.0
$M_{23}C_6$	0.517	0.247	0.00	0.186	0.050	0.0
M_7C_3	0.270	0.796	0.076	0.072	0.085	0.0
Mo_2C	0.009	0.373	0.048	0.470	0.081	0.018
Fe_3C	0.590	0.250	0.072	0.021	0.067	0.0

Table 2.4: Weight fractions of the components within the carbides found in 1CrMo steel.

2.8.2 $2\frac{1}{4}$*CrMo*

The predicted precipitation sequence at 700°C for this alloy is shown below. This sequence seems to provide evidence for the view of Klueh and Leitnaker (1975) that it is possible for two carbides to exist at equilibrium. However, the calculation seems to provide anomalous results concerning the position of Mo_2C in the precipitation sequence as no other workers have found that M_7C_3 dissolves before Mo_2C precipitates. The chemical compositions of the carbides are given in Table 2.5.

$$Fe_3C \rightarrow M_7C_3 \rightarrow Mo_2C \rightarrow Mo_2C + M_{23}C_6 \rightarrow M_{23}C_6 + M_6C$$

Phase	Weight fraction of component within phase					
	Fe	Cr	Mn	Mo	C	V
M_6C	0.279	0.031	0.0	0.665	0.025	0.0
$M_{23}C_6$	0.364	0.391	0.00	0.194	0.050	0.0
M_7C_3	0.172	0.526	0.055	0.165	0.082	0.0
Mo_2C	0.004	0.303	0.025	0.573	0.076	0.018
Fe_3C	0.429	0.407	0.070	0.024	0.068	0.0

Table 2.5: Weight fractions of the components within the carbides found in $2\frac{1}{4}$CrMo steel.

2.8.3 9CrMo

Unfortunately, MTDATA does not allow for the formation of the phase M_2X and therefore the precipitation sequence omits this phase. The calculations show that the carbides formed

are very dependent on the bulk carbon concentration and in this alloy the equilibrium carbide is M_7C_3 at 730°C and not $M_{23}C_6$ as found by Sanderson (1977).

$$Fe_3C \rightarrow Mo_2C \rightarrow Mo_2C + M_7C_3$$

Table 2.6 shows the chemical compositions of carbides formed.

Phase	Weight fraction of component within phase					
	Fe	Cr	Mn	Mo	C	V
M_7C_3	0.069	0.807	0.006	0.028	0.088	0.0
Mo_2C	0.001	0.574	0.004	0.225	0.093	0.104
Fe_3C	0.165	0.750	0.012	0.003	0.071	0.0

Table 2.6: Weight fractions of the components within the carbides found in 9CrMo steel.

2.8.4 12CrMo

This precipitation sequence shows the prediction of $M_{23}C_6$ as the stable carbide at 730°C a result which is verified by Thomson and Bhadeshia (1992) and Murphy and Branch (1968).

$$Fe_3C \rightarrow M_7C_3 \rightarrow M_{23}C_6$$

Table 2.7 gives the chemical compositions of all the carbides calculated.

Phase	Weight fraction of component within phase					
	Fe	Cr	Mn	Mo	C	V
$M_{23}C_6$	0.119	0.651	0.000	0.178	0.052	0.0
M_7C_3	0.059	0.822	0.007	0.023	0.088	0.0
Fe_3C	0.139	0.774	0.012	0.003	0.071	0.0

Table 2.7: Weight fractions of the components within the carbides found in 12CrMo steel.

2.9 Conclusions

The search of the literature has revealed that the tempering characteristics for the chromium steels under investigation is very dependent on the exact composition of the steel,

the treatment prior to tempering, the initial microstructure and the temperature at which tempering occurs. The MTDATA calculations together with the available literature provide a reference base for assessment of the experimental results obtained in the present work.

CHAPTER 3

Modelling of carbon diffusion

3.1 Introduction

The diffusion of atoms will always occur in order to produce a decrease in the Gibbs free energy of the system. This concept is illustrated in Figure 3.1. Consider welding two blocks of the same A-B solid solution together and holding them at some temperature in order to allow diffusion to occur. The Gibbs free energy of the system is also illustrated in Figure 3.1. Thus, the B-rich side of the joint has a free energy G_1 and the A-rich side a corresponding energy G_2. The initial free energy of the block is given by G_3, but if diffusion is allowed to occur between the two sides then the free energy will be reduced to G_4, the free energy of the homogeneous alloy. Thus in this case, a decrease in free energy is achieved by the diffusion of A and B atoms down the resultant concentration gradient which is also parallel to the chemical potential gradient.

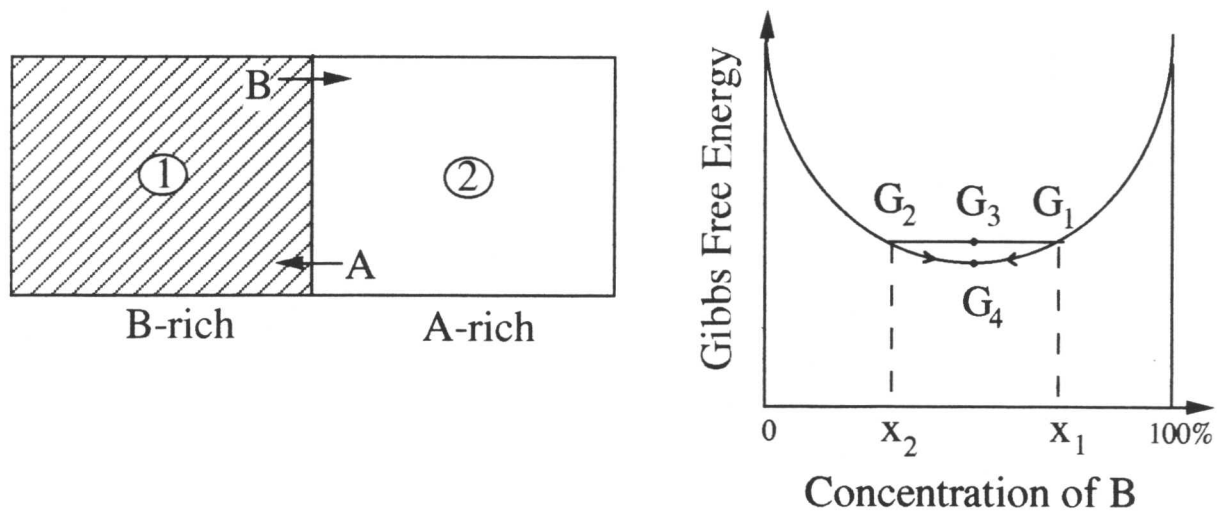

Figure 3.1: Free energy diagram for 'downhill' diffusion (after Porter and Easterling (1981))

Consider now a homogeneous solid solution of composition x made up of components A and B metals whose free energy diagram is as illustrated in Figure 3.2. The initial Gibbs free energy is given by G_3. However, a reduction in free energy in this case is achieved by the development of A–rich and B–rich regions thereby causing an overall decrease in the free energy of the system to G_4. Thus, the system is achieving a lowering of its free energy by diffusion up

a concentration gradient and therefore this type of diffusion is sometimes termed 'uphill' diffusion, even though diffusion is still occurring down a chemical potential gradient. The situation just described is one in which an initially homogeneous solid solution is unstable to infinitesimal composition perturbations. It decomposes by uphill diffusion into an inhomogeneous solution, *i.e.* it spinodally decomposes. This classical description of uphill diffusion proves that diffusion is driven by chemical potential gradients rather than mere concentration gradients. Thus when a transition joint is made between two steels of equal carbon concentration but different substitutional solute content, the chemical potential of carbon on either side may differ. This is because the substitutional solute content alters the chemical potential of the carbon. Consequently, initially homogeneously distributed carbon will partition across the weld junction along this chemical potential gradient, by uphill diffusion to lead to an inhomogeneous distribution. An alternative but equivalent physical explanation is that the attraction for carbon atoms by the substitutional solute on one side of the weld is larger than on the other.

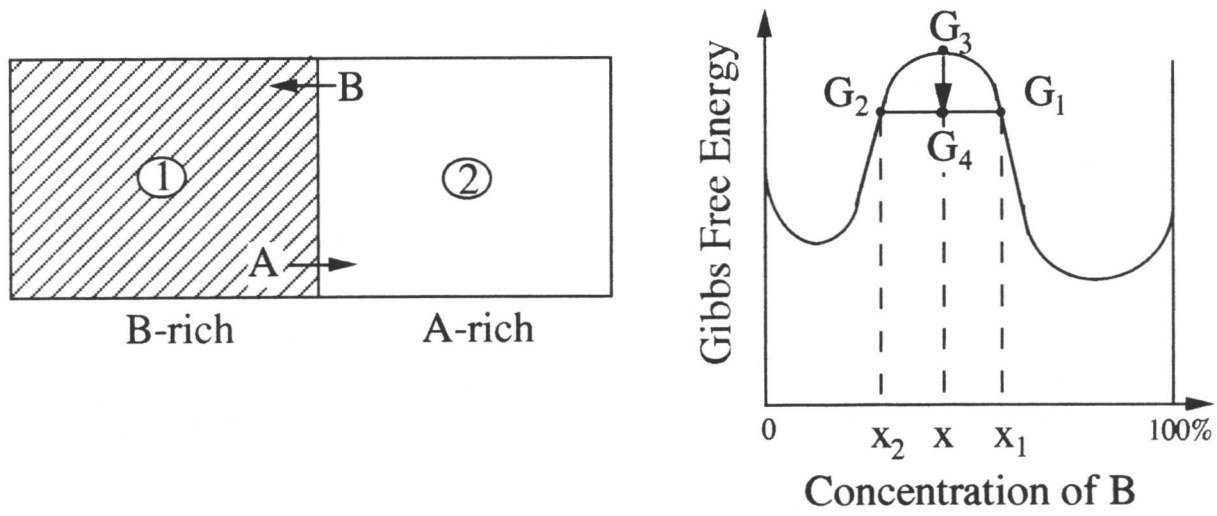

Figure 3.2: Free energy diagram for 'uphill' diffusion (after Porter and Easterling (1981)).

3.2 Mechanisms of diffusion

There are two methods of diffusion operative in crystal lattices dependent on the site that the diffusing atom occupies in the lattice *i.e.* whether it is a substitutional or interstitial atom. In the modelling of carbon diffusion in either the ferritic or austenitic phase field, it is the interstitial mechanism which is of interest as the free carbon available for diffusion is found in the interstices of both lattices.

3.2.1 Interstitial diffusion

3.2.1.1 Derivation of Ficks first law

Consider a model consisting of a simple cubic lattice of A atoms in which the interstices between atoms are filled with the interstitial atom B. The B atoms are arranged such that every A atom is surrounded by 6 interstital sites into which the B atoms can fit without causing any distortion in the A lattice. If a concentration gradient is set up as shown in Figure 3.3 then the B atoms will tend to diffuse by a random walk process (*i.e.* the direction of each new jump is independent of the direction of the previous jump) to eliminate the gradient.

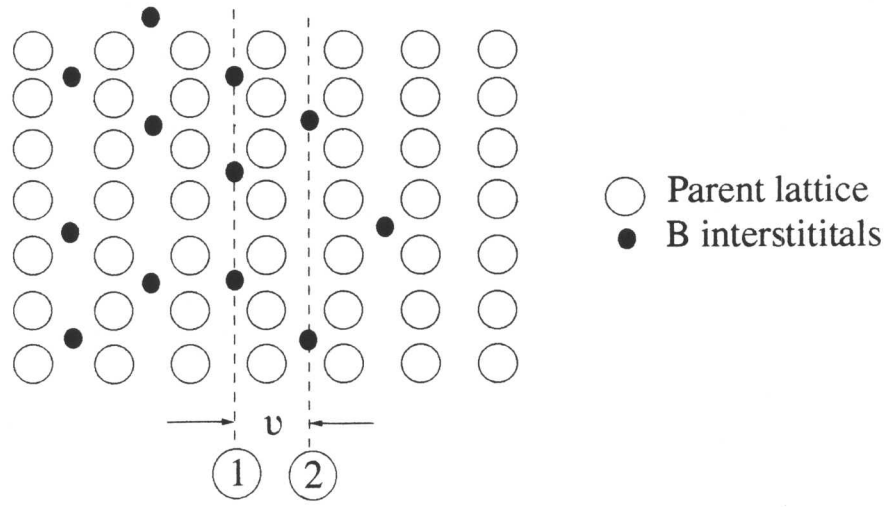

Figure 3.3: Planes of A atoms and a concentration gradient of interstitial B atoms. (after Porter and Easterling (1981))

If the diffusion of a B atom from plane 1 to plane 2 is considered, assuming that, on average, an interstitial atom jumps Γ_B times per second and there are n_1 B atoms/m^2 that will jump from plane 1 to plane 2, then the flux of B atoms will be given by:-

$$\overrightarrow{J} = \frac{1}{6}\Gamma_B n_1 \tag{3.1}$$

However, if each atom can jump in any direction and Γ_B is independent of concentration, then there is also a corresponding flux from plane 2 to plane 1 of:-

$$\overleftarrow{J} = \frac{1}{6}\Gamma_B n_2 \tag{3.2}$$

Now, because of the concentration gradient, $n_1 > n_2$, and therefore, a net flux from left to right can be defined as:-

$$J_B = \frac{1}{6}\Gamma_B (n_1 - n_2) \tag{3.3}$$

n_1 and n_2 can be translated into concentrations if the separation of the planes is taken to be v, then the concentration of B atoms on plane 1 is given by:-

$$C_{B_1} = \frac{n_1}{v} \tag{3.4}$$

and similarly for plane 2:-

$$C_{B_2} = \frac{n_2}{v} \tag{3.5}$$

The difference between n_1 and n_2 is therefore given by:-

$$n_1 - n_2 = v(C_{B_1} - C_{B_2}) \tag{3.6}$$

However, with reference to Figure 3.4, it can be seen that $(C_{B_1} - C_{B_2})$ can be expressed as:-

$$(C_{B_1} - C_{B_2}) = -v\frac{\partial C_B}{\partial z} \tag{3.7}$$

Therefore, substitution into (3.3) yields the following expression for the net flux of atoms:-

$$J_B = -\left(\frac{1}{6}\Gamma_B v^2\right)\frac{\partial C_B}{\partial z} \tag{3.8}$$

If a diffusion coefficient is defined such that:-

$$D_B = \frac{1}{6}\Gamma_B v^2 \tag{3.9}$$

then (3.8) reduces to:-

$$J_B = -D_B\frac{\partial C_B}{\partial z} \tag{3.10}$$

This equation is known as Ficks First Law of Diffusion. The diffusion coefficient defined in equation (3.9) is only strictly applicable when the jumping of B atoms is truly random with a frequency independent of concentration. However, in many crystal systems this is found not to be the case and in fact the diffusion coefficient is dependent on crystal direction (*e.g.* atoms in hexagonal lattices diffuse at different rates parallel and perpendicular to the basal plane) or concentration. However, Ficks first law is still found to hold if appropriate concentration dependent expressions are substituted for the diffusion coefficient.

3.2.2 Ficks Second Law - non steady state diffusion

Ficks first law is only applicable for steady state diffusion conditions, *i.e.* where the concentration at any point does not change with time. This cannot, therefore, be applied to a system like a transition joint where the concentration at any point is constantly changing with both time and distance *i.e.* under non-steady state conditions. In order to deal with these conditions

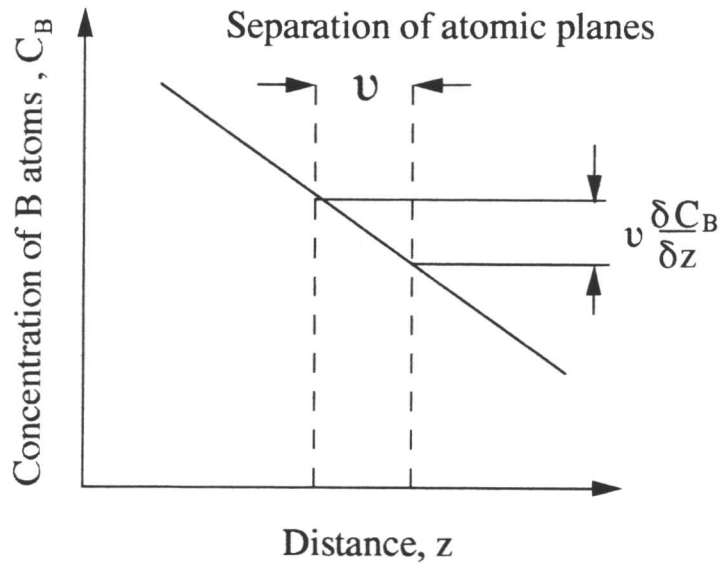

Figure 3.4: Illustration of the gradient of B atoms (after Porter and Easterling (1981))

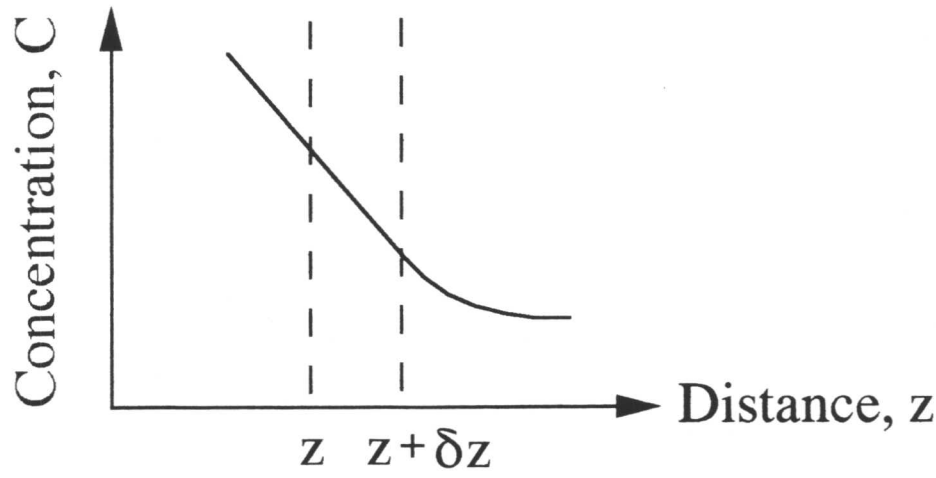

Figure 3.5: Concentration gradient of interstitial B atoms in one–dimension. (after Porter and Easterling (1981))

consider the situation illustrated in Figure 3.5 where a concentration gradient exists in the z direction only.

As in the derivation of Ficks first law, the B atoms are still diffusing interstitially down this concentration gradient. In order to calculate how the concentration of B varies with time, consider a thin slice of material of area A and thickness δz as shown in Figure 3.6. In a time δt the number of B atoms that will have diffused into this slice is given as $J_1 A \delta t$. However,

under non-steady state conditions, the number of atoms that will have diffused out of the slice is given by $J_2 A\delta t$ where $J_1 > J_2$ causing a net increase in the number of B atoms in the slice of:-

$$\delta n_B = (J_1 - J_2)A\delta t \tag{3.11}$$

and therefore, a net increase in the concentration of B atoms in the slice of:-

$$\delta C_B = \frac{(J_1 - J_2)A\delta t}{A\delta z} \tag{3.12}$$

Now, since δz is small then J_2 can be written as:-

$$J_2 = J_1 + \frac{\partial J}{\partial z}\delta z \tag{3.13}$$

which on substitution into (3.12) and in the limit as $t \to 0$:-

$$\frac{\partial C_B}{\partial t} = -\frac{\partial J_B}{\partial z} \tag{3.14}$$

Substituting for Ficks first law in the above expression gives:-

$$\frac{\partial C_B}{\partial t} = -\frac{\partial}{\partial z}\left(D_B \frac{\partial C_B}{\partial z}\right) \tag{3.15}$$

If D_B does not depend on C_B, this equation simplifies to:-

$$\frac{\partial C_B}{\partial t} = D_B \frac{\partial^2 C_B}{\partial z^2} \tag{3.16}$$

which is known as Ficks Second Law and is the basis for many of the models concerning the diffusion of carbon in dissimilar metal welds.

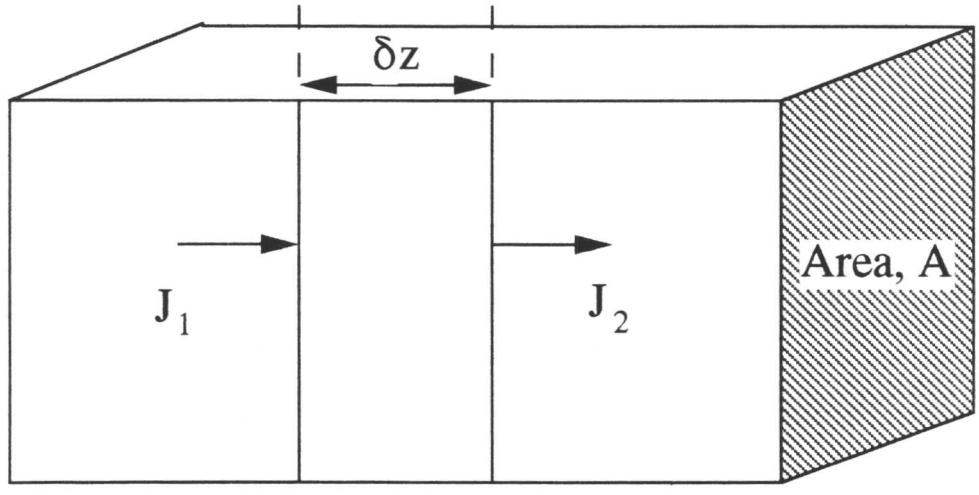

Figure 3.6: Derivation of Ficks Second Law (after Porter and Easterling (1981))

3.3 Carbon diffusion across dissimilar metal joints in the austenite phase field - review and critique of published work

There have been various analytical models proposed for the modelling of 'uphill' diffusion of carbon in austenitic joints using the classical data of Darken (1949). In these experiments steels of virtually the same carbon content, but differing in substitutional solute concentration, were welded together and held at 1050°C for about two weeks. The compositions of the steels welded are shown in Table 3.1.

		C	Mn	**Si**	P	S	Cr
Steel A	wt%	**0.49**	0.25	**3.80**	0.011	0.006	0.31
Steel B	wt%	**0.04**	0.28	**4.78**	0.006	0.011	–
Steel C	wt%	**0.45**	0.88	**0.05**	0.02	0.008	–

Table 3.1: Composition of the steels used in the Darken experiment. The carbon and silicon concentrations are highlighted to outline the differences between the steels and the main contributors to the diffusion.

After heat treatment, the specimens were sliced at various distances from the fusion line and analysed for carbon. The profiles thus obtained are given in Figure 3.7.

The aim of any model is to predict carbon concentration profiles such as those above in which the carbon is diffusing down a gradient of chemical potential and up a gradient of concentration. On reviewing the literature, it was apparent that the types of models fell into two categories, those that would predict Darken's data and those that required the data for fitting equations describing the variation in solute concentration as a function of distance from the weld junction, but assuming that the concentrations at the junction are known from experiments. These two categories of model will now be discussed.

3.3.1 Category 1 : Prediction of Darken's profiles

There are three published models that propose equations for the prediction of carbon concentration profiles under the influence of a chemical potential gradient. In chronological order, these are due to Stark (1980), Agren (1983) and Bhadeshia (1988). However, on studying the methods by which the solutions were obtained it was discovered that all the models start with the equation for the continuity of matter (Fick's second law) and apply certain boundary conditions to solve this equation. Thus all three models arrive at the same set of equations. This general method will now be explained.

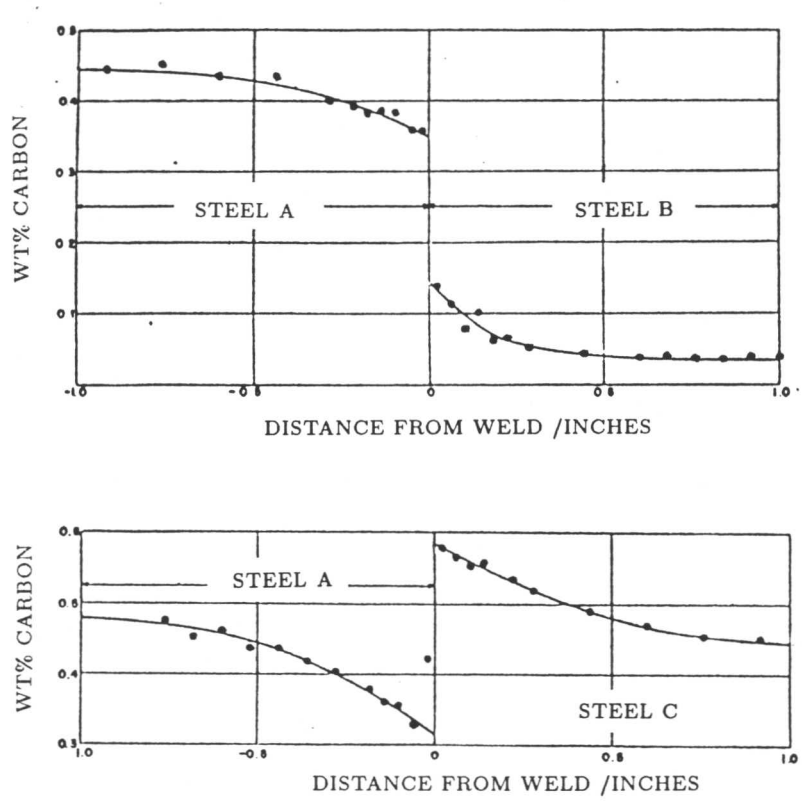

Figure 3.7: Darken profiles for welds A–B and A–C.

3.3.1.1 Solution of Fick's second law

The situation of diffusion in a system where two media are present can be treated as a combination of two semi–infinite media in which the surface concentration remains constant. This is shown diagramatically in Figure 3.8 where a diffusion couple is formed between two alloys which vary in substitutional alloy content such that redistribution of carbon will tend to occur from α to θ.

Fick's second law can be written as:-

$$\frac{\partial x}{\partial t} = D\frac{\partial^2 x}{\partial z^2} \tag{3.17}$$

where x is the concentration of carbon, z is the position, t is time and D is the diffusion coefficient. Onsager (1945–46) proposed a logical extension of Fick's Law, that the flux of a given element in a multi–component system can be represented as a linear function of the concentration gradients of all other elements (and, of course, of itself), *viz.*,

$$J_i = -\sum_{k=1}^{n} D_{ik}\frac{\partial x_k}{\partial z}$$

where the D_{ik} are functions of all the concentrations x_k. It should be noted here that this applies to concentration independent diffusion coefficients, although the diffusion coefficient of

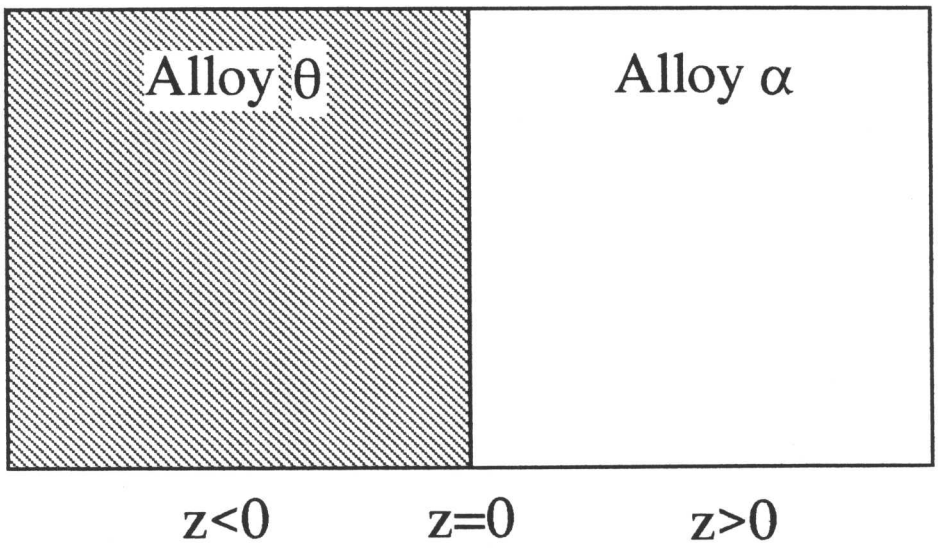

Figure 3.8: Schematic representation of the diffusion couple.

carbon in austenite is concentration dependent. However, if it is assumed that the composition of Si is time independent, consistent with its relatively slow diffusion rate, then the flux can again be expressed as equation (3.17).

The Laplace transform solutions to this equation are given as:-

$$x^{\alpha} = A_1 + B_1 \mathrm{erf}\{\frac{z}{2\sqrt{D_{\alpha} t}}\} \tag{3.18}$$

$$x^{\theta} = A_2 + B_2 \mathrm{erf}\{\frac{|z|}{2\sqrt{D_{\theta} t}}\} \tag{3.19}$$

In this equation the term α refers to the α side of the weld and the term θ to the θ side. A and B are constants whose values can be found from the boundary conditions.

3.3.1.2 The boundary conditions

1. Continuity of chemical potential across the interface.

The chemical potential must be continuous across the weld, therefore:-

$$\mu_{\alpha\theta} = \mu_{\theta\alpha} \tag{3.20}$$

Now

$$\mu = \mu_o + RT\ln a_c \tag{3.21}$$

so

$$\mu_o + RT\ln a_c^{\alpha\theta} = \mu_o + RT\ln a_c^{\theta\alpha} \tag{3.22}$$

a_c is the activity of carbon in austenite, and the superscript $\alpha\theta$ refers to the α/θ boundary. Similarly, the superscript $\theta\alpha$ refers to the θ/α boundary, *i.e.* when z=0.

μ_o is the partial molar free energy of the pure substance in the standard state.

Since the phase on either side of the interface is austenite then the value of the partial molar free energy will be the same, therefore:-

$$RT\ln a_c^{\alpha\theta} = RT\ln a_c^{\theta\alpha} \tag{3.23}$$

therefore

$$a_c^{\alpha\theta} = a_c^{\theta\alpha} \tag{3.24}$$

so

$$x^{\alpha\theta}\Gamma_\alpha = x^{\theta\alpha}\Gamma_\theta \tag{3.25}$$

since

$$a_c = x\Gamma \tag{3.26}$$

where Γ is the activity coefficient of carbon. If the partition coefficient is defined as:-

$$k = \frac{\Gamma_\alpha}{\Gamma_\theta} \tag{3.27}$$

then

$$x^{\theta\alpha} = kx^{\alpha\theta} \tag{3.28}$$

So applying this condition to (3.18) and (3.19) when z=0 $A_1 = x^{\alpha\theta}$ and $A_2 = x^{\theta\alpha}$ but,

$$k = \frac{x^{\theta\alpha}}{x^{\alpha\theta}} = \frac{A_2}{A_1} \tag{3.29}$$

which rearranges as:-

$$A_2 = kA_1 \tag{3.30}$$

2. Continuity of flux across the interface.

The flux across the interface must be continuous therefore, there must be no build up of solute at the α/θ interface, *i.e.* the flux leaving α must be equal to the flux entering θ *i.e.* $J_\alpha = J_\theta$

It follows that

$$D_\alpha \frac{\partial x^\alpha}{\partial z}\Big|_{z=0} = -D_\theta \frac{\partial x^\theta}{\partial z}\Big|_{z=0}$$

from Fick's first law.

Applying this condition to equations (3.18) and (3.19) and differentiating with respect to z :-

$$\frac{2}{\sqrt{\pi}}D_\alpha B_1 \exp\{\frac{-z^2}{4D_\alpha t}\}\frac{1}{2\sqrt{D_\alpha t}} = -\frac{2}{\sqrt{\pi}}D_\theta B_2 \exp\{\frac{-z^2}{4D_\theta t}\}\frac{1}{2\sqrt{D_\theta t}}$$

(The method for differentiation of the error function is given in Appendix I) Therefore when z=0

$$\frac{D_\alpha B_1}{2\sqrt{D_\alpha t}} = -\frac{D_\theta B_2}{2\sqrt{D_\theta t}} \tag{3.31}$$

$$B_2 = -\sqrt{\frac{D_\alpha}{D_\theta}}B_1 \tag{3.32}$$

If the carbon concentration is not the same on both sides of the weld:-

when $z=\infty$ erf(∞)=1, $x^\alpha = x^{\alpha o}$ and $x^\theta = x^{\theta o}$ so, from (3.18) and (3.19)

$$x^{\alpha o} = A_1 + B_1 \tag{3.33}$$

$$x^{\theta o} = A_2 + B_2 \tag{3.34}$$

substituting from (3.30) and (3.32) into (3.34)

$$x^{\theta o} = kA_1 - \sqrt{\frac{D_\alpha}{D_\theta}}B_1 \tag{3.35}$$

rearranging (3.33)

$$x^{\alpha o} - A_1 = B_1$$

and substituting into (3.35)

$$x^{\theta o} = kA_1 - \sqrt{\frac{D_\alpha}{D_\theta}}(x^{\alpha o} - A_1) \tag{3.36}$$

$$x^{\theta o} = kA_1 - x^{\alpha o}\sqrt{\frac{D_\alpha}{D_\theta}} + \sqrt{\frac{D_\alpha}{D_\theta}}A_1 \tag{3.37}$$

$$A_1 = \frac{x^{\theta o} + x^{\alpha o}\sqrt{\frac{D_\alpha}{D_\theta}}}{k + \sqrt{\frac{D_\alpha}{D_\theta}}} \tag{3.38}$$

and

$$B_1 = x^{\alpha o} - A_1$$

therefore (3.18) and (3.19) rearrange as

$$x^\alpha = A_1 + (x^{\alpha o} - A_1)\mathrm{erf}\{\frac{z}{2\sqrt{D_\alpha t}}\} \tag{3.39}$$

$$x^\theta = kA_1 + \sqrt{\frac{D_\alpha}{D_\theta}}(x^{\alpha o} - A_1)\mathrm{erf}\{\frac{|z|}{2\sqrt{D_\theta t}}\} \tag{3.40}$$

From these equations the carbon concentration can be calculated at any position z if the value of the partition coefficient is known. As Stark points out in his paper the value of the partition coefficient is given simply by the ratio of the activity coefficients (equation (3.27)).

3.3.2 Category 2 : Fitting of Darken's profiles

There are two workers who have published models that will fit Darken's profiles as long as fitting parameters taken from the data are used. These are Kirkaldy (1957) and Kucera and Stransky (1982). As in the previous case the models are very similar in their derivation of the equations and a general method can again be discussed. The starting point is again Fick's second law.

Onsager (1945-46) proposed as a logical extension of Fick's Law, that the fluxes in a multi-component system can be represented as linear functions of the concentration gradients, *viz.*,

$$J_i = -\sum_{k=1}^{n} D_{ik} \frac{\partial x_k}{\partial z} \tag{3.41}$$

where the D_{ik} are functions of all the x_k.

In a one dimensional system such as the semi-infinite diffusion couple the above equation becomes, for the two independent components:-

$$\frac{\partial x_C}{\partial t} = \frac{\partial D_{11}}{\partial z}\frac{\partial x_C}{\partial z} + \frac{\partial D_{12}}{\partial z}\frac{\partial x_{Si}}{\partial z} \tag{3.42}$$

and

$$\frac{\partial x_{Si}}{\partial t} = \frac{\partial D_{21}}{\partial z}\frac{\partial x_C}{\partial z} + \frac{\partial D_{22}}{\partial z}\frac{\partial x_{Si}}{\partial z} \tag{3.43}$$

where, x_C is the concentration of carbon and x_{Si} is the concentration of Si. For this situation the subscript 1 refers to carbon, subscripts greater than 1 refer to metal (in the case of the Darken experiment this metal is silicon), thus D_{12} for example represents the effect of the gradient of Si concentration on the flux of carbon. For the initial and boundary conditions corresponding to the semi-infinite diffusion couple, the solutions have the general form described by Fujita and Gosting (1956):-

$$x_i = x_i(\lambda) \tag{3.44}$$

where $\lambda = \frac{z}{\sqrt{t}}$ and more specifically,

$$x_C = a\ \mathrm{erf}(\frac{\lambda}{2\sqrt{u}}) + b\ \mathrm{erf}(\frac{\lambda}{2\sqrt{v}}) + c \tag{3.45}$$

where $a - f$ are functions of D_{ik} and u and v are functions of D_{ik} and the boundary conditions. These equations take a simple form when component 1 is more rapidly diffusing than component 2 as D_{21}=0. Kirkaldy (1957) showed that the equation for the carbon profiles becomes:-

$$x_C = \frac{x^{\theta o} + x^{\alpha o}}{2} + A[\mathrm{erf}(\frac{\lambda}{2\sqrt{D_{22}}}) - \frac{2A - x^{\theta o} + x^{\alpha o}}{2A}\mathrm{erf}(\frac{\lambda}{2\sqrt{D_{11}}})] \tag{3.47}$$

where $A = \frac{D_{12}}{D_{11}-D_{12}} \frac{x^{\theta o}-x^{\alpha o}}{2}$ and is found by fitting the results to the equations. The result of fitting the equations to Darken's data is shown in Figure 3.9.

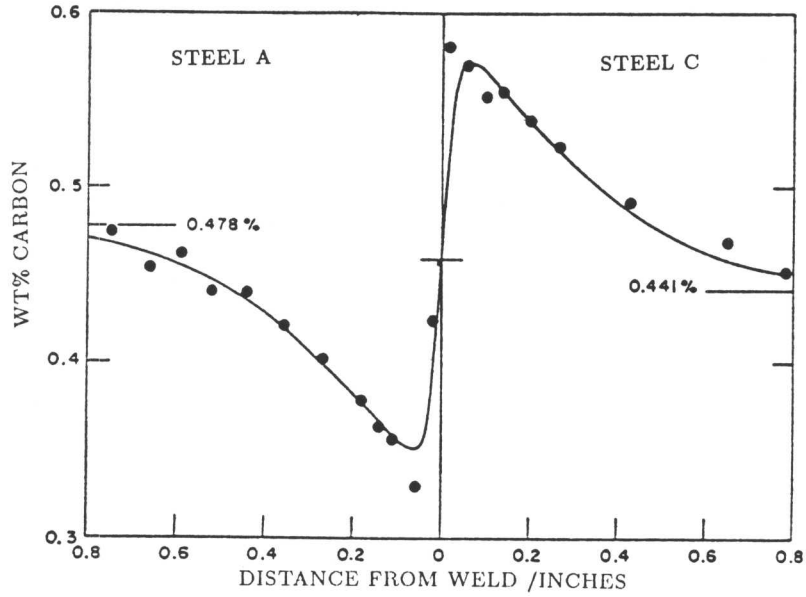

Figure 3.9: Darken's diffusion profiles after Kirkaldy (1957).

The problems with this model are that:-

1.) There is the same carbon concentration in the austenite on both sides of the weld at the interface, therefore the activity of carbon cannot be the same, so this is incorrect.

2.) The plot implies uphill diffusion within a single phase. There is no justification for this.

In some later work, Kirkaldy (1958) interpreted Darken's results as showing a sharp discontinuity at the boundary, then:-

$$D_{11}D_{22} \cong D_{21}D_{12} \tag{3.48}$$

must apply. The fit in this case was found to be much better (Figure 3.10).

Kucera and Stransky also start with the Fujita and Gosting solution to obtain an

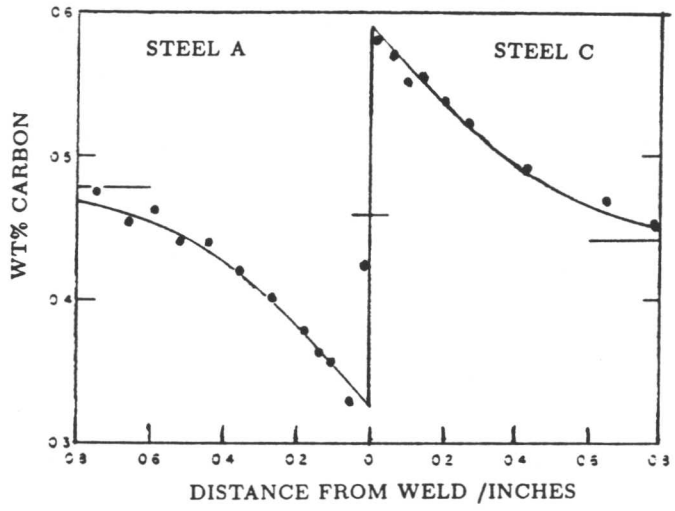

Figure 3.10: Darken's diffusion profiles after Kirkaldy (1958).

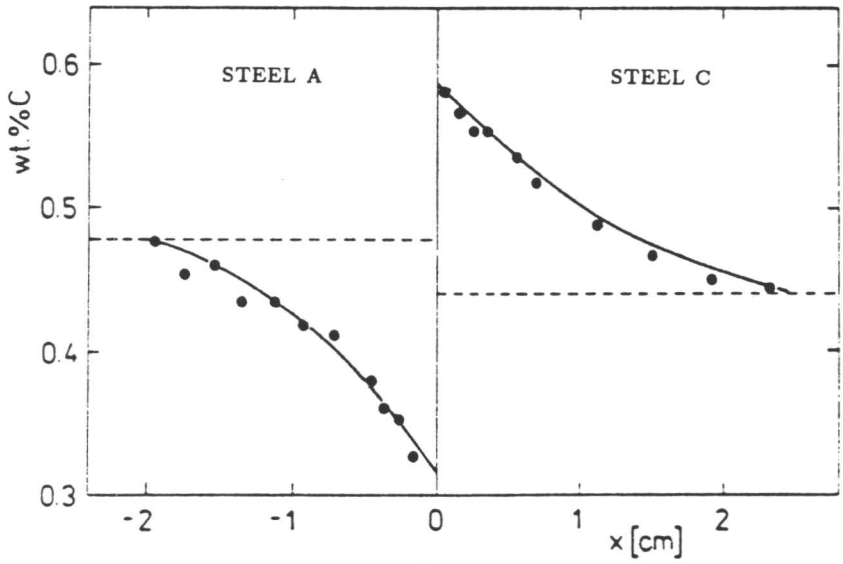

Figure 3.11: Darken's diffusion profiles after Kucera and Stransky (1982).

An interesting extension of Kucera and Stransky's work is that they use the Darken data to obtain further thermodynamic data, specifically the interaction coefficients for Si, Cr, Mn and Mo.

3.4 Carbon diffusion across dissimilar metal joints in the ferrite phase field - review and critique of published work

and is not as readily available for diffusion as was the case in austenite when all the carbon is in the interstitial sites. There have been two major models that address the problems of carbon diffusion in the ferritic phase field, that due to Buchmayer *et al.* (1989) and that of Christoffel and Curran (1956).

3.4.1 Model due to Buchmayer et al. (1989)

Consider that the initial situation is one of a conglomerate phase of cementite and ferrite and carbon diffuses out of this conglomerate phase to form pure ferrite (Figure 3.12). The analytical solution for this situation is given by Jost (1960) after Wagner.

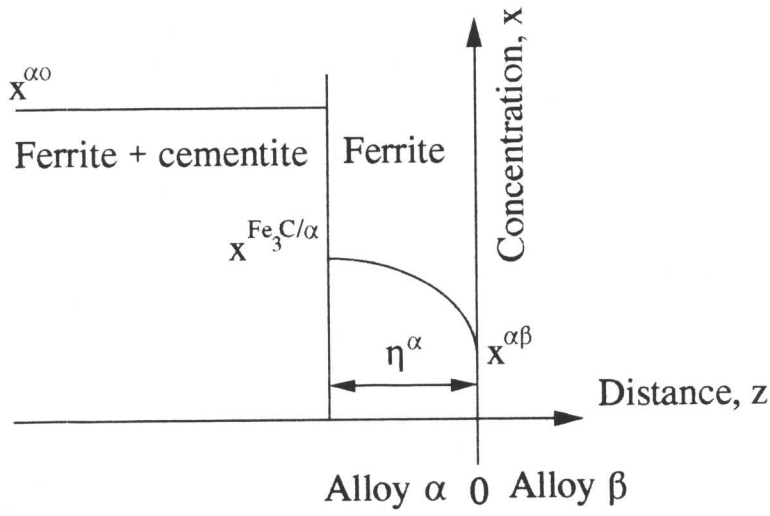

Figure 3.12: Model for diffusion in a two phase system.

At the surface, $z = 0$, the conditions of continuous activity across the interface impose a surface concentration $x^{\alpha\beta}$. The diffusion will proceed from the surface and after a time t will have extended to a distance $z = \eta^{\alpha}$, where η^{α} can be described by the parabolic growth equation as:-

$$\eta^{\alpha} = 2\xi\sqrt{Dt} \tag{3.49}$$

where ξ is a dimensionless parameter.

The diffusion process will be governed by Fick's second law such that:-

$$\frac{\partial x}{\partial t} = D\frac{\partial^2 x}{\partial x^2} \tag{3.50}$$

Now the boundary conditions for this situation are:-

And when $z = \eta^{\alpha}$, the concentration of carbon in pure ferrite is that corresponding to equilibrium between ferrite and cementite, so $x = x^{Fe_3C/\alpha}$ at $z = \eta^{\alpha}$.

When the interface between the ferrite/cementite 'phase' and the ferrite 'phase' is placed by a distance $\partial\eta$ in time ∂t, the amount of solute that must be supplied is

$$[x^{Fe_3C/\alpha} - x^{\alpha o}]\partial\eta$$

per unit area.

$$x = [x^{Fe_3C/\alpha} - x^{\alpha o}]\partial\eta = -D\partial t(\frac{\partial x}{\partial z}) \tag{3.51}$$

A particular solution for this is:-

$$x = x^{\alpha\beta} - B\text{erf}(\frac{z}{2\sqrt{Dt}}) \tag{3.52}$$

for $0 < z < \eta^{\alpha}$ and B is a constant. So when $z = \eta^{\alpha}$, from equation (3.52),

$$x^{Fe_3C/\alpha} = x^{\alpha\beta} - B\text{erf}(\xi) \tag{3.53}$$

Integrating (3.52) gives

$$\frac{\partial x}{\partial z} = \frac{-2}{\sqrt{\pi}}B\exp(\frac{z^2}{4Dt})\frac{1}{2\sqrt{Dt}} \tag{3.54}$$

So, when $z = \eta^{\alpha}$

$$\frac{\partial x}{\partial z} = \frac{-2}{\sqrt{\pi}}B\exp(-\xi^2)\frac{1}{2\sqrt{Dt}} \tag{3.55}$$

Also,

$$\frac{\partial\eta}{\partial t} = \frac{\sqrt{D}\xi}{\sqrt{t}}$$

So substitution into (3.51) gives:-

$$[x^{Fe_3C/\alpha} - x^{\alpha o}]\frac{\sqrt{D}\xi}{\sqrt{t}} = \frac{2D}{\sqrt{\pi}}B\exp(-\xi^2)\frac{1}{2\sqrt{Dt}} \tag{3.56}$$

$$[x^{Fe_3C/\alpha} - x^{\alpha o}] = \frac{B}{\sqrt{\pi}\xi}\exp(-\xi^2) \tag{3.57}$$

Eliminating B from (3.53) and (3.56)

$$\frac{x^{\alpha\beta} - x^{Fe_3C/\alpha}}{x^{Fe_3C/\alpha} - x^{\alpha o}} = \sqrt{\pi}\xi\exp\{-\xi^2\}\text{erf}\xi \tag{3.58}$$

Using an iterative procedure a value of ξ can be found so that the width of the decarburised zone can be calculated using equation (3.49). If the Onsager extension of this equation is considered:-

$$J_k = -\sum_{j}^{n} D_{kj}\frac{\partial x_k}{\partial}$$

Kirkaldy and Young (1987) have shown that for steady state conditions in a three component system this equation becomes:-

$$-D_{11}\frac{\partial x_1}{\partial z} - D_{12}\frac{\partial x_2}{\partial z} = 0 \tag{3.59}$$

Therefore

$$\frac{\partial x_1}{\partial z} = -\frac{D_{12}}{D_{11}}\frac{\partial x_2}{\partial z} \tag{3.60}$$

On integration, the result

$$\Delta x_1 = -\frac{D_{12}}{D_{11}}\Delta x_2 \tag{3.61}$$

is obtained, where Δx_1 is the difference in carbon concentration at the interface *i.e.* ($x^{\beta\alpha}$ - $x^{\alpha\beta}$) and Δx_2 is the difference in concentration of the other metal at the interface *i.e.* ΔCr assuming no diffusion of substitutional elements. Now it was shown by Bhadeshia (1985), that

$$\frac{D_{12}}{D_{11}} = \frac{\epsilon_{12}x_1}{1+\epsilon_{11}x_1} \tag{3.62}$$

ϵ_{ik} is the Wagner interaction coefficient between element i and element k. Again, the subscript 1 refers to carbon and the subscript 2 refers to the alloying element. If x_1, the carbon concentration in solution in the ferrite, is taken to be very small, then this reduces to:-

$$\frac{D_{12}}{D_{11}} = \epsilon_{12}x_1 \tag{3.63}$$

so equation (3.61) becomes

$$\Delta x_1 = -\epsilon_{12}x_1\Delta x_2 \tag{3.64}$$

Now a third condition is required in order to fulfil the mass balance in the interface region *i.e.* the area $A_I = A_{II}$ in Figure 3.13 therefore

$$[x^{\beta\alpha} - x^{\beta o}]\frac{1}{2}\eta^{\beta} = [x^{\alpha o} - x^{\alpha\beta}]\frac{1}{2}\eta^{\alpha} \tag{3.65}$$

substituting for η from (3.48)

$$[x^{\beta\alpha} - x^{\beta o}]\frac{1}{2}2\sqrt{D_{\beta}t} = [x^{\alpha o} - x^{\alpha\beta}]\frac{1}{2}2\sqrt{D_{\alpha}t} \tag{3.66}$$

where η^{β} is the carburised zone width. Substituting for $x^{\alpha\beta}$ from (3.64)

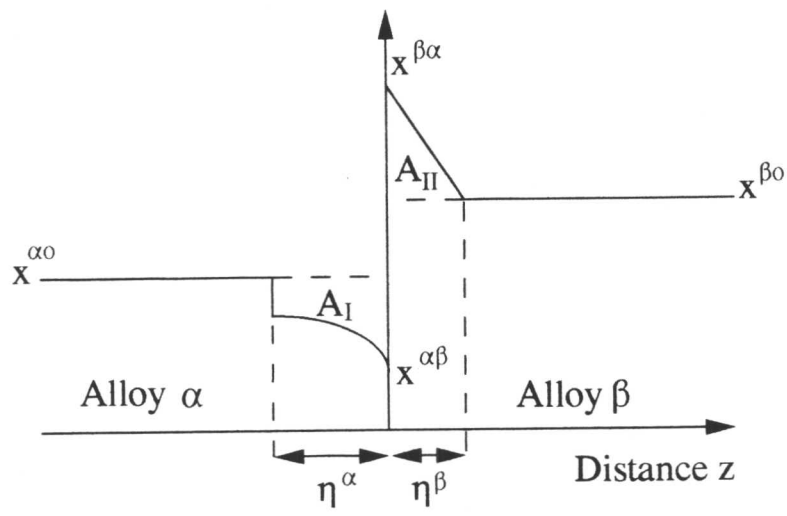

Figure 3.13: Schematic representation of the carbon profiles after Buchmayer *et al.* (1989).

where in the Buchmayer experiments, Δx_2 is the difference in chromium concentration ΔCr.

Rearrangement gives

$$x^{\beta\alpha} = \frac{x^{\alpha o} + \sqrt{\frac{D_\alpha}{D_\beta}} x^{\beta o} + \epsilon_{12} x_1 \Delta x_2}{1 + \sqrt{\frac{D_\alpha}{D_\beta}}} \tag{3.68}$$

which allows the limits to be set.

The limitations of this model are that it is strictly only applicable for temperatures below which chromium carbides are precipitated *i.e.* below 500–550°C, which limits its applicability in terms of the transition joints used in power plant, which are generally operating above this temperature. No account is made for precipitation on the high alloy side of the weld. This is an important factor as precipitation reduces the amount of dissolved carbon, therefore changing the activity of carbon. Precipitation also reduces the chromium concentration in the matrix resulting in a decrease in the driving force for diffusion.

3.4.2 Model due to Christoffel and Curran (1956)

Another more empirical method of producing carbon profiles was proposed by Christoffel and Curran (1956) who describe the process of carbon migration as occurring in four distinct stages to produce a carbon profile as shown in Figure 3.14. In this case there are really three phases present, the low alloy material, the high alloy material and a decarburised band which

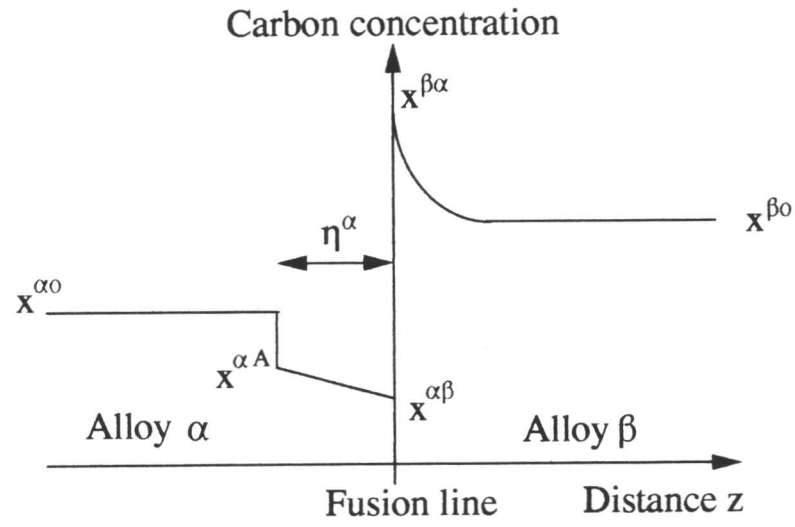

$x^{\beta o}$ = original total carbon content in high alloy material

$x^{\alpha o}$ = original total carbon content in low alloy material

$x^{\alpha A}$ = carbon solubility concentration in low alloy material

$x^{\alpha\beta}$ = carbon content in low alloy material at the fusion line

$x^{\beta\alpha}$ = carbon content in high alloy material at the fusion line

Figure 3.14: Schematic diagram of carbon distribution in composite weldment.

previously, is the activity gradient arising from the difference in substitutional alloy content. As a result, the carbon concentration at the interface increases on the high alloy side of the weld (precipitation may occur if the carbon concentration rises above the solubility limit) causing the development of a carbon concentration gradient and carbon will migrate away from the fusion line under the influence of the gradient. As a further consequence of carbon diffusion across the boundary, the carbon concentration decreases on the low alloy side of the weld and carbon diffuses to the diffusion line under the action of the resulting gradient. When the carbon concentration in the low alloy material has dropped below the solubility limit by virtue of the migration across the fusion line, some of the carbon which is in the form of carbides, breaks up and goes into solution. Therefore, Christoffel and Curran conclude that the solution of carbides accounts for the occurrence of the decarburised band.

where $x^{\alpha A}$ = carbon concentration solubility limit at the diffusing temperature in the low alloy side of the joint and $x^{\alpha o}$ = carbon concentration on the high alloy side of the joint.

This equation is derived as follows:-

Consider the carbon distribution after exposure at an elevated temperature for times t and dt as shown in Figure 3.15. After time t, the width of the decarburised zone is given by η^{α}. From Ficks law:-

$$J = -D\frac{\partial x}{\partial z} \tag{3.70}$$

therefore from Figure 3.15

$$J = -D\frac{(x^{\alpha A} - x^{\alpha \beta})}{\eta^{\alpha}} \tag{3.71}$$

The amount of carbon which has crossed the fusion line into the high alloy side of the weld in time dt is given by:-

$$Jdt = -D\frac{(x^{\alpha A} - x^{\alpha \beta})}{\eta^{\alpha}}dt \tag{3.72}$$

The amount of carbon which has left the low alloy side is also given by Jdt where from Figure 3.15,

$$D\frac{(x^{\alpha A} - x^{\alpha \beta})}{\eta^{\alpha}}dt = (x^{\alpha o} - \frac{x^{\alpha A}}{2} - \frac{x^{\alpha \beta}}{2})d\eta \tag{3.73}$$

$$\eta^{\alpha}d\eta = \frac{D(x^{\alpha A} - x^{\alpha \beta})}{x^{\alpha o} - \frac{x^{\alpha A}}{2} - \frac{x^{\alpha \beta}}{2}}dt \tag{3.74}$$

Integrating this expression,

$$(\eta^{\alpha})^2 = \frac{2D(x^{\alpha A} - x^{\alpha \beta})}{x^{\alpha o} - \frac{x^{\alpha A}}{2} - \frac{x^{\alpha \beta}}{2}}t + A$$

where A is a constant of integration which can be evaluated by applying the boundary conditions that when $\eta^{\alpha} = 0$, $t = 0$, therefore $A = 0$. Also the terms in $x^{\alpha A}$ and $x^{\alpha \beta}$ in the denominator can be neglected as they are very small in ferritic joints, therefore:-

$$(\eta^{\alpha})^2 = \frac{(x^{\alpha A} - x^{\alpha \beta})}{x^{\alpha o}}2Dt \tag{3.75}$$

3.5 Conclusions

Models for predicting carbon diffusion profiles in both austenite and ferrite have been

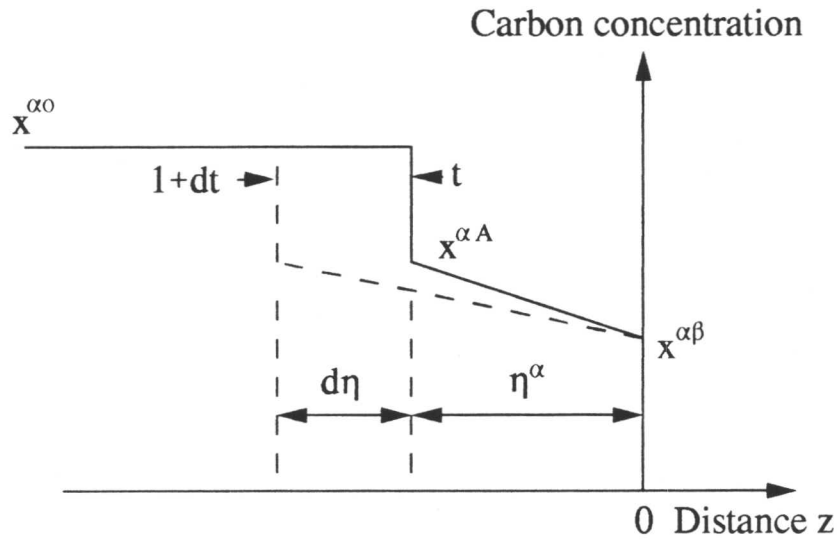

Figure 3.15: Schematic diagram of the development of the decarburised band (Christoffel and Curran, 1956).

Diffusion of carbon in ferrite is complicated by the presence of carbon in the form of carbides. Two models for the diffusion of carbon in ferritic dissimilar metal welds have been described. It should be emphasised at this point that equations 3.49 and 3.75 are both of the form:-

$$\eta^{\alpha} \propto \sqrt{t} \tag{3.76}$$

Therefore both the model of Buchmayer *et al.* and Christoffel and Curran predict that the growth of the decarburised zone will follow parabolic kinetics.

CHAPTER 4

Diffusion in austenite/austenite dissimilar metal joints

4.1 Introduction

The aim of this work was to produce a model for diffusion of carbon across dissimilar metal joints when both sides of the joint are held in the austenite phase field. Previous work, described in Chapter 3, did not provide a means by which the carbon profiles developed during diffusion in the austenite phase field could be predicted. The problem lies in the accurate determination of a value of the partition coefficient, a problem which none of the authors addressed in attempting to describe Darkens diffusion profiles. This chapter describes the attempts that have been made in this research to predict Darkens profiles and to extend this to other alloy systems. It was also intended that this work should provide a basis from which to tackle the problem of diffusion in the ferrite phase field.

To summarise the relevant points from Chapter 3, Stark (1980), Agren (1983) and Bhadeshia (1988) developed equations which can be described by the general formula:-

$$x^{\alpha} = A_1 + B_1 \mathrm{erf}\{\frac{z}{2\sqrt{D_{\alpha}t}}\} \tag{4.1}$$

$$x^{\theta} = A_2 + B_2 \mathrm{erf}\{\frac{|z|}{2\sqrt{D_{\theta}t}}\} \tag{4.2}$$

By applying the boundary conditions of continuity of chemical potential and continuity of carbon flux across the interface, exact solutions could be calculated for these equations:-

$$x^{\alpha} = x^{\alpha\theta} + (x^{\alpha o} - x^{\alpha\theta})\mathrm{erf}\{\frac{z}{2\sqrt{D_{\alpha}t}}\} \tag{4.3}$$

$$x^{\theta} = x^{\theta\alpha} - \sqrt{\frac{D_{\alpha}}{D_{\theta}}}(x^{\alpha o} - x^{\alpha\theta})\mathrm{erf}\{\frac{z}{2\sqrt{D_{\theta}t}}\} \tag{4.4}$$

These equations produce profiles represented schematically in Figure 4.1. To solve these equations values of the diffusion coefficient of carbon in austenite and the partition coefficient are required.

4.2 Calculation of the diffusion coefficient of carbon in austenite

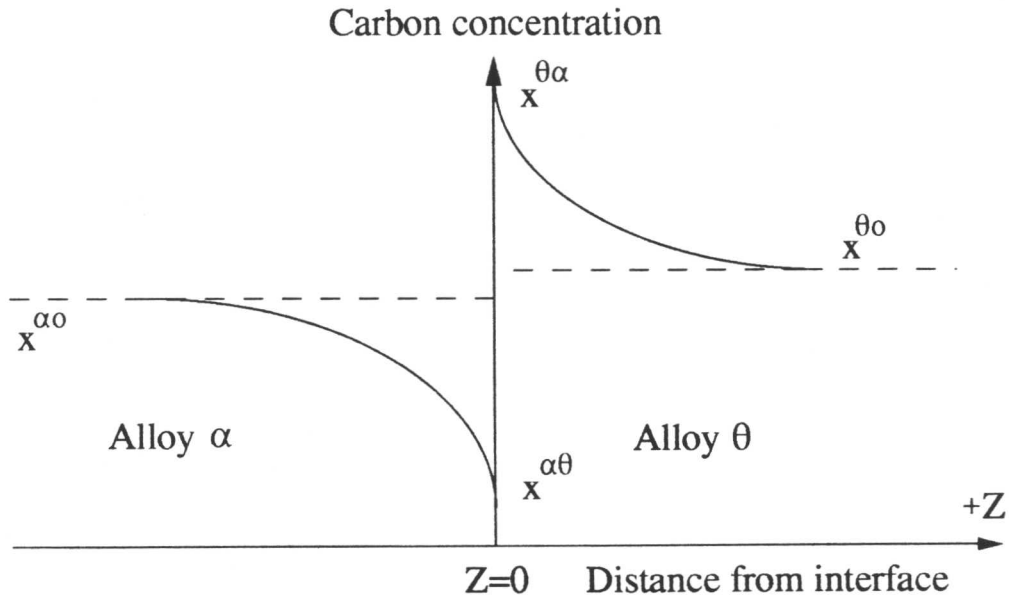

Figure 4.1: Schematic representation of the carbon profiles produced during diffusion across a dissimilar metal weld.

function of position in space. Wells, Batz and Mehl (1950) noted also that the diffusion coefficient increased first slowly then more rapidly with increasing concentration. In fact Hillert (1959) empirically expressed the diffusion coefficient as an exponential function of solute concentration and therefore assumed that the best approximation to the diffusion coefficient could be obtained by considering a constant coefficient corresponding to the maximum solute concentration. However, this assumption is not justified and a more rigorous approach to the concentration dependence of diffusivity is given by Trivedi and Pound (1967) who proposed an integrated average diffusivity, which although only strictly valid for steady state conditions, has been shown to give a reasonable approximation (Bhadeshia, Svensson and Gretoft, 1986) even for conditions where the nature of the concentration profile changes with time.

$$\overline{D} = \int_{x_\gamma^{\gamma\alpha}}^{\overline{x}} \frac{D\{x,\, T\}dc}{(\overline{x} - x_\gamma^{\gamma\alpha})} \tag{4.5}$$

where $\overline{x}$ is the average carbon concentration of the alloy and $x_\gamma^{\gamma\alpha}$ is the maximum permissible carbon content in the austenite at the transformation interface. It is therefore necessary to obtain an expression for $D\{x,T\}$ over the specified carbon concentration range. Siller and McLellan (1969) have developed a model which takes account of the concentration dependence

final equation becomes:-

$$D\{x,T\} = D'\zeta\{\omega\} \tag{4.6}$$

where ω is the atom fraction of carbon which is given by:-

$$\omega = \frac{X}{1-X} \tag{4.7}$$

where X is the atom fraction of carbon atoms. D' is a temperature dependent but carbon concentration independent term described by the equation:-

$$D' = \frac{k_B T}{h}\left[\exp\left(\frac{\Delta F^*}{k_B T}\right)\left(\frac{\lambda^2}{3\gamma_m}\right)\right] \tag{4.8}$$

In this expression:-

ΔF^* = the activation free energy. This term is independent of composition and temperature and represents a difference in the free energy between the 'activated complex' and the 'reactants' when each is in its standard state at the temperature of the reaction.

γ_m = the activity coefficient of the activated complex

λ = the distance between {002} austenite planes

k_B = Boltzmann's constant

h = Planck's constant

The concentration dependent part of equation (4.6) is $\zeta\{\omega\}$. This is defined by Siller and M^{c}Lellan as:-

$$\zeta\{\omega\} = a_c\left[1 + \frac{z_a(1+\omega)}{1-(\frac{z_a}{2}+1)\omega + \frac{z_a}{2}(\frac{z_a}{2}+1)(1-\sigma)\omega^2}\right] + (1+\omega)\frac{\partial a_c}{\partial \omega} \tag{4.9}$$

In this expression, z_a=the co-ordination number of an octahedral site in the austenite lattice, a_c=the activity of carbon and σ is defined as:-

$$\sigma = 1 - \exp\left\{\frac{-\Delta\epsilon}{k_B T}\right\} \tag{4.10}$$

where $\Delta\epsilon$ is the carbon-carbon interaction energy. The calculation of the carbon-carbon interaction energy and the activity of carbon in austenite are given by Bhadeshia (1981(b) and (c)).

Having calculated $\zeta\{\theta\}$ and using experimental values of $D\{x,T\}$, Bhadeshia (1981(a)) deduced that:-

and

$$\ln(\frac{3\gamma_m}{\lambda^2}) = 31.84$$

Thus a value of $\overline{D}$ can be calculated for either side of the weld interface. Therefore, using the notation of Figure 4.1:-

$$\overline{D_\alpha} = \int_{x^{\alpha\theta}}^{x^{\alpha o}} \frac{D\{x, T\}dc}{(x^{\alpha o} - x^{\alpha\theta})} \tag{4.11}$$

$$\overline{D_\theta} = \int_{x^{\theta o}}^{x^{\theta\alpha}} \frac{D\{x, T\}dc}{(x^{\theta\alpha} - x^{\theta o})} \tag{4.12}$$

4.3 Calculation of the partition coefficient

There are basically three methods by which the partition coefficient can be calculated. The relative merits of each of these methods will be discussed later.

4.3.1 Wagner interaction parameters.

For dilute solutions, the activity coefficient for carbon is calculated using Wagner interaction parameters

$$\ln\{\Gamma_c\} = \sum_1^n \epsilon_i x_i \tag{4.13}$$

where ϵ_i is the Wagner interaction coefficient, in austenite, between carbon and carbon for $i = 1$ and carbon and a substitutional alloying element for $i > 1$. Baganis and Kirkaldy (1978) have deduced these as shown in Table 4.1.

The partition coefficient is then given by:-

$$k = \frac{\Gamma_\alpha}{\Gamma_\theta}$$

4.3.2 Uhrenius model.

This is a thermodynamic model developed from that due to Hillert and Staffansson (1970) to describe the Gibbs free energy of carbon in austenite. The basis of this model is the application of the regular solution model to phases which contain one interstital and one substitutional solute element. Thus there are in effect two sublattices, one which is completely filled by the base metal and any substitutional elements and one which is partially filled with the interstitial elements and partially filled with vacancies. The molar ratios are therefore defined by:-

Element	ϵ_i
C	$8910/T$
Mn	-5070/T
Si	4.84-(7370/T)
Ni	-2.2-(7600/T)
Cr	24.4-(38400/T)
Mo	3.855-(17870/T)
Cu	$4200/T$
W	23.4-(36214/T)
V	-24660/T
Nb	-28770/T
Cu	$2800/T$

Table 4.1: Wagner interaction coefficients after Baganis and Kirkaldy, 1978. (where T is the Absolute temperature.)

$$y_c = \frac{a}{b}\frac{x_c}{1-x_c} \tag{4.15}$$

where the subscript m stands for iron and substitutional elements and c stands for carbon in this case. The ratio $(\frac{a}{b})$ (where a represents the number of metal atoms per mole and b the corresponding number of interstitial sites available) is 1 for austenite. This analogy was continued to derive an expression for the integral free energy of austenite *i.e.* the partial free energies summed over all the elements in the phase.

$$RT\ln a_c + \Delta^o G_c^{\gamma \rightarrow gr} = RT\ln\frac{y_c}{1-y_c} + K_1 y_c + K_2 y_m + K_3 y_c y_m + K_4 y_m^2 \tag{4.16}$$

In this expression $\Delta^o G_c^{\gamma \rightarrow gr}$ is the molar Gibbs free energy of pure carbon for the change in crystal structure from $\gamma \rightarrow$ graphite. However, as the couple is comprised of austenite on both sides of the interface then this can be ignored, as can the parameters K_3 and K_4 since these are present in high order terms and will thus have little influence at low values of y_m and y_c. The values K_1 and K_2 have been evaluated from experimental data for carbon activities and optimisation procedures to obtain detailed values of the parameters. These procedures are based on the minimisation of sum of squares between calculated and measured quantities (Uhrenius, 1977). Once these parameters are known then the activity can be calculated from equation (4.16) and thus the activity coefficient is given by equation (4.17):-

$$\Gamma_c = \frac{a_c}{x_c} \tag{4.17}$$

and therefore k can be calculated as before.

4.3.3 Model of Wada et al.

Wada *et al.* (1972) have calculated the activity coefficient for the Fe–Si–C system, for the composition range 0–3wt% Si and 0–1wt%C and give the equation:-

$$\ln\Gamma_c = [\frac{(179 + 8.90\text{wt\%Si})}{T}]\text{wt\%C} + [0.041 + \frac{62.5}{T}]\text{wt\%Si} \tag{4.18}$$

(the compositions in this equation are all in weight percent and T is the Absolute temperature.)

4.4 Extension to the computer program

Once the basic theory had been established from the literature, a program could be written to determine carbon concentration profiles for any weld combination after a specified time at a holding temperature. The flow diagram for the program is illustrated in Figure 4.2 and a full listing given in Appendix II. After the initial values of the two steel compositions and the time and temperature have been input, the diffusion coefficient is calculated. With reference to equation 4.11 and 4.12, it can be seen that values of $x^{\alpha\theta}$ and $x^{\theta\alpha}$ are required. This is estimated using the following approximation:-

$$x^{\alpha\theta} = 0.66x^{\alpha o} \tag{4.19}$$

$$x^{\theta\alpha} = 1.33x^{\theta o} \tag{4.20}$$

This enables an initial estimate of the diffusion coefficient to be made. The partition coefficient is then calculated using one of the four methods described or an experimental value which has to be input. This then enables a better value of the diffusion coefficient to be estimated. This process continues until the best estimate of the diffusion coefficient is obtained. The profiles on either side of the interface can then be calculated for the specified time using equations 4.1 and 4.2.

4.5 Prediction of the Darken profiles

The four methods for the prediction of the partition coefficient can be compared by using test data from the Darken weld A–C. The compositions for this weld are presented in Table 4.2.

The partition coefficients and diffusion coefficients calculated by each method are presented in Table 4.3. If these values are substituted into equations (4.3) and (4.4) then the profiles of Figure 4.3 are obtained.

It can be seen that the values calculated using the method of Wada *et al.* are the most

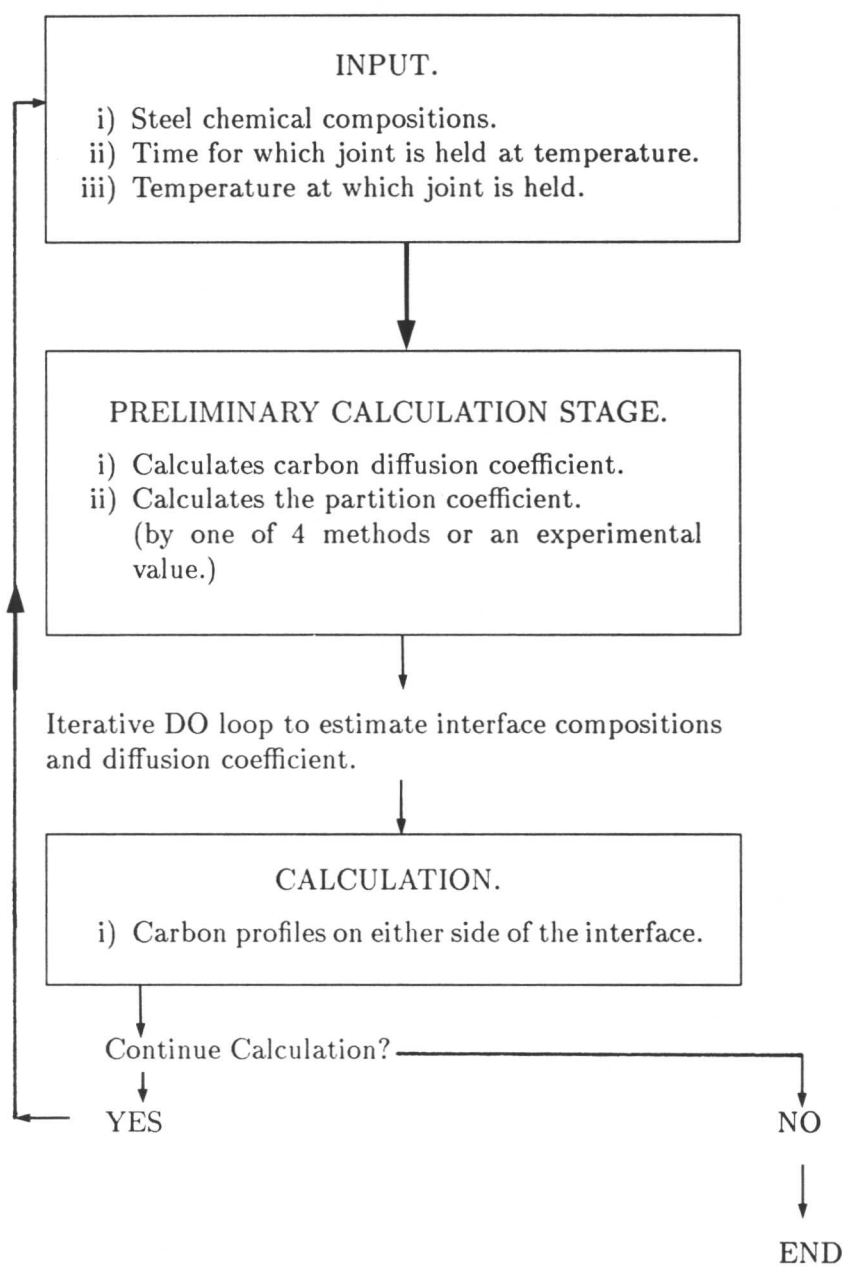

Figure 4.2: Flow diagram representation of the computer program.

mentioned in Chapter 3 that an interesting extension of the work of Kucera and Stransky (1982) was that they obtained values of the interaction coefficients for Si, Cr, Mn and Mo. These results are compared with those of Baganis and Kirkaldy (1978) in Table 4.4. It can be seen that the values are vastly different in the case of silicon which is the substitutional element responsible for diffusion. If the values of Kucera and Stransky are used in Wagners equation (4.13) then the profile in Figure 4.4 is produced.

		C	Mn	Si	P	S	Cr
Steel A	wt%	**0.49**	0.25	**3.80**	0.011	0.006	0.31
Steel B	wt%	**0.04**	0.28	**4.78**	0.006	0.011	–
Steel C	wt%	**0.45**	0.88	**0.05**	0.02	0.008	–

Table 4.2: Composition of the steels used. The carbon and silicon concentrations are highlighted to outline the differences between the steels and the main contributors to the diffusion.

	Wagner	Uhrenius	Wada	Experimental
Partition coefficient	0.968	1.01	1.42	1.86
$D_\alpha/\mathrm{mm^2s^{-1}}$	5.33×10^{-9}	4.76×10^{-9}	4.84×10^{-9}	4.84×10^{-9}
$D_\theta/\mathrm{mm^2s^{-1}}$	5.11×10^{-9}	5.15×10^{-9}	5.60×10^{-9}	5.60×10^{-9}

Table 4.3: Partition and diffusion coefficients calculated for the Darken profile A–C.

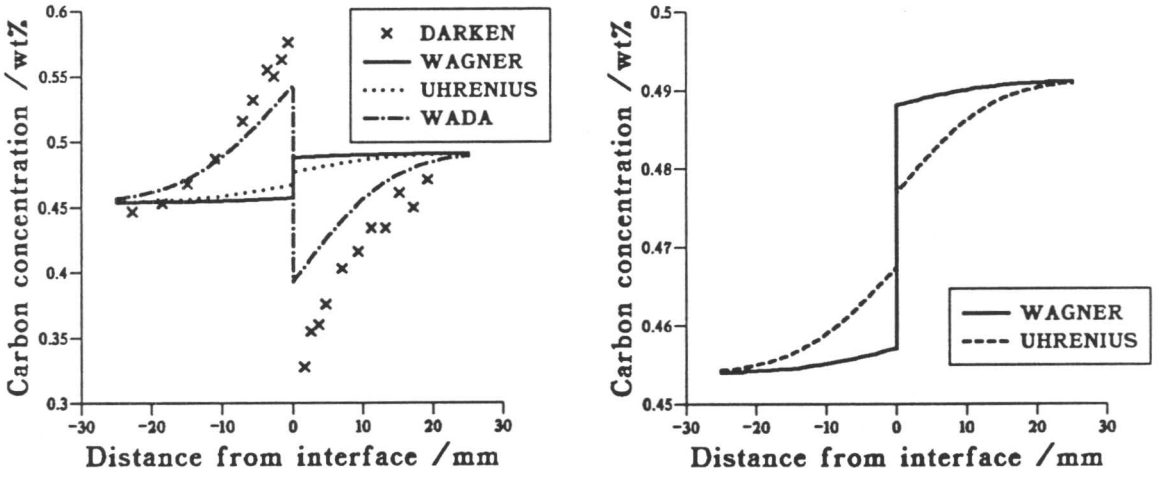

a) b)

Figure 4.3: Calculated Darken profiles using calculated values of the partition coefficient. a) All methods b) Close up showing profiles due to Wagner and Uhrenius. This joint was held at 1050°C for 14 days.

in concentrated solutions. This is proved by the fact that if an experimental value of the partition coefficient is taken from the Darken experimental profiles, then excellent agreement is obtained (Figure 4.5).

The Darken profile A–B can also be predicted using the model of Wada *et al.* These

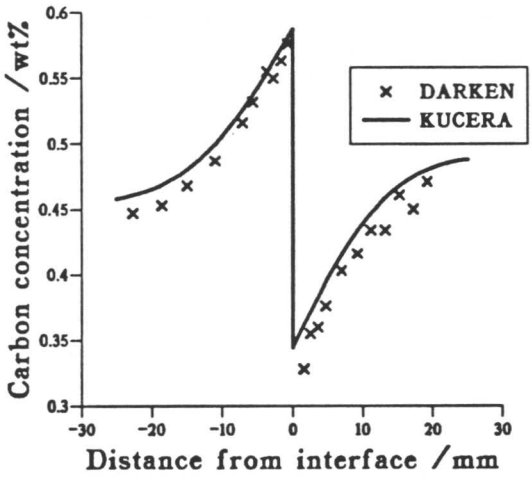

Figure 4.4: Darken profile A–C produced using the interaction coefficients of Kucera and Stransky.

Interaction coefficient	Baganis and Kirkaldy	Kucera and Stransky
ϵ_{Mn}	-3.83	-3.41
ϵ_{Si}	-0.73	7.85
ϵ_{Cr}	-4.62	-9.51
ϵ_{Mo}	-9.65	-9.56

Table 4.4: Comparison of the interaction coefficients calculated at 1323K.

results, together with those using an experimental value of the partition coefficient are shown in Figure 4.6.

The model will also indicate the effect of time and temperature on the diffusion. Figure 4.7(a) shows the effect of increasing time and Fig(4.7(b)) indicates the effect of increasing temperature. For these calculations the compositions of the steels used in the Darken experiment for weld A–C are used.

Having proved the reliability of the equations, the model can be extended with confidence to other more dilute systems, especially those whose thermodynamics are more widely researched. Of special interest are the chromium steels which are of greater commercial importance than those used in the Darken experiment. Wada *et al.* (1972) have also produced an equation for the system Fe–Cr–C for the composition range 0–12 wt% Cr and 0–1 wt% C and give the equation:-

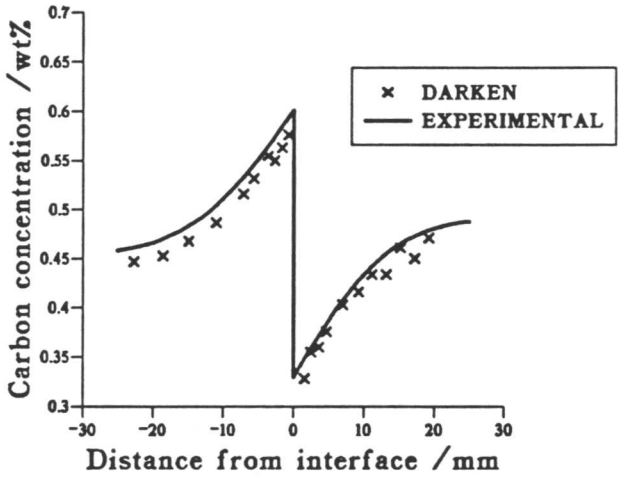

Figure 4.5: Profiles produced using an experimental value of the partition coefficient.

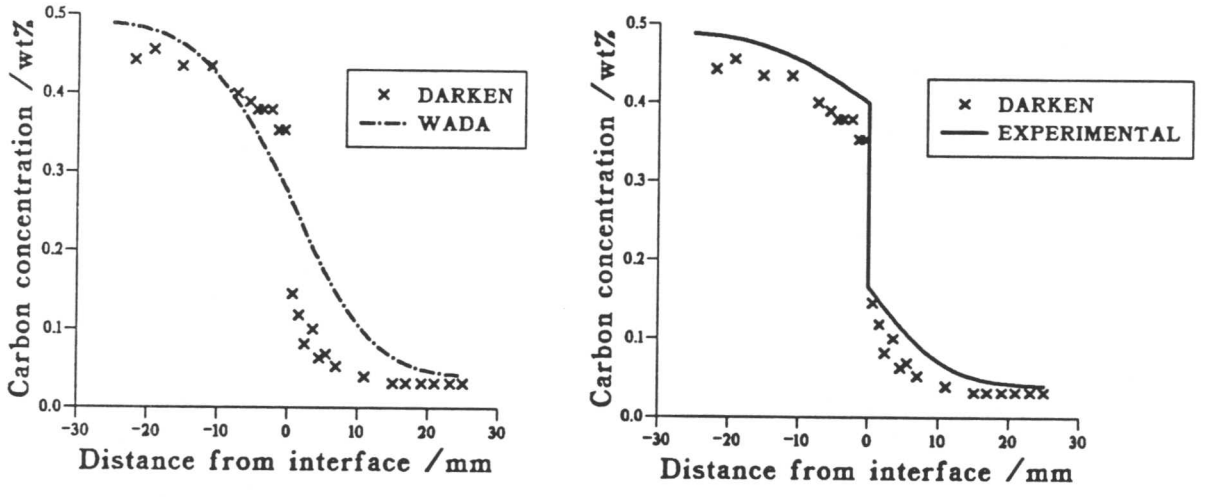

a) b)

Figure 4.6: Darken profile A–B a) using model of Wada *et al.* to calculate the partition coefficient, b) using a partition coefficient taken from the Darken data. This joint was held at 1050°C for 13 days.

$$\ln\Gamma_c = \frac{2300}{T} - 2.24 + \left(\frac{179}{T}\right)\text{wt\%C} - \left(\frac{102}{T} - 0.033\right)\text{wt\%Cr} \tag{4.21}$$

4.6 Extension of the model to the ferrite phase field

This model is only applicable for the joints held in the austenite phase field. Kimmins

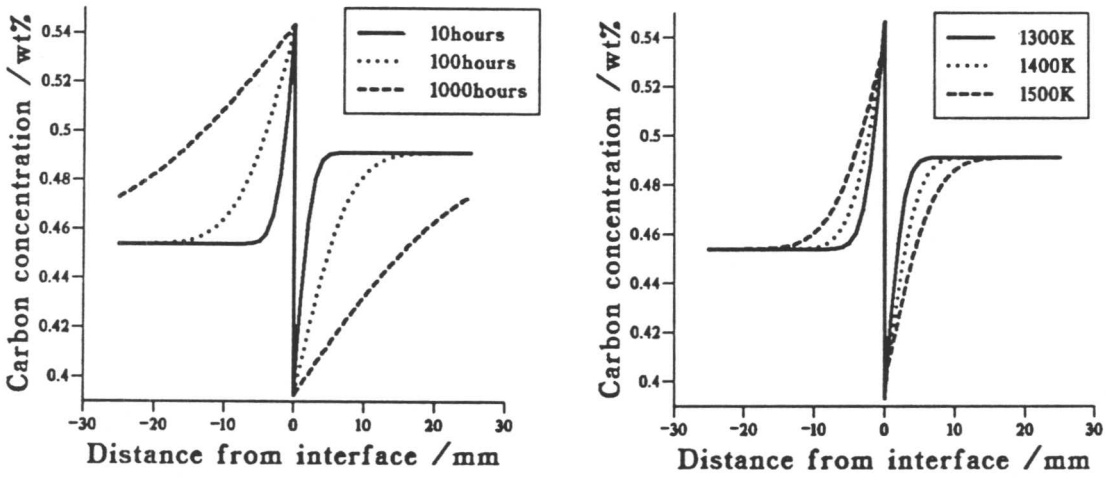

a) b)

Figure 4.7: a) Darken data A–C showing the effect of time. This joint was held at 1323K b) Darken data A–C showing the effect of temperature. This joint was held at each temperature for 16 hours.

(1989) has produced profiles for the $2\frac{1}{4}$CrMo/$\frac{1}{2}$CrMoV dissimilar metal weld which are illustrated in Figure 4.8(a) held at 700°C for 16 hours *i.e.* in the ferrite phase field. If these profiles are modelled using the current equation, it can be seen from Fig 4.8(b) that they are an underestimate. The reason for this discrepancy is that the austenite model deals only with the carbon in solution which is available for diffusion. In ferrite this amount is very small and hence the model cannot account for the steepness of the profiles. Therefore there must be some other process occurring which is accounting for the increase in the amount of carbon available for diffusion. On the low alloy side of the weld this process must be carbon release and on the high alloy side it must be carbon absorbing, such as the dissolution and precipitation of carbides. A detailed investigation into diffusion across dissimilar metal welds in the ferrite phase field is required in order to understand what is going on. Any successful model for predicting the extent of diffusion in ferrite must take these processes into consideration.

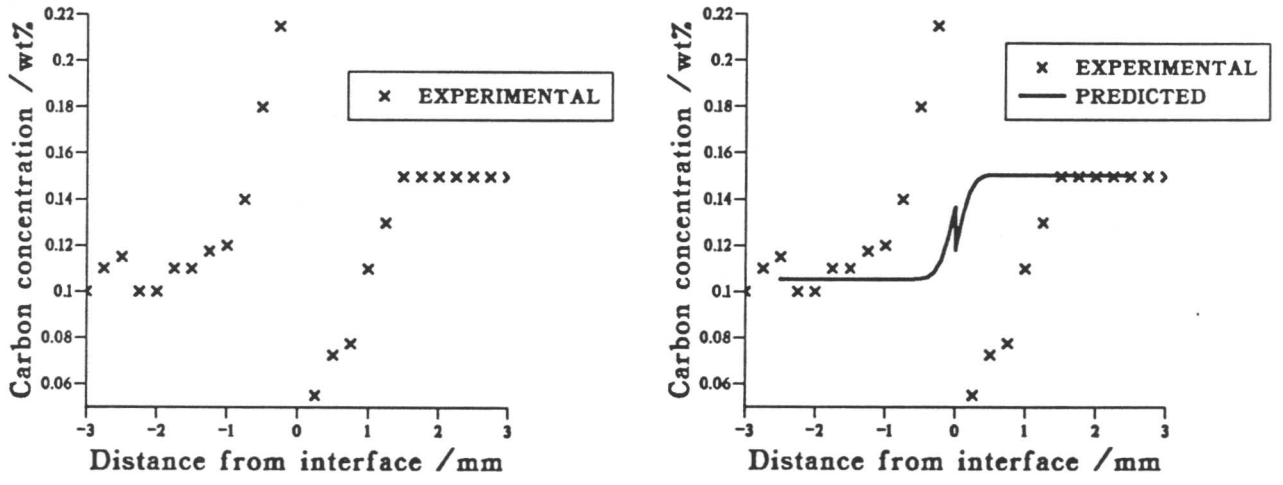

a) b)

Figure 4.8: a) Experimental profile produced by Kimmins (1989). This joint was held at 700°C for 16 hours b) Prediction of this profile using current model.

CHAPTER 5

Experimental procedure

5.1 Weld joint selection

The aim of the experimental work was to study the development of microstructure in dissimilar metal welds after tempering at a series of temperatures. The program of experimental work was intended to simulate the development of carburised and decarburised regions at the weld interface and to provide experimental data for the subsequent modelling of the carburisation and decarburisation effect. For this purpose four experimental joints were chosen; a mild steel/1CrMo, mild steel/$2\frac{1}{4}$CrMo, $2\frac{1}{4}$CrMo/modified 9CrMo and a $2\frac{1}{4}$CrMo/12CrMo joint. The first two joints were selected for the simplicity of the system, *i.e.* if the diffusion of carbon is driven by the difference in chromium concentration across the interface, then the modelling should be facilitated by the fact that one side of the weld, mild steel, contains no chromium. The second two joints were chosen because of their applicability to transition joints in actual power plant.

5.2 Weld preparation and manufacture

The mild steel/1CrMo and mild steel/$2\frac{1}{4}$CrMo joints were made to the weld design shown in Figure 5.1(a), whilst the $2\frac{1}{4}$CrMo/9CrMo and $2\frac{1}{4}$CrMo/12CrMo joints were welded to the design in Figure 5.1(b).

Details of the welding conditions for all of the specimens are given in Table 5.1.

Weld joint	Preheat temperature	Interpass temperature	Number of passes
Mild steel/1CrMo	150–200°C	250°C max	5
Mild steel/$2\frac{1}{4}$CrMo	200–300°C	350°C max	5
$2\frac{1}{4}$CrMo/9CrMo	100°C	100°C	61
$2\frac{1}{4}$CrMo/12CrMo	100°C	100°C	61

Table 5.1: Welding conditions for all of the joints.

The resultant chemical compositions of the weld metal and parent plate for each joint are given in Table 5.2. Post weld heat treatment was not given to any of the joints prior to specimen sectioning.

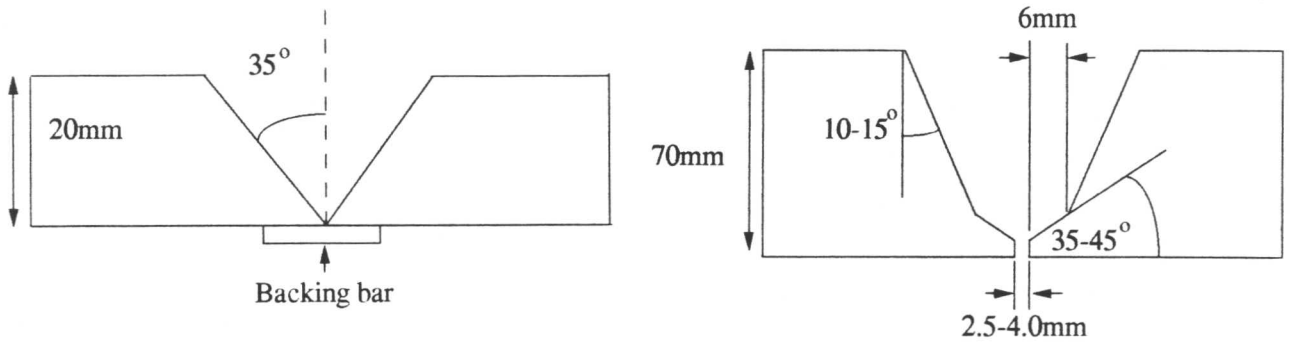

a) b)

Figure 5.1: a) Weld design for the mild steel/1CrMo and mild steel/$2\frac{1}{4}$CrMo joints b) weld design for $2\frac{1}{4}$CrMo/9CrMo and $2\frac{1}{4}$CrMo/12CrMo joints.

Material	Composition /wt%									
	C	Si	Mn	P	S	Cr	Mo	Ni	V	N
Mild steel/1CrMo weld										
Mild steel plate	0.20	0.26	0.76	0.010	0.016	0.035	0.015	0.015	0.000	0.0
1CrMo weld	0.056	0.40	0.77	0.010	0.012	1.11	0.44	0.035	0.015	0.0
Mild steel/$2\frac{1}{4}$CrMo weld										
Mild steel plate	0.23	0.26	0.77	0.011	0.016	0.037	0.015	0.017	0.000	0.0
$2\frac{1}{4}$CrMo weld	0.079	0.43	0.98	0.011	0.012	2.17	0.99	0.053	0.025	0.0
$2\frac{1}{4}$CrMo/9CrMo weld										
9CrMo pipe	0.108	0.44	0.46	0.017	0.001	8.74	0.94	0.19	0.24	0.049
$2\frac{1}{4}$CrMo weld	0.08	0.43	1.01	0.011	0.003	2.42	1.00	0.064	0.028	0.0
$2\frac{1}{4}$CrMo/12CrMo weld										
12CrMo pipe	0.20	0.37	0.58	0.035	0.003	11.5	0.92	0.74	0.31	0.0
$2\frac{1}{4}$CrMo weld	0.08	0.43	1.01	0.011	0.003	2.42	1.00	0.064	0.028	0.0

Table 5.2: Chemical compositions of all of the weld joints.

5.3 Heat treatment program

In order to provide diffusion couples that could easily be studied, the welds were sectioned

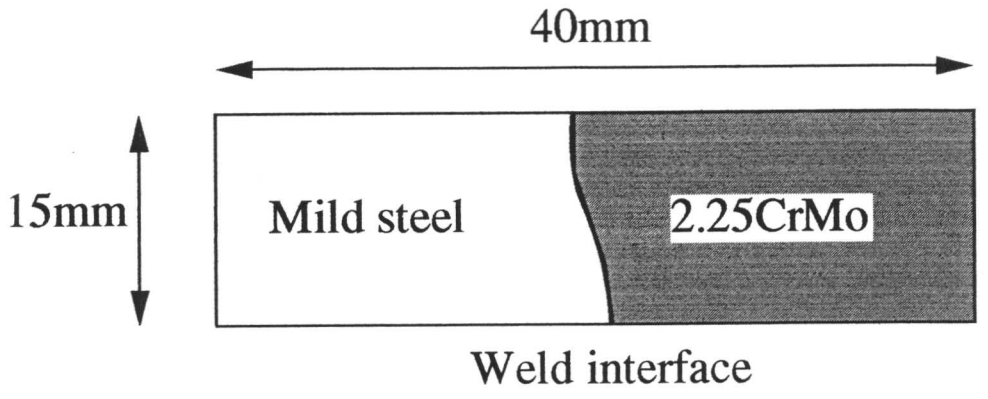

Figure 5.2: Schematic illustration of a dissimilar metal junction as sectioned from welds for diffusion studies.

parallel to the fusion line to the approximate dimensions shown in Figure 5.2.

In order to prevent decarburisation, scaling and contamination during heat treatment, the samples were sealed in quartz tubes under a partial pressure of argon and placed in ceramic boats in the furnace. Three temperatures were chosen at which to carry out the heat treatments. The highest heat treatment temperature was 700°C for mild steel/1CrMo and mild steel/$2\frac{1}{4}$CrMo, 730°C for $2\frac{1}{4}$CrMo/9CrMo and $2\frac{1}{4}$CrMo/12CrMo joints. The lowest corresponded to the working temperature of the power plant (565°C) and an intermediate heat treatment temperature of 620°C was also studied. Heat treatments were carried out at these temperatures for upto 10,000 hours for each weld combination. The specimens were quenched to room temperature in water at the completion of heat treatment.

5.4 Optical microscopy

After heat treatment the specimens were mounted in conductive Bakelite, ground to 120 grit and polished to a 1μm finish. An etch of 2% nital (concentrated nitric acid in methanol) was used for the mild steel/1CrMo and mild steel/$2\frac{1}{4}$CrMo joints. The $2\frac{1}{4}$CrMo/9CrMo and $2\frac{1}{4}$CrMo/12CrMo joints were etched in Villelas reagent (5ml HCl, 1g Picric acid, 100ml methanol). Optical micrographs were taken on Ilford PanF film using an Olympus BHM microscope.

5.5 Hardness measurements.

Vickers hardness measurements were taken at 0.25mm intervals across the weld interface

at right angles to the fusion line from the parent plate to the weld metal. A Leitz Miniload microhardness machine was used with a load of 0.981 N and loading and dwell times of 15 seconds each. At every point three measurements were made and an average taken.

5.6 Measurement of decarburised zone width

There are two methods by which the decarburised zone width can be measured, either from optical micrographs or from hardness profiles taken across the weld interface.

5.6.1 Optical measurement of decarburised zones

Figure 5.3 illustrates how the decarburised zone width can be measured from optical micrographs taken of the weld interface area. The decarburised zone is characterised by the growth of large ferrite grains. The width of these grains was measured at several points on the micrograph and an average taken to give a mean decarburised zone width for that specimen.

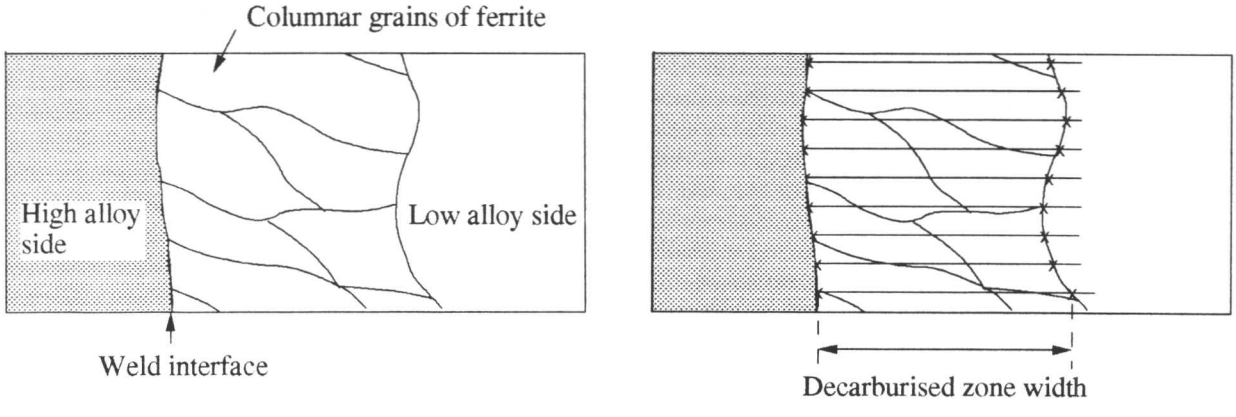

Figure 5.3: Optical measurement of the decarburised zone width.

5.6.2 Hardness profile measurement of decarburised zone width

The principle behind this method is that the carburisation and decarburisation, which has taken place during the heat treatment of the joint, will produce hard and soft zones immediately adjacent to each other at the weld interface. Therefore, if a hardness profile is taken across the interface region at right angles to the fusion line, then a profile as illustrated in Figure 5.4 would be expected. It is therefore possible to measure a decarburised zone width from these plots. However, it was found that, in practice, there was so much scatter in the results that often it

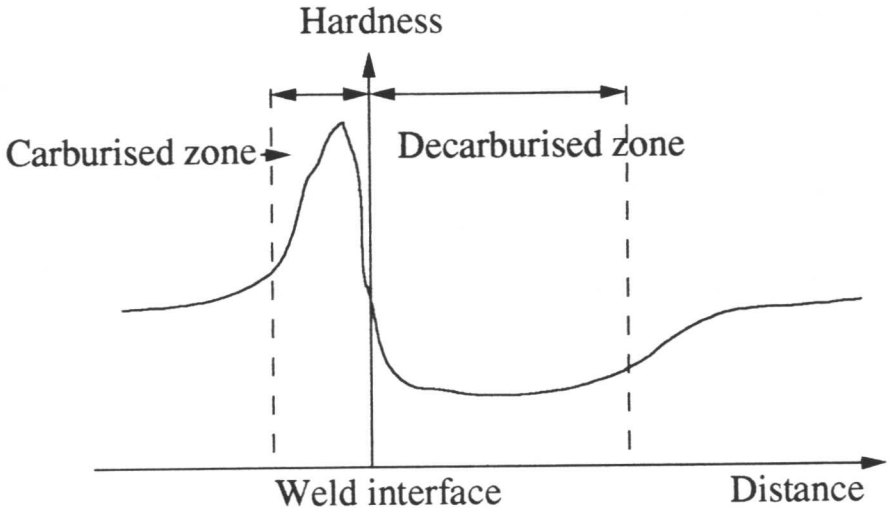

Figure 5.4: Example hardness plot across the dissimilar weld interface.

was difficult to distinguish clearly the carburised and decarburised regions. For this reason the decarburised zone width data presented has all been measured optically.

5.7 Scanning electron microscopy (SEM)

Imaging in the SEM was carried out in a Camscan S4 microscope operated at 30kV using secondary electrons and 45° tilt. The specimens were polished and deeply etched to reveal the carbide structure which then protruded above the matrix. Chemical analyses were taken at 0.25mm intervals across the weld interface at right angles to the fusion line. A live time of 100 seconds was used with an average count rate of 1000 counts per second and a dead time of less than 20%. The operating voltage was 20kV. The working distance was kept at 30mm and the specimen tilted at an angle of 45° to the detector. The data were analysed using the LINK ZAF4 programmes for microanalysis, which correct the data for atomic number and account for overlapping peaks by fitting standard profiles.

5.8 Transmission electron microscopy (TEM)

Transmission electron microscopy (TEM) was used to identify individual carbides in the region of the weld close to the fusion line. The carbide phases can, of course, in most cases, be identified uniquely using electron diffraction, but this is in practice very difficult when examining large numbers of small particles. The carbides are often too thick or too thin to get reasonable diffraction data, and in some cases, the diffraction patterns can be ambiguous.

A common alternative method used routinely in this kind of research is based on energy dispersive X-ray (EDX) microanalysis. This technique for carbide identification is carried out

in the TEM and it enables chemical analyses to be taken from individual carbides. For these procedures, carbon extraction replicas were used instead of thin foils in order to avoid spurious X-rays from the matrix.

The carbon replica extraction procedure developed by Smith and Nutting (1957) was used to produce thin carbon films suitable for examination in the TEM. The metal surface was first polished and etched so that the structure was clearly visible under the optical microscope. A thin carbon film was then evaporated onto the metal surface. The thin film was removed by etching in a solution of 5% chloral (hydrochloric acid in methanol) at a potential of 1.5V until the film began to lift away from the surface. The specimen was then washed in alcohol before being transferred to a bath of distilled water where the replica was floated off and carefully collected on copper grids. The replicas were examined in the TEM using an accelerating voltage of 120kV. The diffraction patterns were taken using selected area apertures and chemical compositions were determined using EDX analysis with a specimen tilt of 35° towards the X-ray detector. A live time of 100 seconds was used during which the dead time was not allowed to exceed 25%. The data were analysed using the LINK RTS2 FLS programmes for microanalysis.

In this research, the majority of the carbide identification was carried out using EDX analysis with diffraction patterns providing valuable identity verification data.

CHAPTER 6

Experimental results

6.1 Introduction

The experimental work described here was all conducted on joints in the ferrite phase field to try and gain some understanding into the processes governing the diffusion of carbon. The work described in Chapter 3 highlighted the fact that the mechanism by which carbon is released for diffusion from the low alloy side and the mechanism by which it is taken up on the high alloy side needs to be understood thoroughly in order to develop a predictive model. The purpose of this work was to make an extensive characterisation of the microstructure and in particular the development of any decarburised zone in four different joints heat treated for varying times at three different temperatures. All welds were received in the as–welded condition with no post weld heat treatment having been given to any of the weld combinations. The micrographs in Figure 6.1 indicate the initial microstructure of all of the welds studied. The mild steel plate in both Figure 6.1(a) and 6.1(b) has a ferrite/pearlite structure in the unaffected parent and a martensitic reheated heat affected zone (HAZ) microstructure. The weld bead microstructure of both the 1CrMo and $2\frac{1}{4}$CrMo is fully bainitic. The 9CrMo and 12CrMo parent plate illustrated in Figure 6.1(c) and 6.1(d) is martensitic. These micrographs also illustrate the bainitic nature of the $2\frac{1}{4}$CrMo weld metal in both joints.

6.2 Measurement of the decarburised zone width

As described previously, there are two methods by which the decarburised zone width can be measured, optical measurement and hardness profile measurement.

6.2.1 Optical measurement of the decarburised zone width

Example micrographs for the four joints are presented in Figure 6.2. These joints were all heat treated at the post weld heat treatment temperature of the welds for 64 hours. The decarburised zone width is taken to be the distance from the fusion line to the end of the large ferrite grains.

6.2.1.1 Effect of time

The decarburised zone width plots against root time for all of the joints at their respective heat treatment temperatures are given in Figure 6.3. As would be expected all of these plots show that there is an increase in the amount of decarburisation with time. This point is also

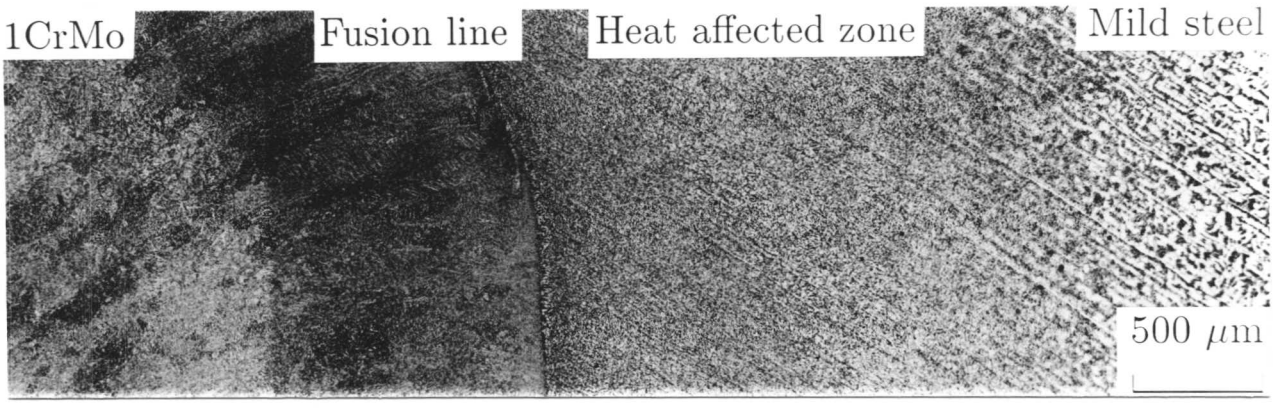

a) mild steel/1CrMo

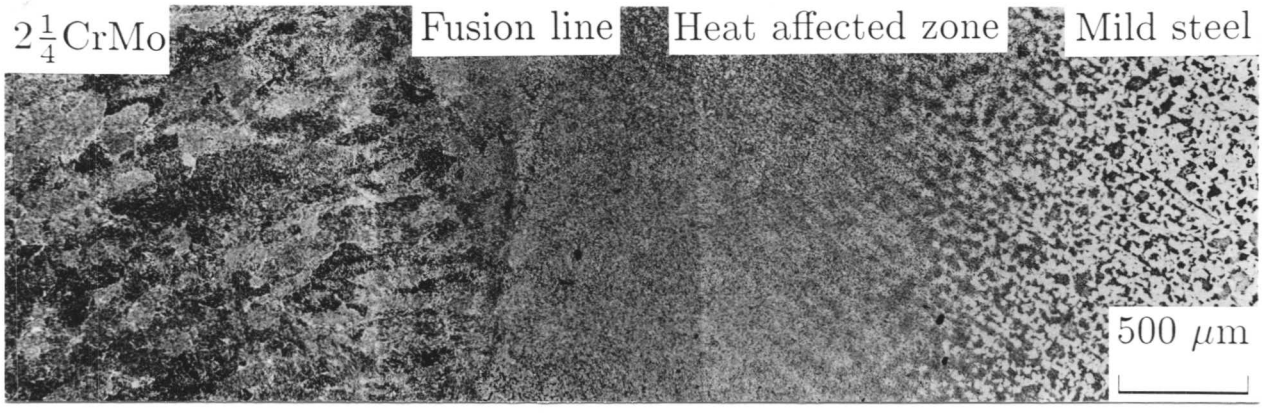

b) mild steel/$2\frac{1}{4}$CrMo

Figure 6.1: As–received microstructures

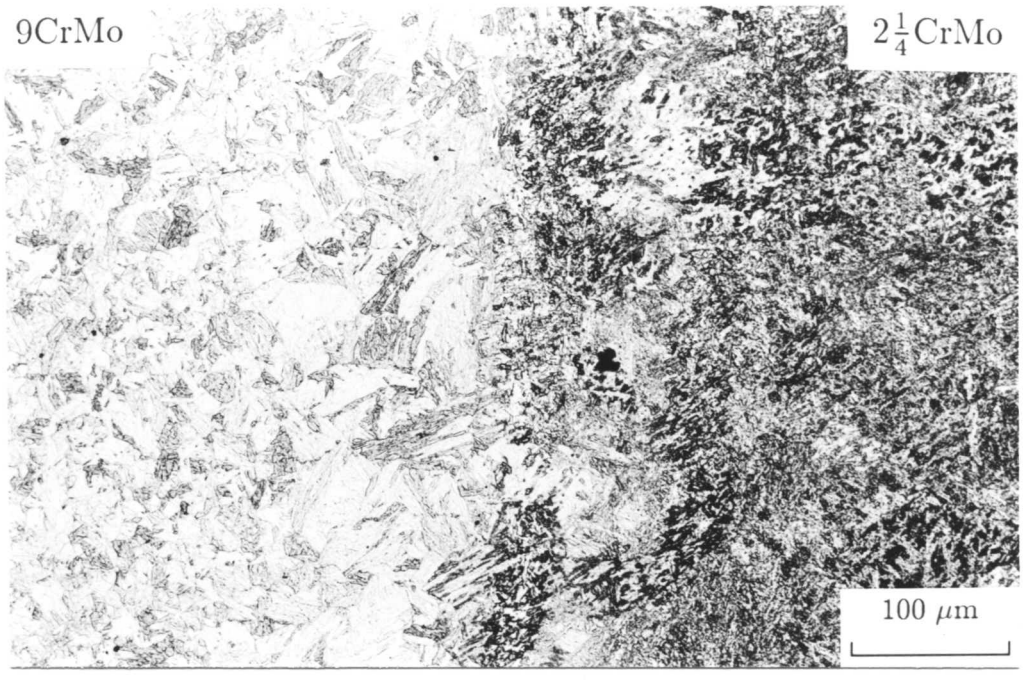

c) $2\frac{1}{4}$CrMo/9CrMo

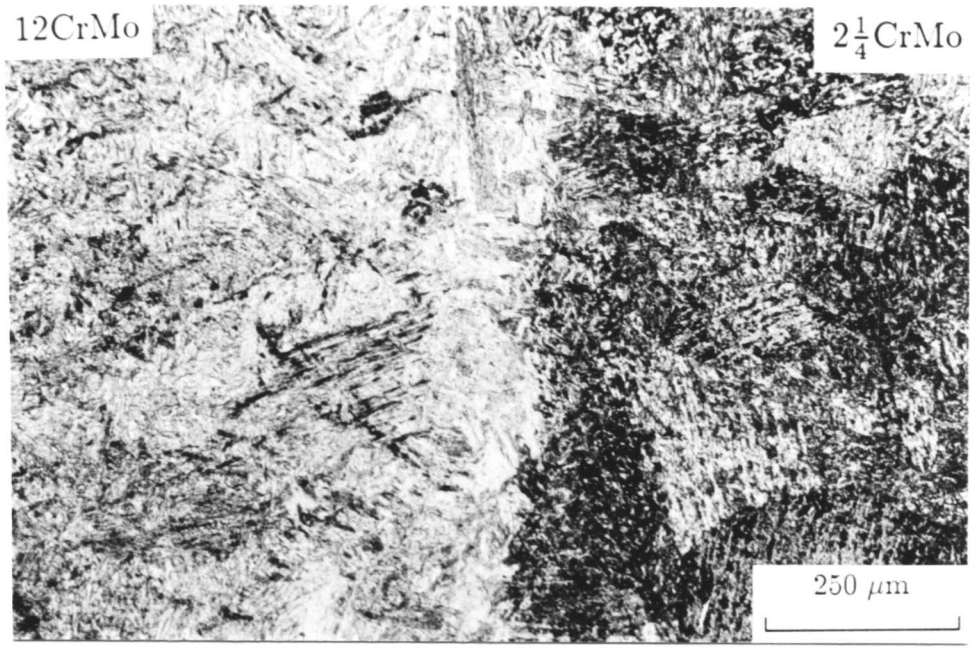

d) $2\frac{1}{4}$CrMo/12CrMo

Figure 6.1: As–received microstructures

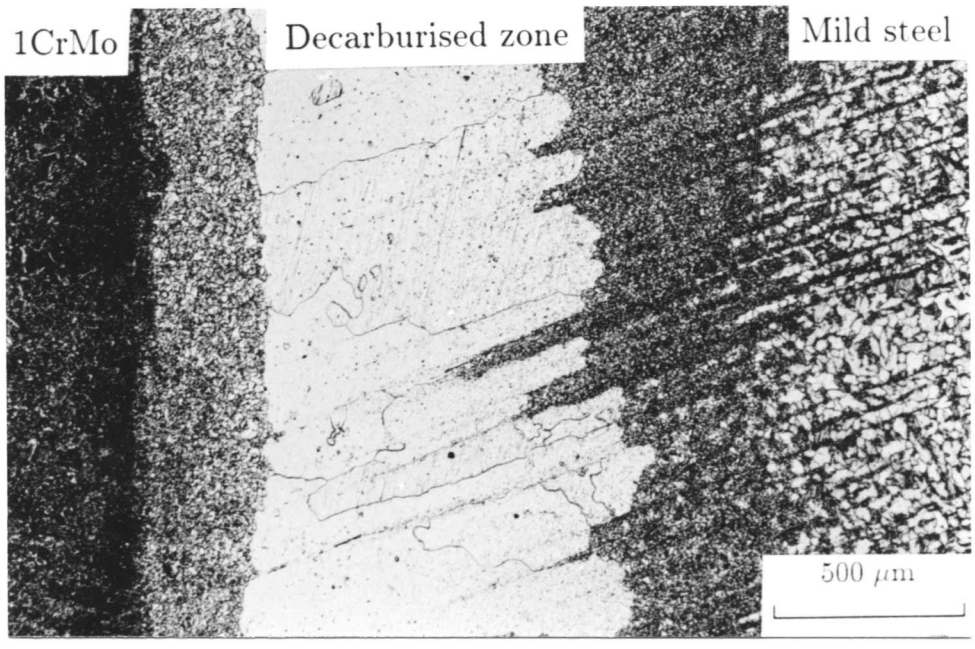

a) mild steel/1CrMo - 64 hours at 700°C

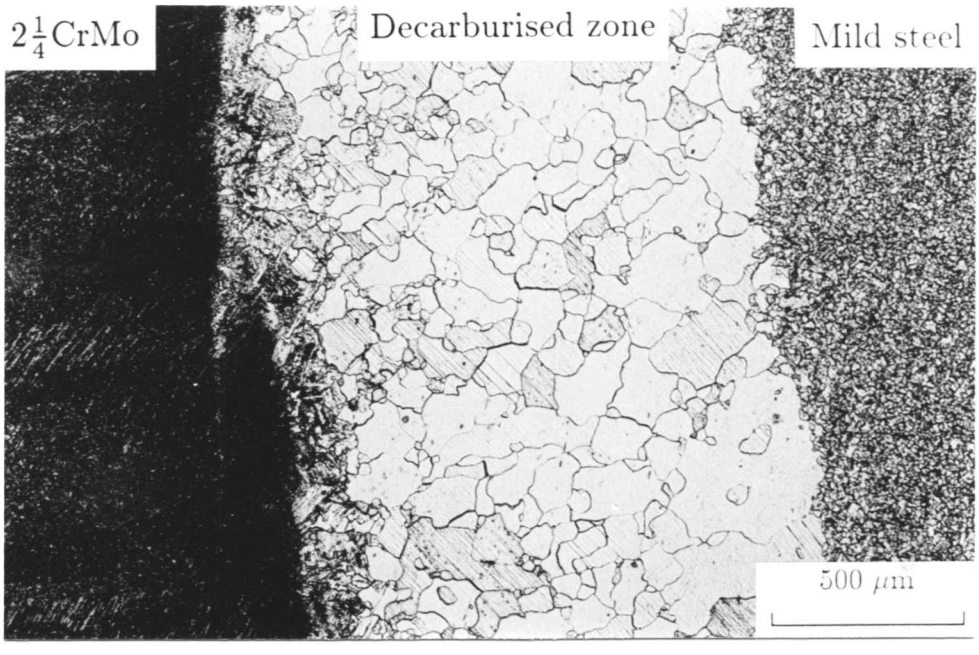

b) mild steel/$2\frac{1}{4}$CrMo - 64 hours at 700°C

Figure 6.2: Optical micrographs from specimens heat treated at the post weld heat treatment temperature for 64 hours

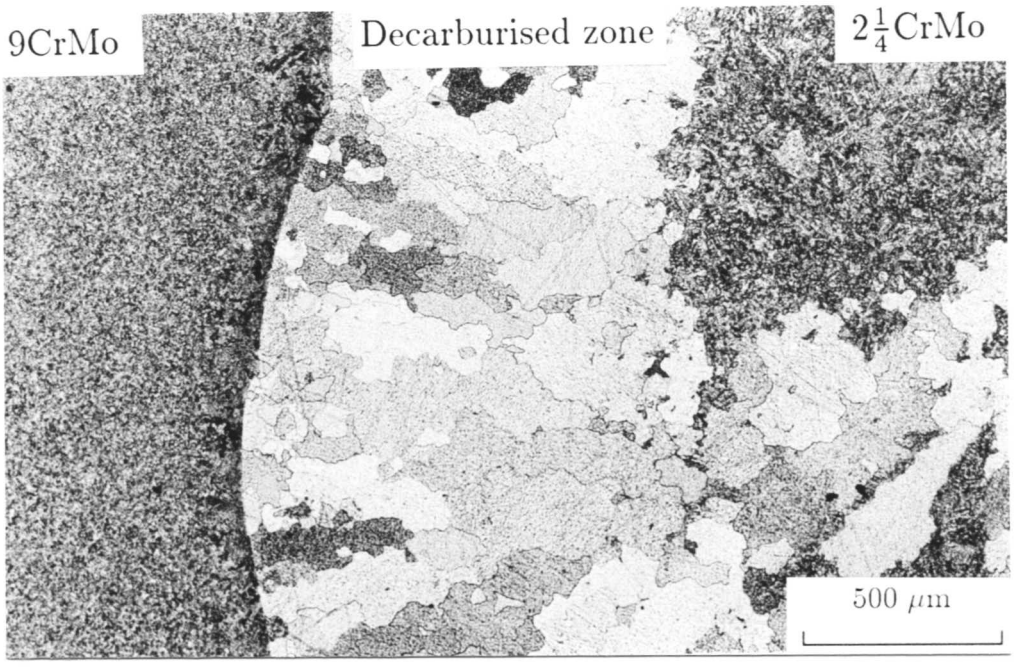

c) $2\frac{1}{4}$CrMo/9CrMo - 64 hours at 730°C

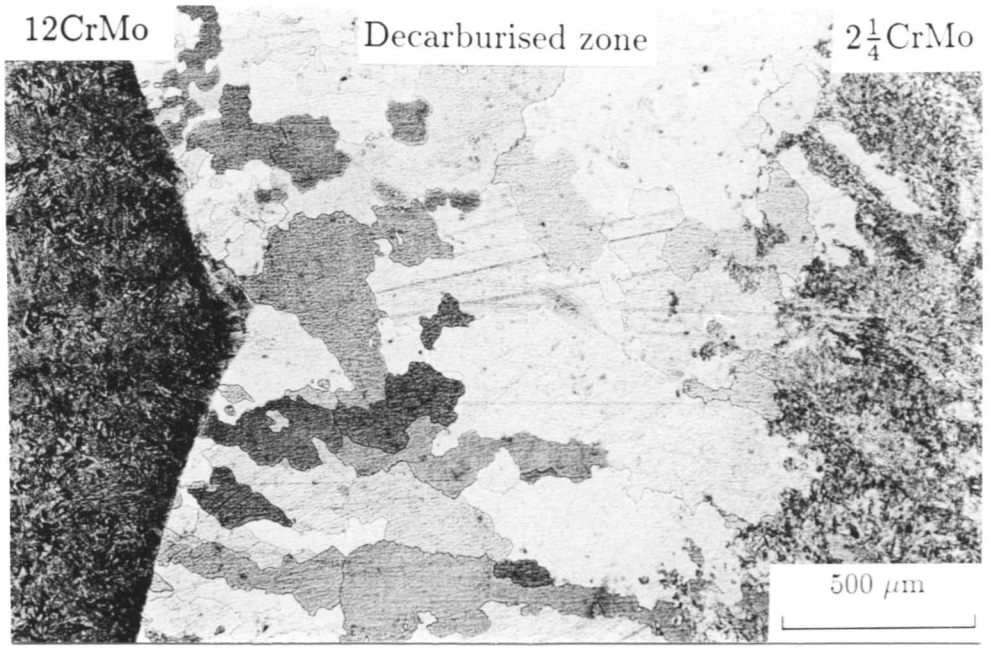

d) $2\frac{1}{4}$CrMo/12CrMo - 64 hours at 730°C

Figure 6.2: Optical micrographs from specimens heat treated at the post weld heat treatment temperature for 64 hours

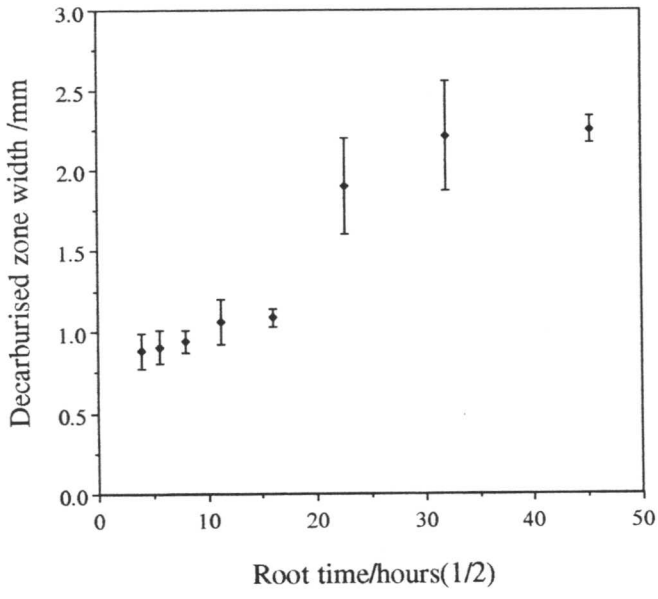

a) mild steel/1CrMo - 700°C

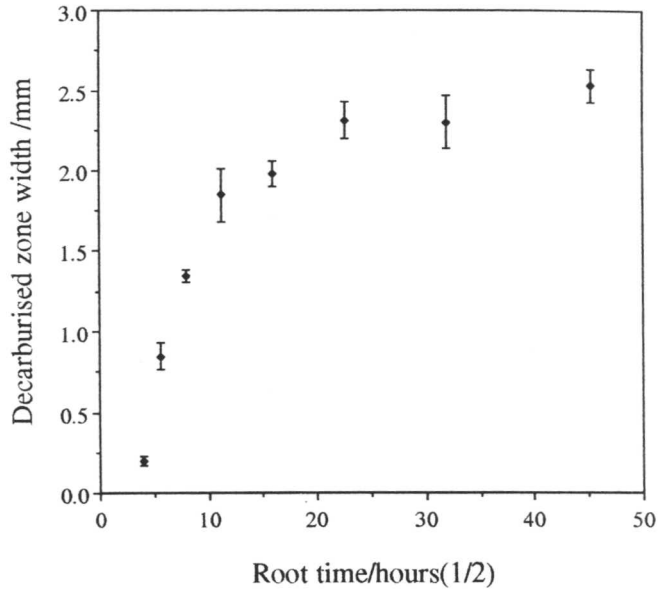

b) mild steel/$2\frac{1}{4}$CrMo - 700°C

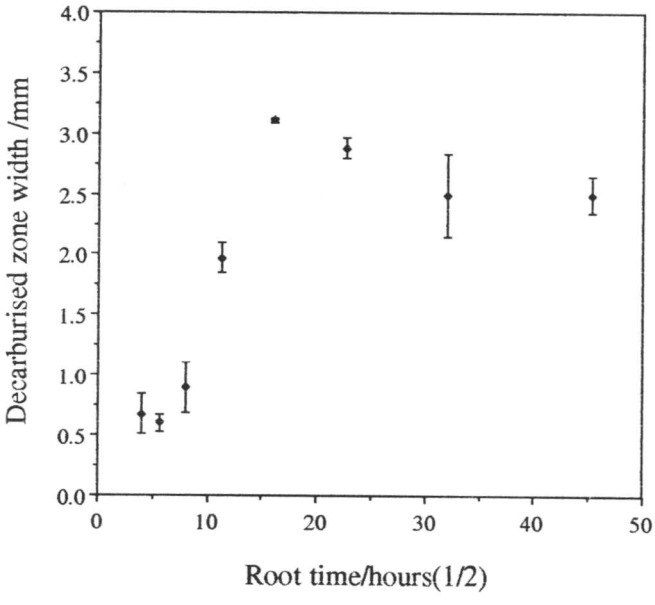

c) $2\frac{1}{4}$CrMo/9CrMo - 730°C

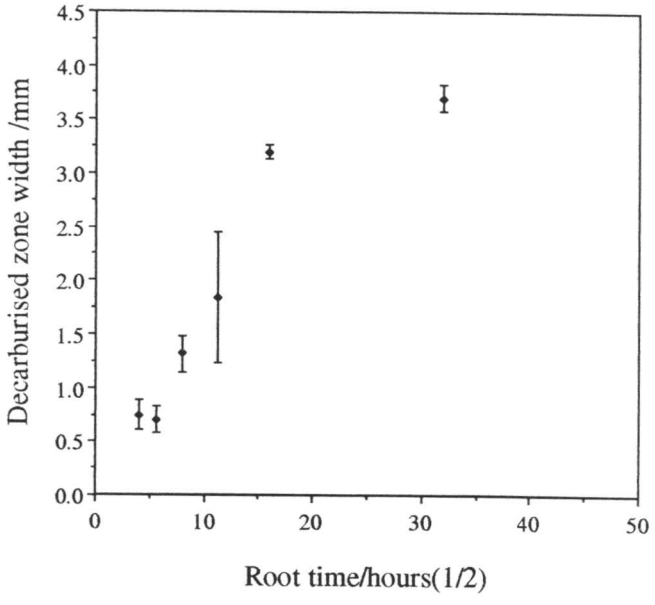

d) $2\frac{1}{4}$CrMo/12CrMo - 730°C

Figure 6.3: Decarburised zone width plots for the four joints heat treated at the post weld heat treatment temperature for the joints

illustrated in the micrographs of Figure 6.4. However, parabolic growth rate theory as described in Chapter 3 would predict that:-

$$\eta^{\alpha} \propto \sqrt{t}$$

where η^{α} is the decarburised zone width. Therefore plots such as these should be linear. These plots therefore indicate that the classical parabolic equations do not apply in this case as there is clearly a levelling off of the profiles at longer times.

6.2.1.2 Effect of temperature

The effect of temperature is illustrated in the micrographs of Figure 6.5 and the plot of Figure 6.6. Figure 6.5a indicates that although changes in the microstructure are occurring in the joint at 565°C, no decarburised zone width could be measured optically at this temperature. These indicate that the extent of diffusion is less at lower temperatures. This is what would be expected as diffusion is a thermally activated process (section 7.3).

6.2.1.3 Effect of alloy content

A comparison of the relative extent of decarburisation between joints is quite difficult due to the error in the experimental measurements. Plots for all of the joints at the two temperatures where decarburised zone widths could be measured are given in Figure 6.7. At the post weld heat treatment temperature, the following sequence is suggested:-

$2\frac{1}{4}$CrMo/12CrMo > ($2\frac{1}{4}$CrMo/9CrMo & mild steel/$2\frac{1}{4}$CrMo) > mild steel/1CrMo

It is not really possible to distinguish between the $2\frac{1}{4}$CrMo/9CrMo joint and the mild steel/$2\frac{1}{4}$CrMo joint as the curves overlap within the experimental error at several points. At 620°C:-

(mild steel/$2\frac{1}{4}$CrMo and mild steel/1CrMo) > ($2\frac{1}{4}$CrMo/9CrMo and $2\frac{1}{4}$CrMo/12CrMo)

(for the 620°C comparison the two steels have been grouped together as it is not possible to say which have the greater decarburised zone widths within the experimental error.)

The first sequence is probably as would be expected given that the sequence is showing a decrease in the difference in alloy content between both sides of the weld and temperature from left to right. However, the sequence at 620°C shows that less decarburisation occurs in the two alloy systems that have the greater difference in chromium concentration across the interface, $2\frac{1}{4}$CrMo/9CrMo and $2\frac{1}{4}$CrMo/12CrMo.

6.2.1.4 Problems in optical measurement of the decarburised zone width

The major problem with the optical measurement is determining where the decarburised zone width finishes. This is more difficult in the two cases where the decarburisation is in

the weld metal as the large ferrite grains tend to follow the weld bead shape as illustrated in Figure 6.8. In these cases an estimate had to be made.

6.3 Hardness measurements of the decarburised zone width

Hardness profiles for the mild steel/$2\frac{1}{4}$CrMo joint are are presented in Figure 6.9. These illustrate the unaged profile together with three taken at increasing times at 700°C. The error bars on this plot indicate the standard deviation from the mean value of the three readings taken at each point. The decarburised zone widths measured using this technique are compared with those measured optically in Table 6.1. It can be seen that this method is highly inaccurate owing to the scatter produced in the microhardness data and the fact that this is only a scan across a small area and it is not representative of the whole sample. The variation of the decarburised zone width in the weld metal as described in the previous section is also a problem. For these reasons the decarburised zone width measurements were entirely made using the optical technique.

	Decarburised zone width /mm	
Time /hours	Hardness measurement	Optical measurement
32	0.5	0.85
128	0.72	1.85
256	0.75	1.95
512	1.75	2.31
1024	1.75	2.30

Table 6.1: Comparison of decarburised zone widths measured using the hardness and optical techniques for the mild steel/$2\frac{1}{4}$CrMo joint at 700°C.

6.4 Measurement of the carburised zone width

The carburised zone width *i.e.* the region on the high alloy side of the weld interface where the carbon content is greater than average is rather more difficult to measure optically, as the micrographs illustrate. For this reason this measurement is made using the hardness profiles. Hardness profiles in the carburised region are given in Figure 6.10. Although this method suffers from the same problems of inaccuracy as described for the decarburised zone width, it does give an indication of the extent of carburisation compared with decarburisation for the same sample

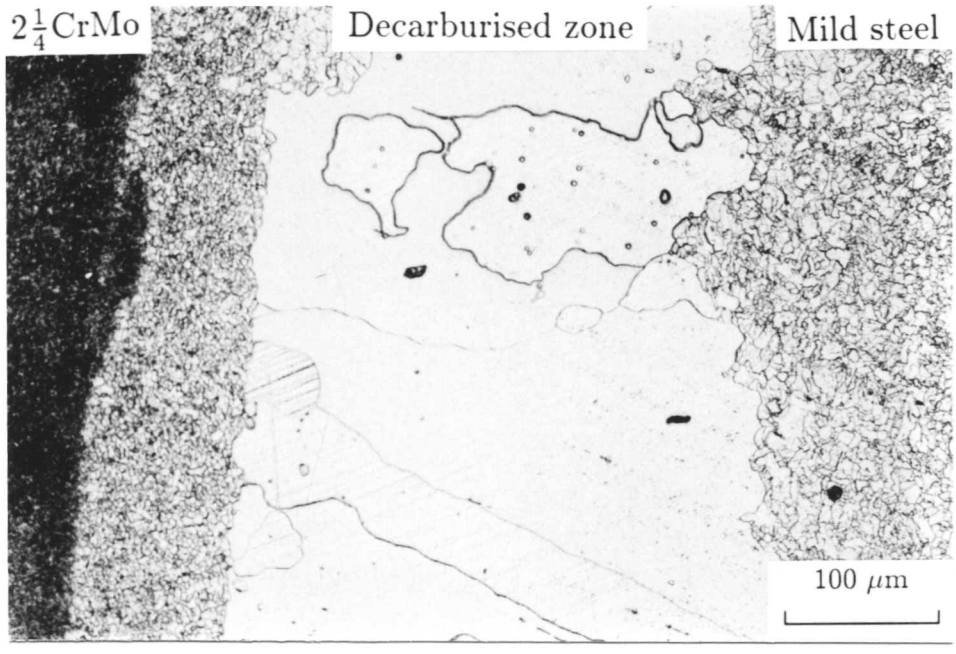

a) mild steel/$2\frac{1}{4}$CrMo - 32 hours at 700°C

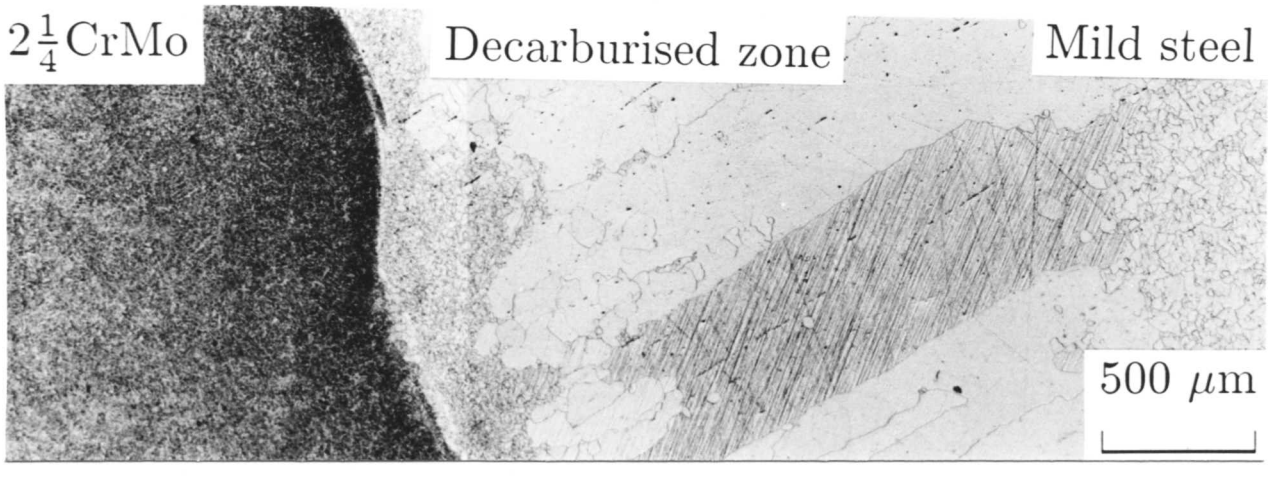

b) mild steel/$2\frac{1}{4}$CrMo - 512 hours at 700°C

Figure 6.4: Optical micrographs for mild steel/$2\frac{1}{4}$CrMo specimens heat treated at 700°C for various times

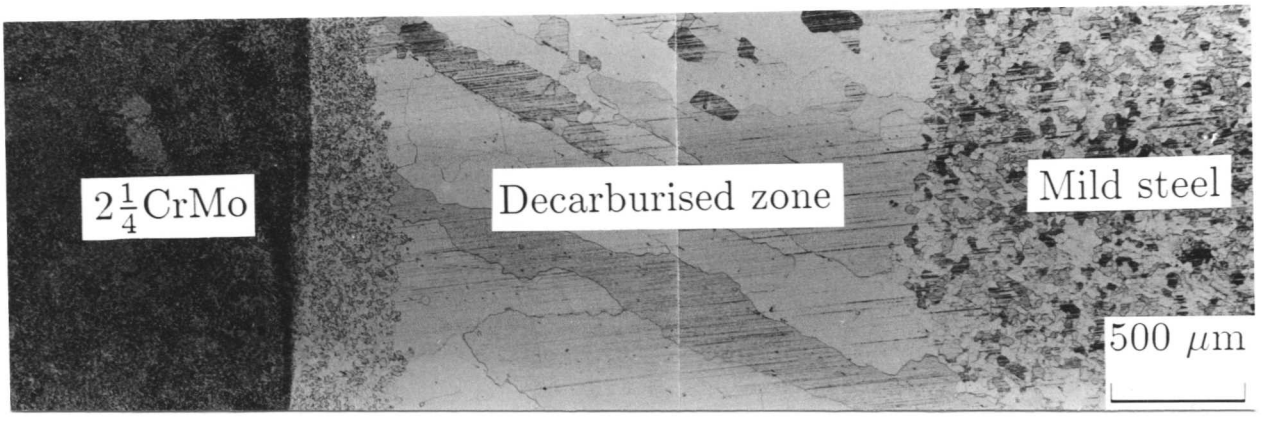

c) mild steel/$2\frac{1}{4}$CrMo - 2000 hours at 700°C

Figure 6.4: Optical micrographs for mild steel/$2\frac{1}{4}$CrMo specimens heat treated at 700°C for various times

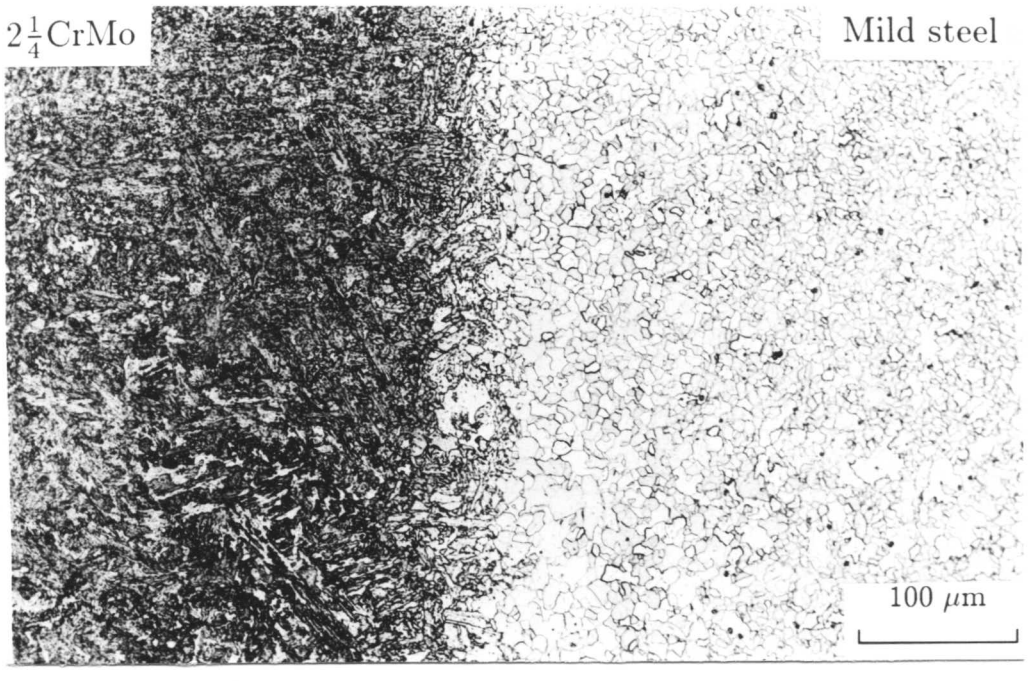

a) mild steel/$2\frac{1}{4}$CrMo - 512 hours at 565°C

Figure 6.5: Optical micrographs for mild steel/$2\frac{1}{4}$CrMo specimens heat treated at various temperatures for 512 hours

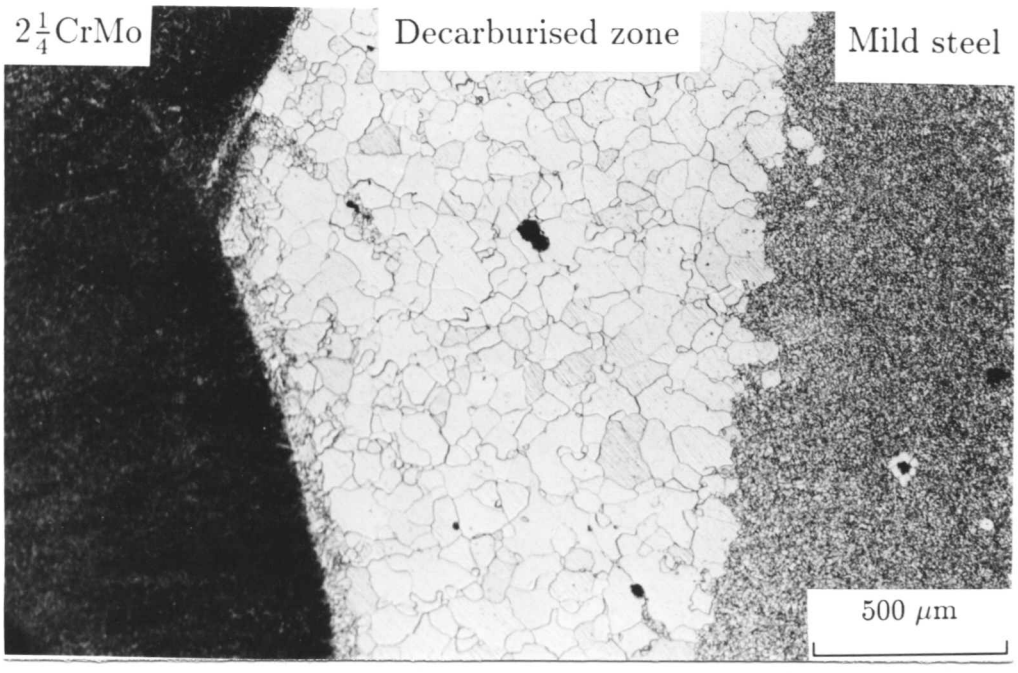

b) mild steel/$2\frac{1}{4}$CrMo - 512 hours at 620°C

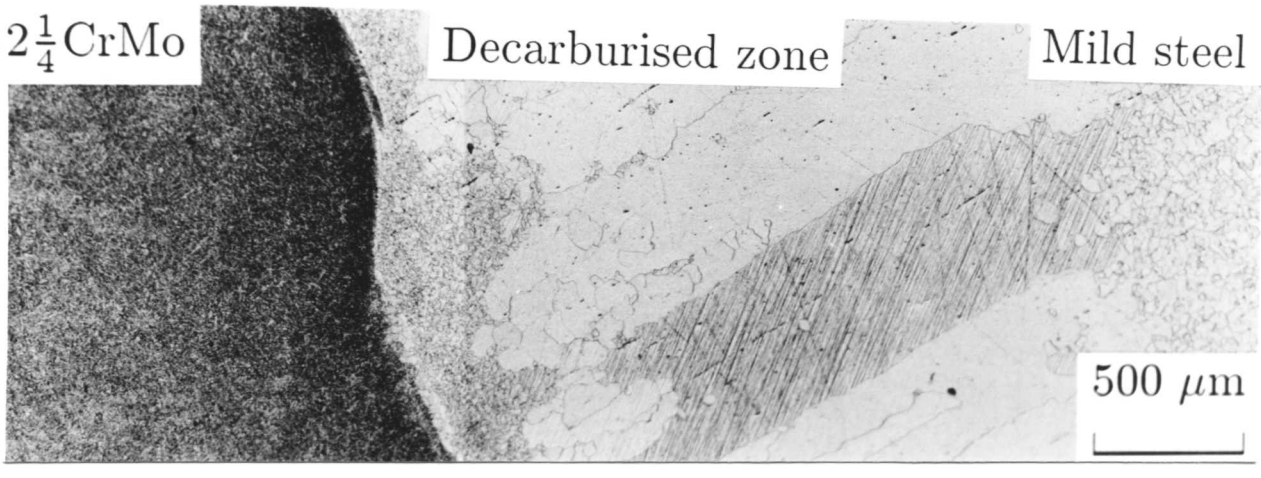

c) mild steel/$2\frac{1}{4}$CrMo - 512 hours at 700°C

Figure 6.5: Optical micrographs for mild steel/$2\frac{1}{4}$CrMo specimens heat treated at various temperatures for 512 hours

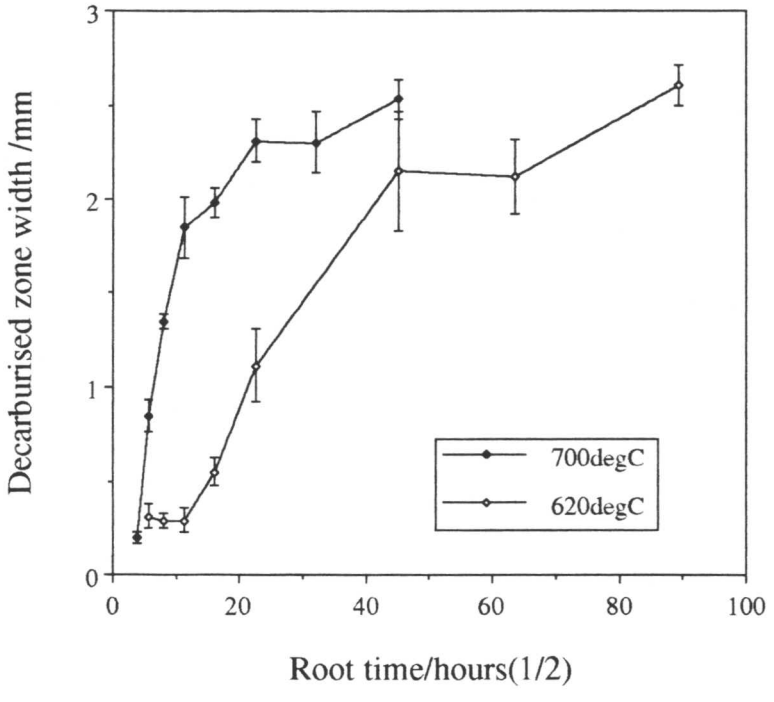

Figure 6.6: Effect of temperature on the decarburised zone width for the mild steel/$2\frac{1}{4}$CrMo joint

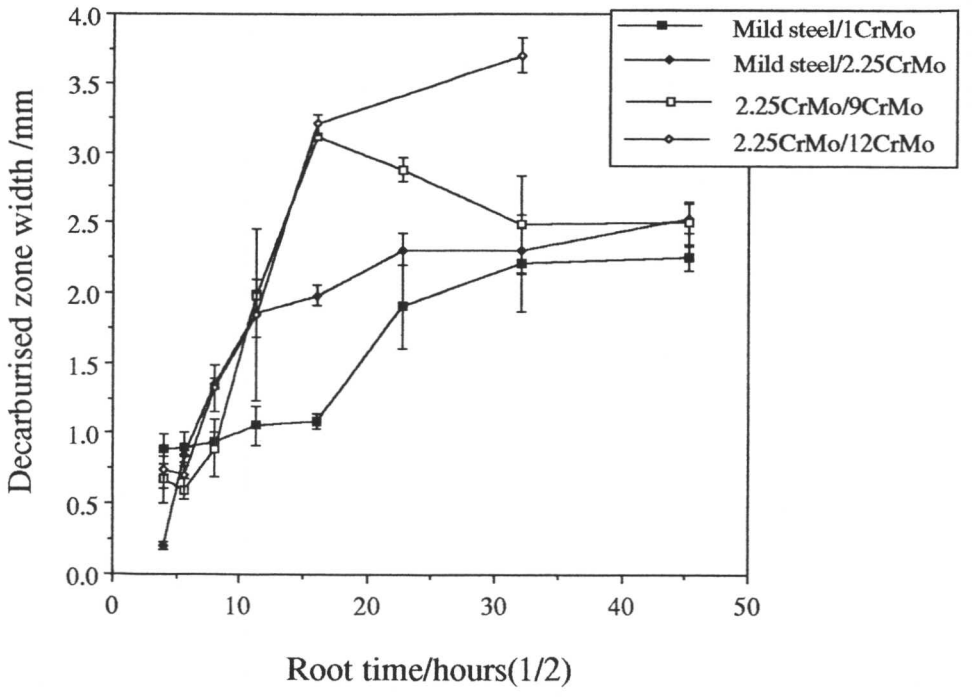

a) Post weld heat treatment temperature

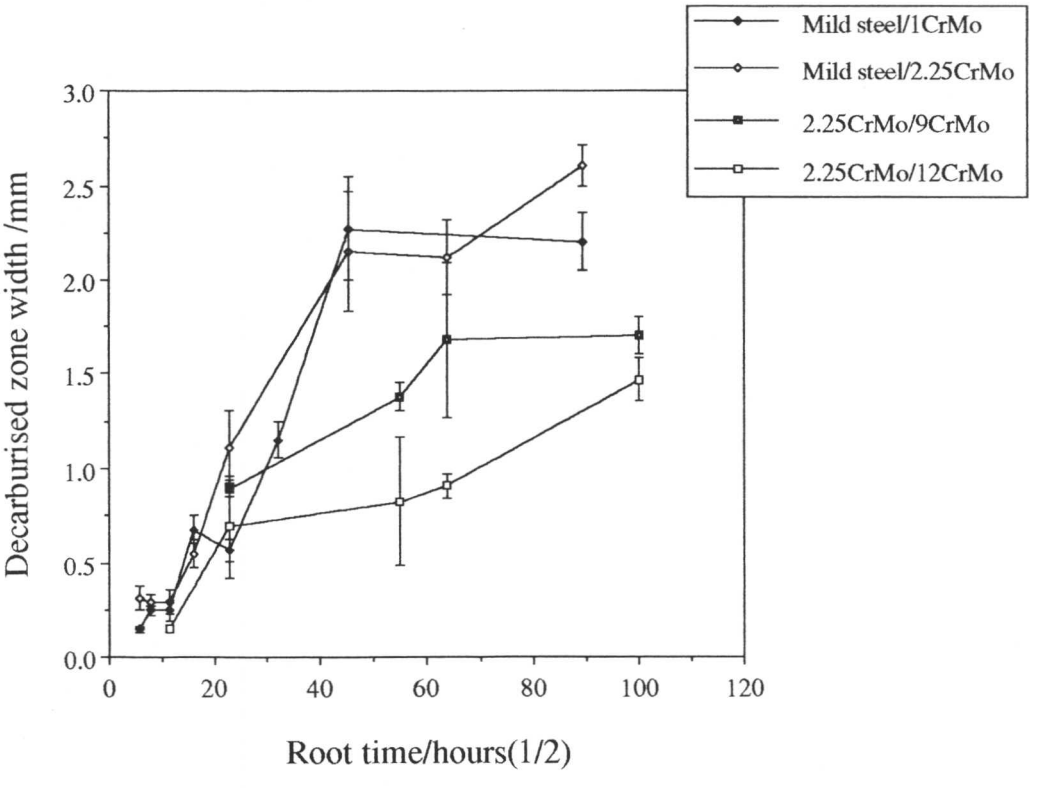

b) 620°C

Figure 6.7: Effect of alloy content on the decarburised zone width for all of the joints at a) post weld heat treatment temperature and b) 620°C

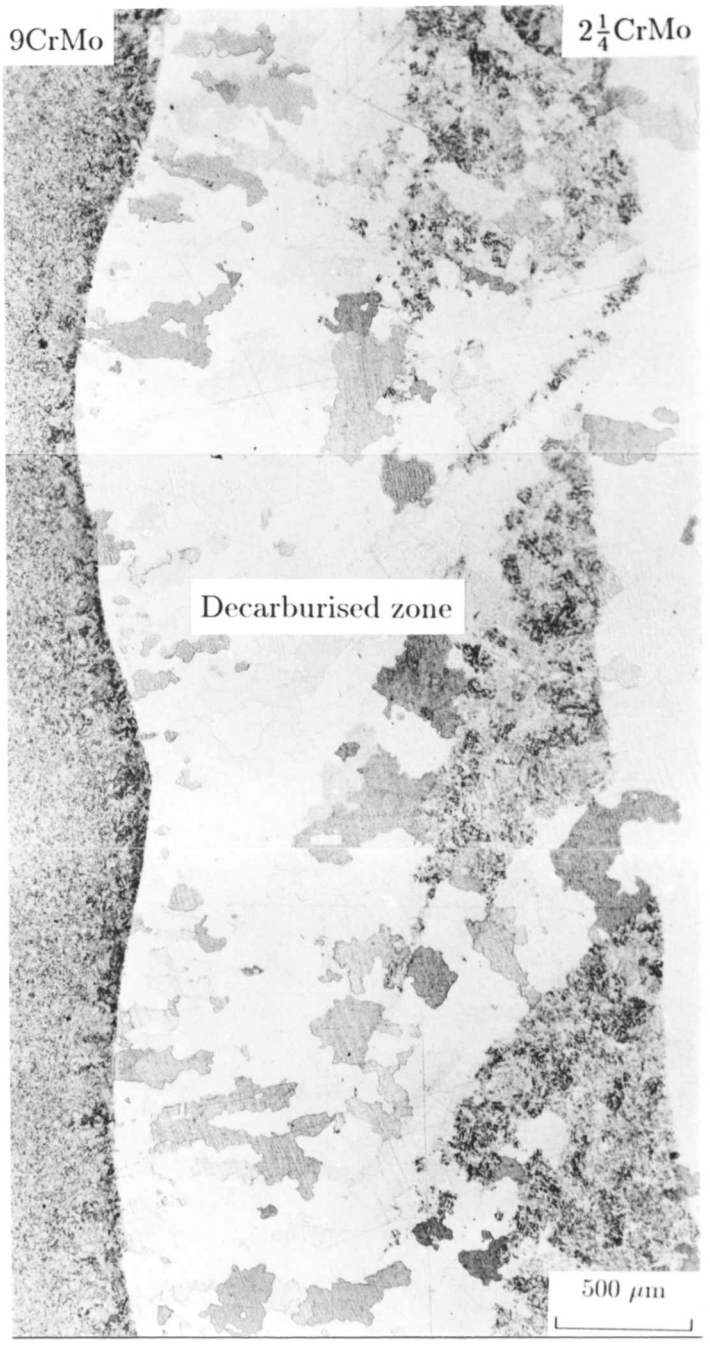

Figure 6.8: 9CrMo/$2\frac{1}{4}$CrMo joint heat treated at 730°C for 64 hours indicating the difficulties in measuring the decarburised zone width

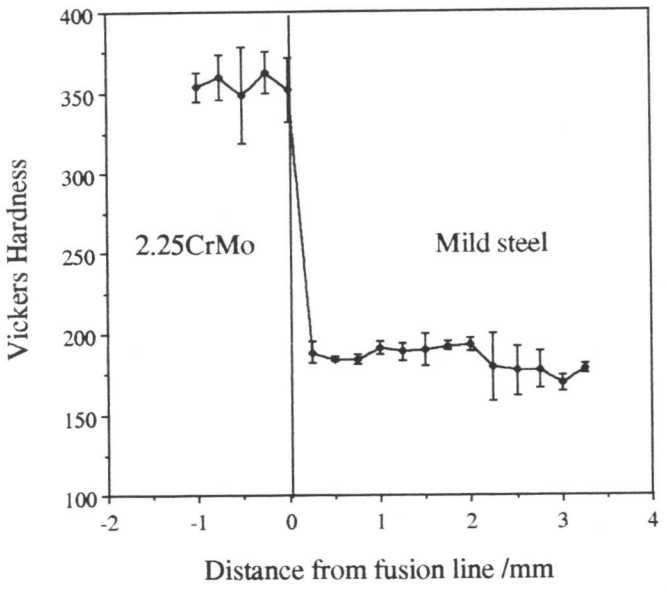

a) mild steel/$2\frac{1}{4}$CrMo - unaged

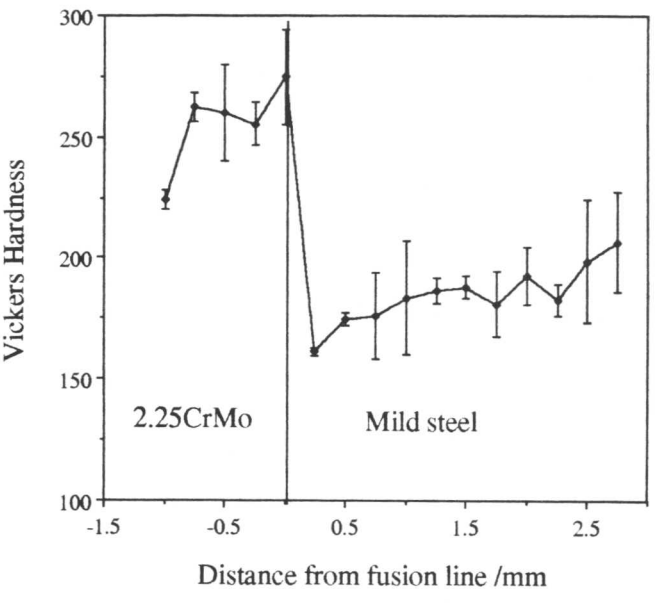

b) mild steel/$2\frac{1}{4}$CrMo - 32 hours

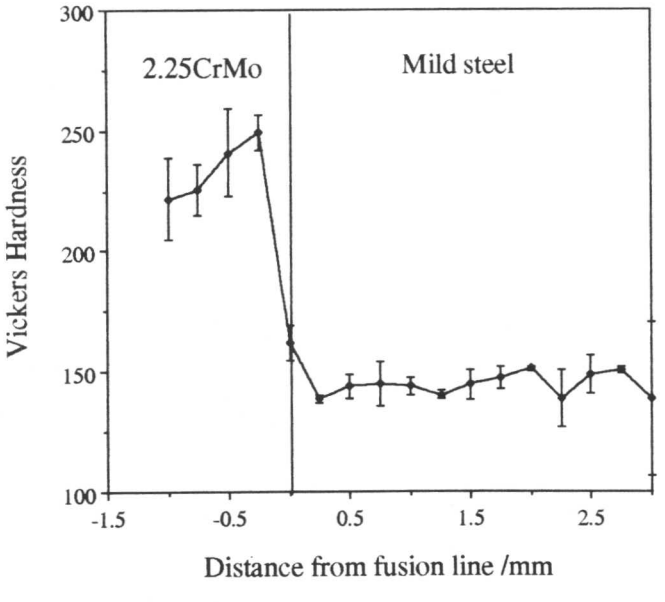

c) mild steel/$2\frac{1}{4}$CrMo - 256 hours

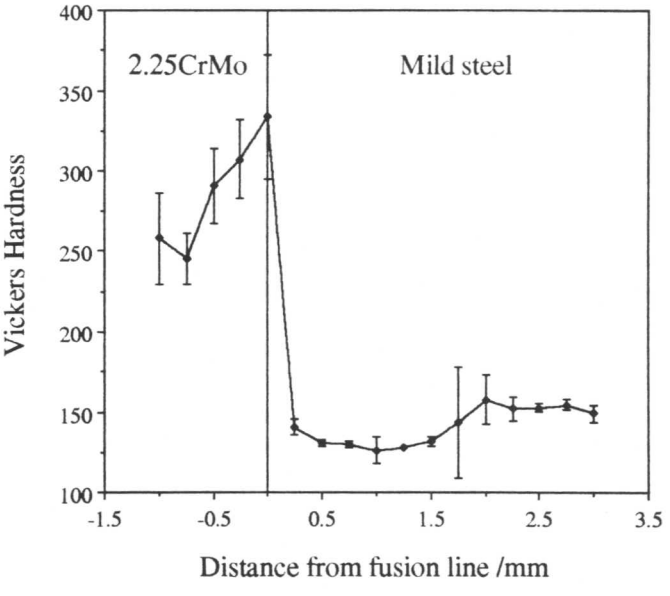

d) mild steel/$2\frac{1}{4}$CrMo - 1024 hours

Figure 6.9: Hardness profiles for the mild steel/$2\frac{1}{4}$CrMo joint heat treated at 700°C

(Figure 6.11). This illustrates that the zones formed on either side of the interface are unequal and carburisation is less extensive than decarburisation.

6.5 Characterisation of microstructure

From these initial results a clearer understanding of the microstructural changes occurring in the joints is required to try an explain the apparently anomalous observations concerning the shape of the decarburised zone width curve and the effect of alloy content. To this end electron microscopy techniques were employed. A scanning electron micrograph across a mild steel/$2\frac{1}{4}$CrMo joint at 700°C (Figure 6.12) illustrates the change in microstructure and specifically carbide size, shape and volume fraction. The parent plate, which was initially a ferrite/pearlite structure still shows this structure although the pearlite is now spherodised. The decarburised zone is characterised by the large ferrite grains which are virtually precipitate free. At the interface there is a sharp transition between the precipitate free (low alloy) side and the precipitate rich (high alloy) side. Figure 6.12(c) illustrates the morphology and volume fraction of carbides in this region. When compared with the micrograph of the weld metal in Figure 6.12(d) it can be seen that the precipitation is more extensive at the weld interface. Figure 6.13 compares the interface region for the other three joints at this temperature. The main point to notice from these micrographs is that the size and volume fraction of carbides is lower in the $2\frac{1}{4}$CrMo/9CrMo and $2\frac{1}{4}$CrMo/12CrMo joints than it is in the mild steel/1CrMo and mild steel/$2\frac{1}{4}$CrMo joints.

A more extensive study of the carbides at the interface was made using transmission electron microscopy. The carbides could be identified either by electron diffraction or the EDX technique as described in Chapter 5. Typical extraction replicas from the $2\frac{1}{4}$CrMo side of the mild steel/$2\frac{1}{4}$CrMo steel weld are presented in Figure 6.14 showing the morphology of the carbides present and typical diffraction patterns from the major types. Representative chemical analyses are given in Table 6.2. Carbide identification was carried out initially for the mild steel/$2\frac{1}{4}$CrMo joint at 700°C. Figure 6.15 illustrates the fraction of carbide types of the total identified at each heat treatment. It is interesting to note in this figure that the less stable cementite is reappearing in the specimen after its initial dissolution earlier in the precipitation sequence. The literature reviewed earlier appeared to predict that the structure was tending towards one of $M_{23}C_6$ and M_6C (Figure 6.16). Results from the mild steel/$2\frac{1}{4}$CrMo joint at 620°C are presented in Figure 6.17 which indicates a similar reversal in the precipitation sequence at longer times. An investigation was then carried out on the other joints to ascertain whether the same phenomenon could be observed. The 1CrMo maintained a structure of

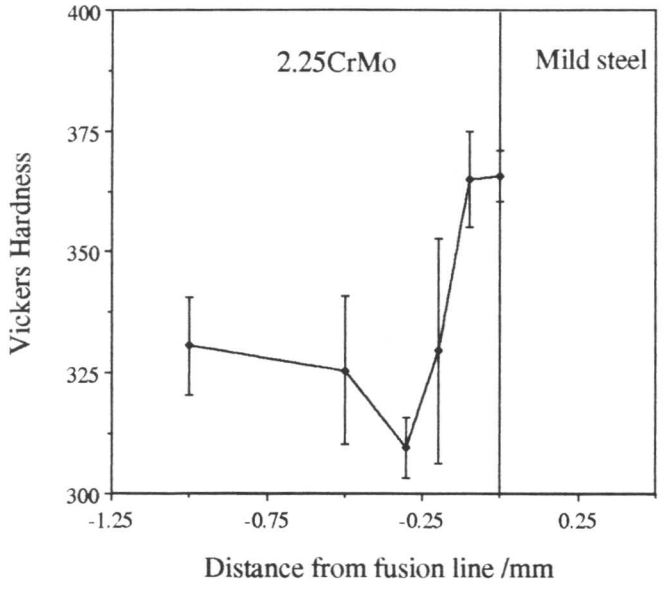

a) mild steel/$2\frac{1}{4}$CrMo - 16 hours

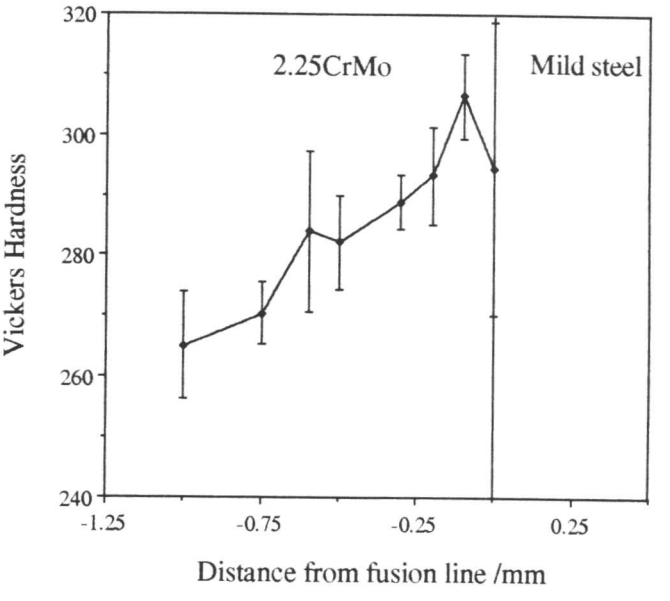

b) mild steel/$2\frac{1}{4}$CrMo - 64 hours

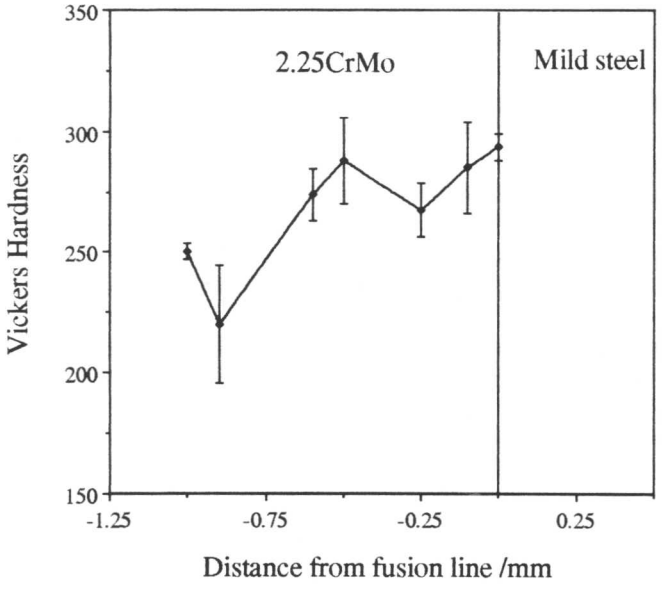

c) mild steel/$2\frac{1}{4}$CrMo - 256 hours

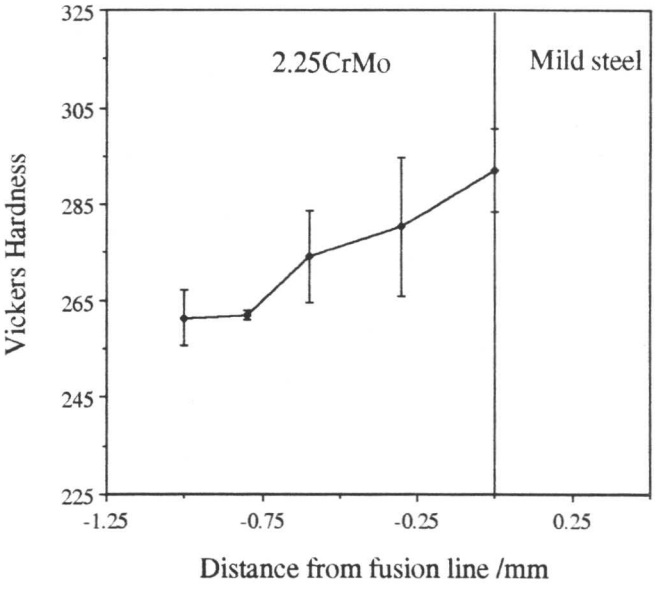

d) mild steel/$2\frac{1}{4}$CrMo - 1024 hours

Figure 6.10: Hardness profiles for the mild steel/$2\frac{1}{4}$CrMo joint heat treated at 700°C showing the carburised region

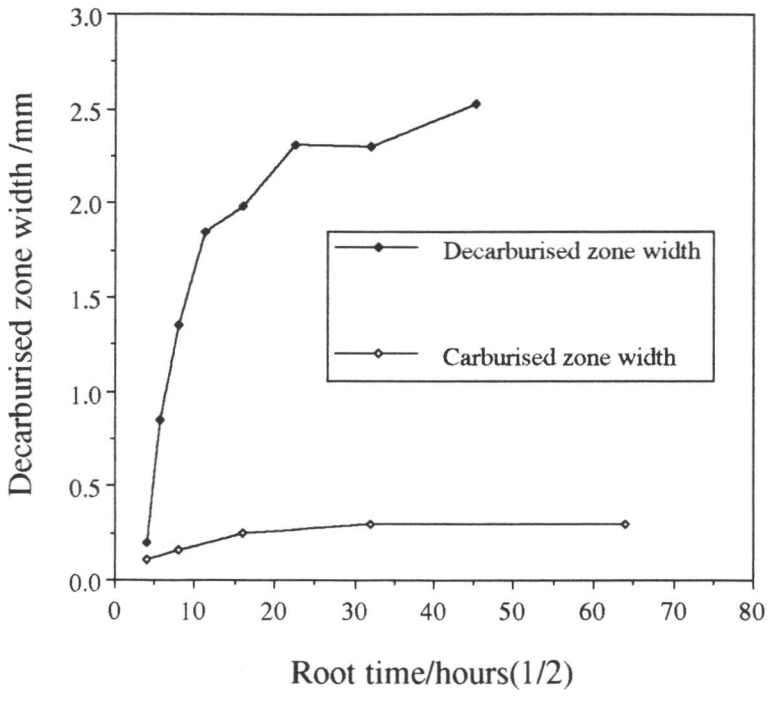

Figure 6.11: Comparison of carburised and decarburised zone widths for the mild steel/$2\frac{1}{4}$CrMo joint heat treated at 700°C.